Master Thesis

Influence of rapid drawdown on dike stability

Steve van Adrichem

January 22, 2021

Cover: Levee failure due to rapid draw down along the Mississippi River near Marchand, LA (Vanden Berge, 2014)

Master Thesis

Influence of rapid draw down on dike stability

by

Steve van Adrichem
Student number: 4393848

to obtain the degree of
Master of Science
at the Delft University of Technology

to be presented on the January 16, 2021

Project duration	February 1, 2020 - October 30, 2020
Thesis committee:	Dr. ir. A. Askarinejad, (Chairman)
	Dr. ir. C. Zwanenburg
	Dr. ir. J.D. Bricker
	Ir. P.R.M. Ammerlaan

Abstract

The aim of this research is to find the influence of rapid drawdown on dike stability with the Delta21 project as case study.

The Delta21 project is a proposed plan for a waterdefence system in front of the Haringvliet, The Netherlands. Its main element is a water retaining lake with an extensive pumping and turbine system. Whenever other storm surge barriers close, water from inland rivers can be pumped to the sea. The water retaining lake can act as an energy storage system as well by using the turbines to generate electricity at moments of high energy prices. The pumping system has the capacity to reduce the water level with 17.5m in 12hours. The dike surrounding the lake has a gradual slope as the height/width ratio below the water line is 1/20. It consists fully of a homogeneous and permeable fine sand. The estimation of material properties were based on limited CPT data, samples from the adjacent Maasvlakte II and empirical relationships.

The rapid decrease of the water level in the lake causes rapid draw down conditions in the dike. Hereby the external hydrostatic pressure is reduced due to unloading effect of removing water, while a delay in the dissipation of pore pressures inside the dike is produced. This causes stress relaxation and slope instability.

The research was performed using a numerical model verified with physical modeling in the form of centrifuge tests. For the numerical model the finite element model PLAXIS2D was used. A fully coupled flow-deformation analysis was chosen, which can solve the full interaction between deformation, consolidation and groundwater flow simultanously in the same phase. It considers a reduced permeability and degree of saturation in the unsaturated zone. The Hardening Soil small strain model was selected as constitutive model due to the potential of capturing hysteresis in the stress-strain regime. Hysteresis could occur as a result of multiple cycles of water level fluctuations.

To gain better understanding of the capabilities and weaknesses of the numerical model, it was verified with several physical tests from literature. The first test is a centrifuge test with failure due to increasing hydrostatic pressures within the dike. The moment of occurrence and shape of the failure contour were compared with the numerical model. The second test was a centrifuge test where a dike experiences rapid draw down conditions with the purpose to validate the pore pressure and saturation level. Thirdly, a full scale test of a dike with a changing water level was added, because full scale tests offer the closest resemblance to situations in the field. The field test was modeled to double check pore pressures and saturation.

The research aimed to further investigate the development of a failure during rapid draw down, a centrifuge test was performed at 100g. Rapid draw down conditions were simulated on a sand dike with slope 1:1.6 to generate failure. By tracking grains with Particle Image Velocimetry (PIV), correctness of estimating displacement by the numerical model was verified. The addition of pore pressure sensors could give further information on pore pressure development.

The numerical model proved to accurately predict positive pore pressures and the moment at which macroscopic failures occur due to drawdown. Negative pore pressures, saturation and development of the failure, in terms of size and deformation could not be accurately approximated.

With understanding of the capabilities and weaknesses of the numerical model, the dike of the Delta21 project was modeled. The original design proved to be stable with a FoS of 6.20. Increasing slope angles were modeled resulting in a decreasing FoS. The influence of hysteresis was found to be very small after modelling multiple cycles of changing water level. The positive effect on stability the addition of a high permeable filter layer was modeled. Finally the risk of erosion due to water outflow was analytically calculated and proved to be closely related to the numerical results.

Acknowledgement

First and foremost, I would like to sincerely express my gratitude to my thesis supervisor, Dr. ir. Amin Askarinejad for all the advice I got during this project. When working at the university, he used to have the door of his office open, so a question could be easily asked. His engaged attitude and critical mindset had a very positive effect on this work.

I would like to thank Dr. ir. Cor Zwanenburg and Dr. ir. Jeremy Bricker for joining my thesis committee. The feedback they gave me during our meetings is much appreciated.

Furthermore, I would like to express my thanks to ir. Patricia Ammerlaan for the useful discussions we had and for giving me the opportunity to graduate at Royal Boskalis Westminster N.V. The Covid-19 pandemic made working at the office not possible. However, I feel grateful for having been part of the company.

I would like to express my gratitude to ir. Huub Lavooij and Leen Berke for letting me be part of the Delta21 plan and giving me the freedom to develop my own research question.

My thanks are directed to ir. Yuen Zhang with whom I shared an interest in simulating rapid draw down conditions in a geotechnical centrifuge. His time in explaining me all the details was meaningful for this work. Especially during the pandemic it was besides helpful, very enjoyable to discuss and work together with a fellow researcher. Furthermore, I would like to thank Dr. ir. Huan Wang and Roland Klasen for their technical support with the geotechnical centrifuge.

Last of all I want to thank my friends and family for their support, and in particular my housemates. I missed working in a team during this research a lot. The good fun from my housemates and their hard-working mentality gave me a lot of motivation to give this thesis my best.

Contents

1 Introduction

1.1. Motivation

The motivation for this research is the Delta21 project. This is a visionary waterdefence system in front of the Dutch coast, between Maasvlakte 2 and Goeree Overflakkee. It ensures that three ambitions are achieved in one go: Flood risk management, Energy storage and Nature restoration. The Flood risk management element is achieved by realizing a large water discharge system in combination with a new water retaining lake that consists of a row of dunes with an open tidal power plant. The water discharge system is used at high river water levels to pump water into the North sea (Ansorena Ruiz, 2020). Because the lake has a function of energy storage as well it is often emptied and filled (Huub Lavooij, personal communication, 6-04-2020). The managers of the project asked the question of the rapid draw down during emptying could be a potential tread to the stability of the dike.

Rapid reduction in the water level of rivers and lakes have a strong correlation on the decrease of the factor of safety of a dike (Alonso Pérez de Agreda and Pinyol Puigmartí, 2009). Accordingly, it is predictable that the probable increased sea level and number of extreme events(Meehl et al., 2000), will lead to an increase of dike failures and floods in the future. This would be a continuation of the trend of last century, where an increasing amount of people and area were affected by floats (Paprotny et al., 2018). Examples of such slope failures caused by rapid draw down include the pilarcitos Dam sourch of San Fransisco, Walter Boudin Dam in Alabama, and a number of river bank slopes along the Rio Montaro in Peru (Duncan et al., 1990). Therefore, a better understanding in the effect of rapid draw down conditions on dike stability is necessary.

1.2. Objective

When the water level next to a dike is decreased quickly, the fast reduction of the external water pressure causes rapid draw down conditions in the dike. Hereby the external hydrostatic pressure is reduced due to unloading effect of removing water, while a delay in the dissipation of pore pressures inside the dike is produced. This causes stress relaxation and slope instability. The effect of water drawdown has been investigated using laboratory tests (Wang et al., 2012)(Yan et al., 2010), numerical analysis (Viratjandr and Michalowski, 2006a) and limit equilibrium analysis (Gao et al., 2014). In addition, analysis of real cases are performed in the past (Zhang et al., 2010)(Li et al., 2010).

Previous studies have alluded the importance of the role of undrained soil behaviour on the pore water pressure within the dike and on stability and advise to use a coupled analysis (Alonso and Pinyol Puigmartí, 2009). However, a lack of in-depth knowledge and verification with lab tests is still apparent in this area due to the large number of variables and conditions. These include material properties, shape and size of the model, and boundary conditions like time and reduction in water level.
Accordingly, the main goal of the research is to gain a comprehensive understanding of the effect rapid draw down has on the stability of a dike. Hereby special interest is taken into the dike of the Delta21 project. The investigation can be divided into two main areas:

- In the first part of the study the capabilities and weaknesses of the numerical model with a fully coupled flow analysis in modeling the stability of a dike in a rapid draw down situation are investigated by comparing the numerical model with physical tests in the form of centrifuge and field tests.
- In the second part the numerical model is used to simulate the decrease in stability during rapid draw down conditions of the Delta21 dike taking into account the effect of different slope angles, multiple cycles of drawdown and the addition of a drain.

1.3. Methodology and thesis outline

To gain insight in rapid draw down and to be able to answer the research question a combination of numerical modeling and physical testing is exploited. Hereby the physical modeling is used to support the numerical model by using it for the objective of verification. While the numerical model is used to develop hypotheses and for understanding the hydro-mechanical processes leading to a global failure of a dike during rapid draw down. This document is divided into 8 chapters and the interaction between different chapters is illustrated schematically in figure 1.1

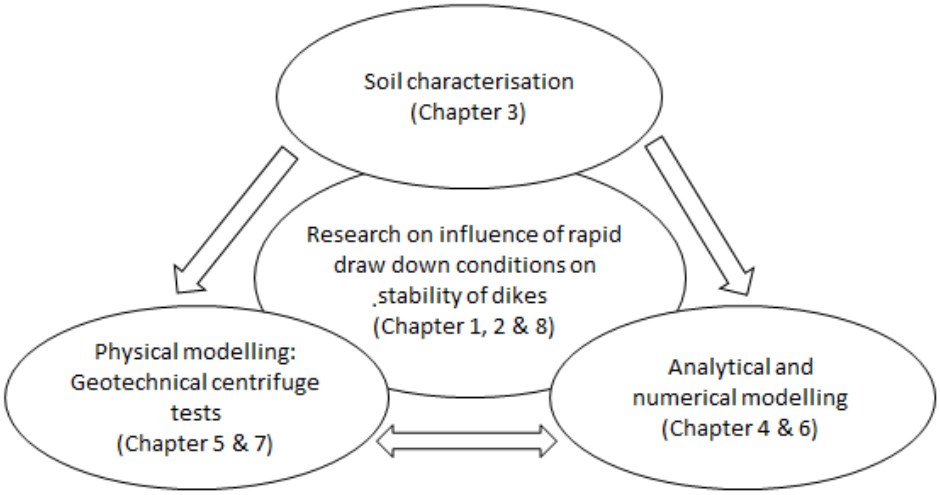

Figure 1.1: Schematic showing the interaction between different parts of the dissertation

- In Chapter 2 a brief literature background on rapid draw down is presented. Afterwards it compiles the background of the Delta 21 project.
- The third chapter is dedicated to unsaturated soil mechanics. Firstly a theoretical background is provided. Afterwards the use of unsaturated soil mechanics in the finite element model PLAXIS is explained. Lastly the constitutive models, Mohr-Coulomb and Hardening Soil with small strain stiffness are elucidated.
- The verification of the numerical model is focused on in chapter 4. This chapter is divided into three parts. In the first and second a centrifuge test from literature is compared with results from the numerical model. In the last part the results of a field test and the numerical model are analysed and interpreted.
- Chapter 5 concentrates on the equipment and test setup of the physical modeling with a centrifuge test. A centrifuge test is presented and compared with the numerical model.
- Chapter 6 is devoted on numerically modeling the dune of the Delta21 project. Results of stability of different designs and scenarios are presented.
- Finally, some conclusions and recommendations are given.

2

Literature review

2.1. Literature on rapid draw down

2.1.1. Failure mechanism during rapid draw down

According to Fattah et al. (2015), who modeled an earth dam, rapid drawdown causes a slight decrease in the factor of safety against sliding of the dam within the short period after the rapid draw down. It can be explained that the water load has disappeared during rapid drawdown and the hydrodynamic pressure creates the downward forces, resulting in a decrease of the shear resistance of the upstream slope. Besides, there is no supporting pressure to resist against mobilizing of the upstream slope. Afterwards the factor of safety increases again, due to the dissipation of excess pore water pressure with time which leads to increase of the effective stresses in the soil and hence increase its shear strength. Several studies have shown that an increase of the speed of drawdown or a decrease in permeability decrease the factor of safety in the dike. Both cause a higher difference in pore water pressure between the outside and inside of the dike. Vrielink (2020) Souliyavong et al. (2012).
In several papers it has been shown that when the water level changes over time in a sinusoidal shape the lowest factor of safety is achieved just before the water level is at its lowest point (Viratjandr and Michalowski, 2006b)(Lane and Griffiths, 2000). At that moment the dissipation of excess pore water pressure has a more positive effect on stability than the slowly decreasing water level.

2.1.2. Mechanisms influencing pore water pressure

Pore water pressures in an initially submerged slope and later subjected to drawdown depend on soil parameters and “external” conditions: soil permeability (saturated and unsaturated), soil water retention properties, mechanical soil constitutive behaviour, rate of water level lowering and boundary conditions. According to Alonso Pérez de Agreda and Pinyol Puigmartí (2009) there are two fundamental mechanisms controlling the resulting pore water pressure: The first one being newly generated flow regime and second one being the change in pore pressure induced by boundary changes in stress. In a simplified situation, under elastic hypothesis for the soil skeleton, the pore pressure depends on the ratio of soil bulk stiffness and water compression modulus. Hereby there is a clear correlation between a sand with higher stiffness and a slower response in pore water pressure after changes in the stress regime. However, in most situations, this ratio is small and the influence of soil stiffness is negligible. This implies a maximum response of the saturated material to stress changes. Without this coupling, the initial pore pressures do not change during very rapid unloading.

2.1.3. Modelling rapid draw down

Classical methods of analysing stability during rapid draw down in a dike include a pure flow analysis and an undrained method. In the first case the soil body is taken as a being a fully rigid body and the flow problem is solved by a change in hydraulic boundary conditions as done by Skempton (1954) and Vandenberge (2014). The undrained approaches do take soil deformation into account. Nevertheless, the soil is taken as impervious with the assumption that drawdown happens instantly.

The 'instantaneous' or undrained method is conservative, but very unrealistic. At the opposite extreme is the pure flow analysis where the dike is taken as rigid soil body. Dilatancy in the dike can cause shear effects which generate additional pore water pressures. Therefore it is not correct to think that in case of rigid material only flow based analysis is sufficient. This leads to a systematic and unsafe underestimation of the pressures caused by soil deformation. (Alonso Pérez de Agreda and Pinyol Puigmartí, 2009).

In addition, the position of the phreatic line does not provide enough information to calculate safety factors against slope failure if due consideration is given to the strength for positive suctions, above the zero-suction surface. Therefore, methods for drawdown analysis, which concentrate on the determination of the position of the phreatic line, using formulations for saturated flow, may lead to significant errors.
Fully coupled flow-deformation analysis in PLAXIS can solve the full interaction between deformations, consolidation and groundwater flow simultaneously in the same phase. This calculation combines staged construction and transient groundwater flow. Coupled analysis capture the actual measurements well. Hereby there is a clear correlation between a sand with higher stiffness and a slower response in pore water pressure after changes in the stress regime (Alonso Pérez de Agreda and Pinyol Puigmartí, 2009).

2D modelling
Just like in this research, the models for the papers above are all in 2D. Viratjandr and Michalowski (2006b) looked at the differences of modelling rapid draw down in 2D and 3D and concludes that 2D solutions yield a conservative estimate of the stability of a 3D slope, especially for a slope constrained to a small width. The difference between 2D and 3D solutions for a slope of height/width 1/2 can exceed 15%, while when the height/width < 1/10 the difference is smaller than 5%. If the water level is reduced slower the 2D and 3D give more similar results.

2.2. Unsaturated soil mechanics

2.2.1. Importance of unsaturated soil mechanics

Dikes subjected to transient water conditions show to have a varying water table over the body of the dike. Below the phreatic water level the soil will be completely saturated, meaning that all pores are filled with water. Other parts of the dike will be completely dry, meaning that the pores are filled with air. Between these two conditions is the unsaturated soil, which is defined as a three-phase material, comprising soil solids, water and air (Terzaghi, 1943).

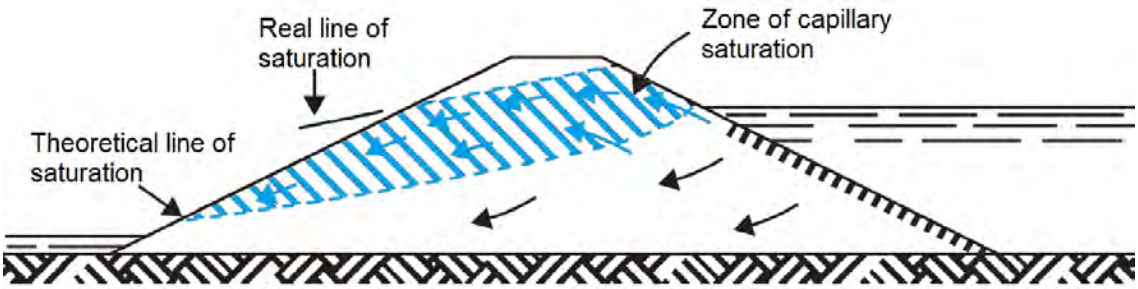

Figure 2.1: A dike illustrating the flow of water above the theoretical phreatic line through the capillary zone (Terzaghi, 1943)

Typical soil conditions are illustrated in figure 2.2.S_r represents the degree of saturation and u_w the pore water pressure. Below the phreatic water level the soil is saturated and the pore pressures are positive. Above the phreatic water level in the unsaturated zone the pore water pressures are negative. The soil desaturates above the phreatic water level until it is completely dry.

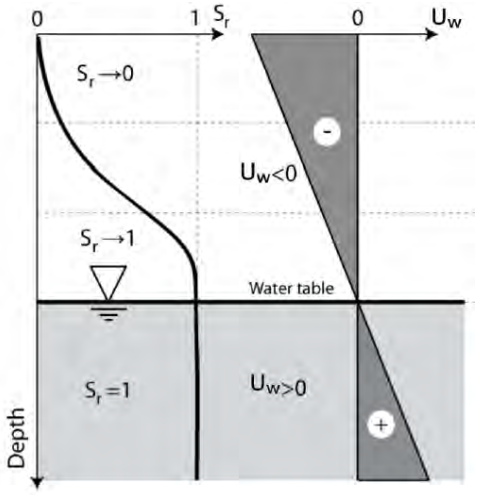

Figure 2.2: Schematic representation of the saturation phases in a soil profile with a ground water table below the surface (Nuth, 2009)

2.2.2. Matric suction in the soil

Matric suction has been widely considered as the most fundamental physical variable governing unsaturated soil behavior such as effective stress, shear strength, welling pressure, freezing temperature depression, and thermal conductivity (Philip, 1977). Unbalanced inter-molecular forces are experienced by a water molecule at the interface of the air and water which lead to a 'tensile pull' along the interface. The difference between this air pressure u_a and water pressure u_w is called matric suction.

$$\text{Matric suction}(S) = u_w - u_w \tag{2.1}$$

The matric suction depends on the surface tension of the water (T_s), the contact angle of the membrane to the container wall (α) and the meniscus radius (R). The matric suction is larger at smaller meniscus radii. This implies that smaller pores create a higher matric suction.

$$u_a - u_w = \frac{2T_s * cos(\alpha)}{R} \tag{2.2}$$

2.2.3. Soil water retention curve

The soil water retention curve (SWRC) or soil water characteristic curve describes the relationship between the soil capillary head, ψ, and the volumetric water content, θ. The hydraulic conductivity function (HCF) describes the relationship between the unsaturated hydraulic conductivity, K, and θ. Different models permit defining the HCF in terms of the SWRC (Mualem, 1986). Therefore the SWRC can be considered to be one of the most fundamental hydraulic characteristics of a soil (Assouline et al., 1998). In figure C.1 the SWRC can be seen, keep in mind that there is hysterisis between the drying and wetting curve.

The volumetric water content used in these functions is defined as in the following equation:

$$\theta = \frac{V_w}{V_t}$$

Where V_w is the volume of water and V_t is the volume of soil. full saturation is reached when the full porosity (n) is filled with water, this is defined as θ_s. The residual value of water content θ_r is defined as the water content at which the slope of the SWRC go to zero when soil suction becomes large (Van Genuchten et al., 1991). This definition is however open for interpretation, because the SWRC is for a long time close to zero but not exactly zero. According to Luckner et al. (1989), the residual water content specifies the maximum amount of water in a soil that will not contribute to liquid flow because there is a blockage in flow paths or a strong adsorption onto the solid phase.

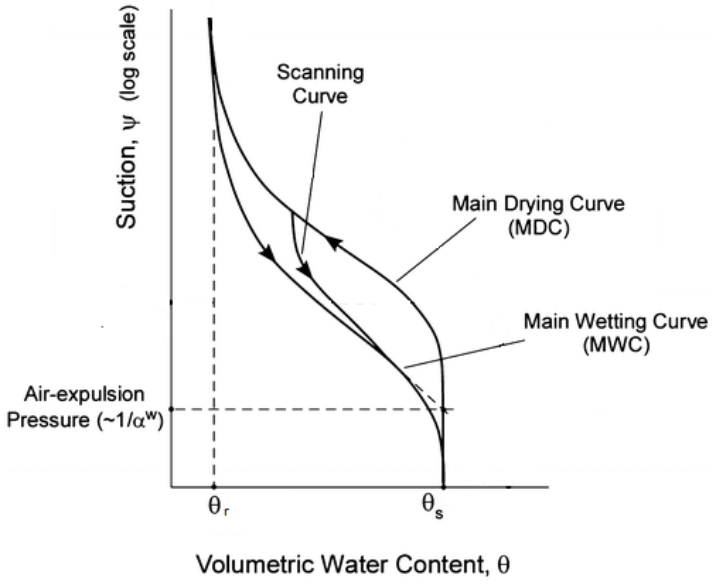

Figure 2.3: Soil water retention curve (Likos et al., 2014)

2.2.4. Flow equations

The flux (q) of water through the soil is proportional to the hydraulic head gradient (dH/dz). For saturated soils, the flux can be determined with the Darcy flow equation.

$$q = -K_s \frac{dH}{dz} \tag{2.3}$$

Where K_s is the saturated hydraulic conductivity and H is the potential energy as expressed in the following equation.

$$H = h_p + h_s + h_m + h_z \tag{2.4}$$

Where h_p = pressure potential
h_s = solute potential
h_m = matric potential
h_z = gravitational potential

Pressure potential represents the external forces and solute potential represents the attractive forces of water to higher solute concentration or osmotic forces. In most cases, pressure and solute potential are considered negligible. Therefore the total potential, in the context of this report, is the sum of the matric potential as described before, and the gravitational potential, representing the energy associated with the location of water in the Earth's gravitational field. The sum of matric and gravitational potentials, when expressed on an equivalent height-of-water basis, is known as the hydraulic head.

To describe the flow in the unsaturated part of the soil equation 2.3 is modified to

$$q = -K(_\theta) \frac{dH}{dz} \tag{2.5}$$

Hereby the hydraulic conductivity is dependent on the volumetric water content. To describe the flow in all directions, Equation 2.5 is combined with the equation of continuity. The equation of continuity is based on the principle of mass conservation. This principle states that the quantity of mass is conserved over time and that the rate of fluid loss or gain is equal to the net flow into and out of ta soil element. When neglecting changes in water density the continuity equation can be written as follows:

$$\frac{\delta\theta}{\delta t} = \frac{\delta q}{\delta z} \tag{2.6}$$

where t is time and z is depth. This combination is commonly known as the Richards equation (Richards, 1931).

$$\frac{\delta\theta}{\delta t} = \frac{\delta}{\delta z}\left[K(\theta)\frac{\delta H}{\delta z}\right] \tag{2.7}$$

2.2.5. Effective stresses in unsaturated soils

The effective stress is a combination of the total stress and the fluid phase pressures inside a porous material; According to Khalili et al. (2004), the concept of effective stress "converts a multi-phase multi-stress state porous medium to a mechanically equivalent, single-phase, single-stress state continuum allowing the application of the principles of continuum solid mechanics." For the saturated soil Terzaghi (Terzaghi, 1936) described the effective stress as in the following formula:

$$\sigma' = \sigma - u_w \tag{2.8}$$

Where σ' is the effective stress, σis the total stress and u_w is the pore water pressure. In the unsaturated soils where all three phases exist, it is more complicated. Jommi (Jommi, 2000) states that: "In fact, no single stress variable has ever been found which, substituted for effective stress, allows for a description of all the aspects of the mechanical behaviour of a given soil in the unsaturated range". However, Bishop proposed a formulation which is often used in soil mechanics to describe the effective stress (Bishop, 1959).

$$\sigma' = (\sigma - u_a) + \chi(u_a - u_w) \tag{2.9}$$

u_a is here the air pressure and χis the effective stress parameter, which is a function of degree of saturation. At full saturation χis 1, which leads Bishop's stress to be equal to Terzaghi's stress in formula 2.8.

2.3. Delta21 project

The current plan is to locate the waterdefence system of the Delta21 project between Maasvlakte 2 and Goeree Overflakkee in front of the Haringvliet, The Netherlands. An overview of the design is shown in figure 2.4. It's main element is a water retaining lake that consists of a row of dikes and a large water discharge system.

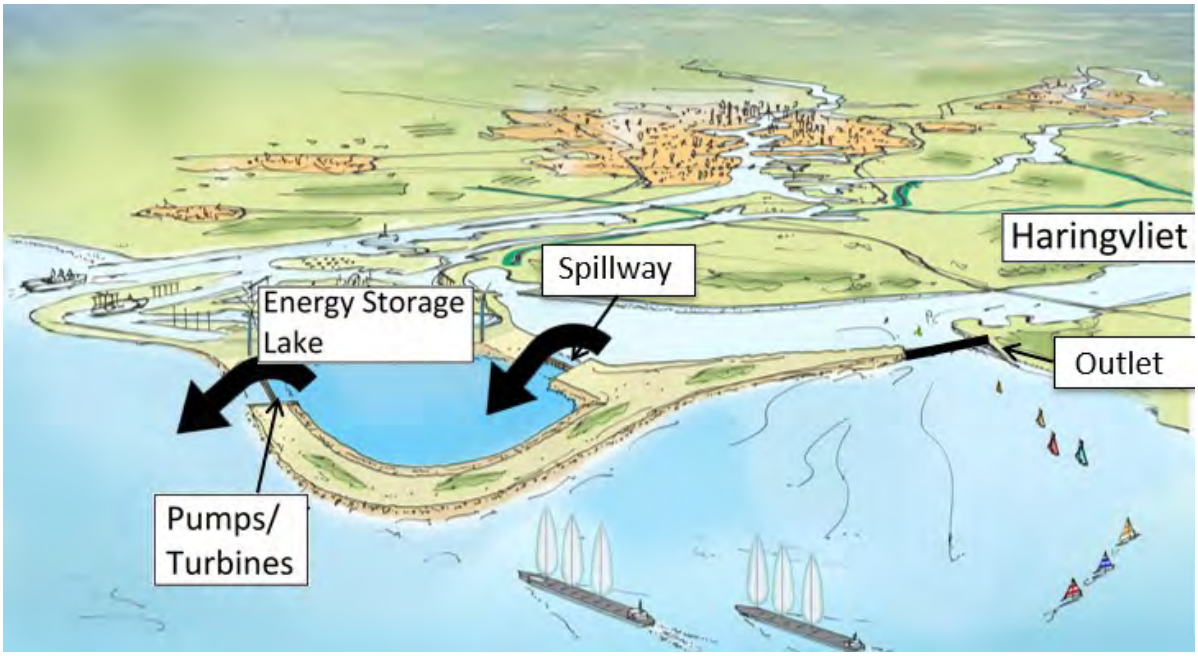

Figure 2.4: Overview of the Delta21 waterdefence system in case of a storm surge (black arrows represent direction of water flow)(Lavooij et al., 2018)

Under bad weather conditions like storm surge waterdefences system as the Maeslant storm-surge barier can be closed. Although the inland is protected from the sea, the river discharge will continue, causing the Maeslant barier to have limited time being closed. Therefore Delta21 suggest adding an extensive pumping system in the Haringvliet to pump out the excess water. The water of the Haringvliet will go through the spillway into the energy storage lake. This lake can be used as buffer and the pumps draw the water off from the lake into the sea.

Figure 2.5: Map of the Delta21 waterdefence system (black arrows represent direction of water flow at normal conditions)(Lavooij et al., 2018)

Under normal weather conditions, the water flows from the Haringvliet directly into the sea. The energy storage lake is not left unused in this scenario. The pumps are used to pump the water out the lake at moments of low energy demand. The energy is won back by using the pumps as turbines when filling up the lake with water from the sea at moments of high energy demand. Both the pumps and the turbines have an efficiency of 85%, making the total system around 72% effective (Huub Lavooij, personal communication, 4-2020). This process of energy storage is already proven in Norway (Hagos et al., 2014). The lake has a volume of 420million m3 and an installed power of 1.8 GW, this system can pump the water with 10.000m^3/s. This will reduce the water level from a maximum -5m NAP to -22.5m NAP within 12 hours. In the same amount of time the lake can be filled again to complete the cycle within 24hours (Lavooij et al., 2018). Figure 6.4 shows a series of possible water level fluctuations during a 10 day period. Firstly a high water level during bad weather conditions or maintenance, followed up by a period of water level fluctuations.

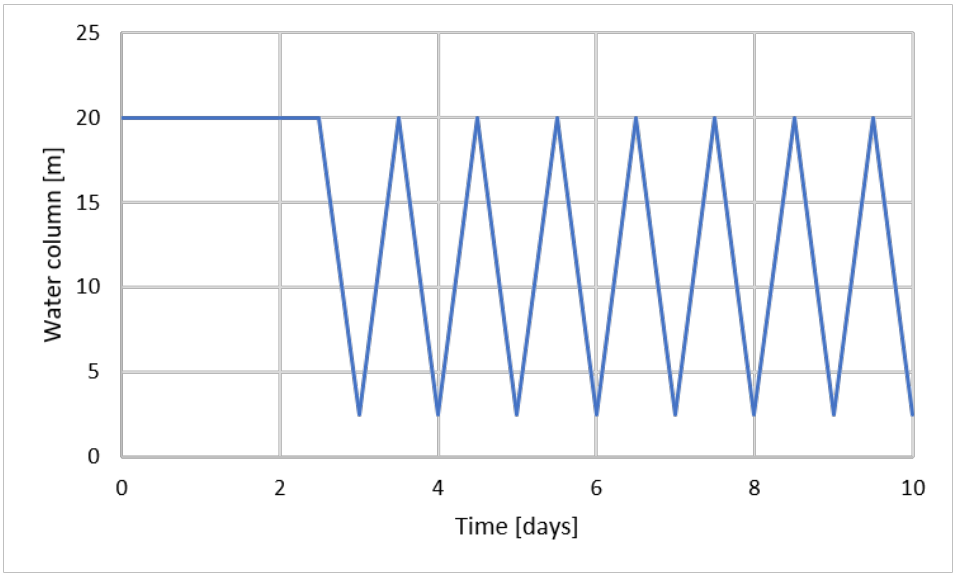

Figure 2.6: Water column during multiple cycles of drawdown

To accommodate large quantities of water the lake will be dredged to a depth of 25m. The dike around the lake will be made from the dredged sand as it is available in large quantities and therefore a cheap option.

The design can be seen in figure 2.7. Because sand has no cohesion the slopes are gradual, between 1/20 to 1/25 height over length ratio on the lake side. The design is based on the Dutch dunes stretching over the countries coastline.

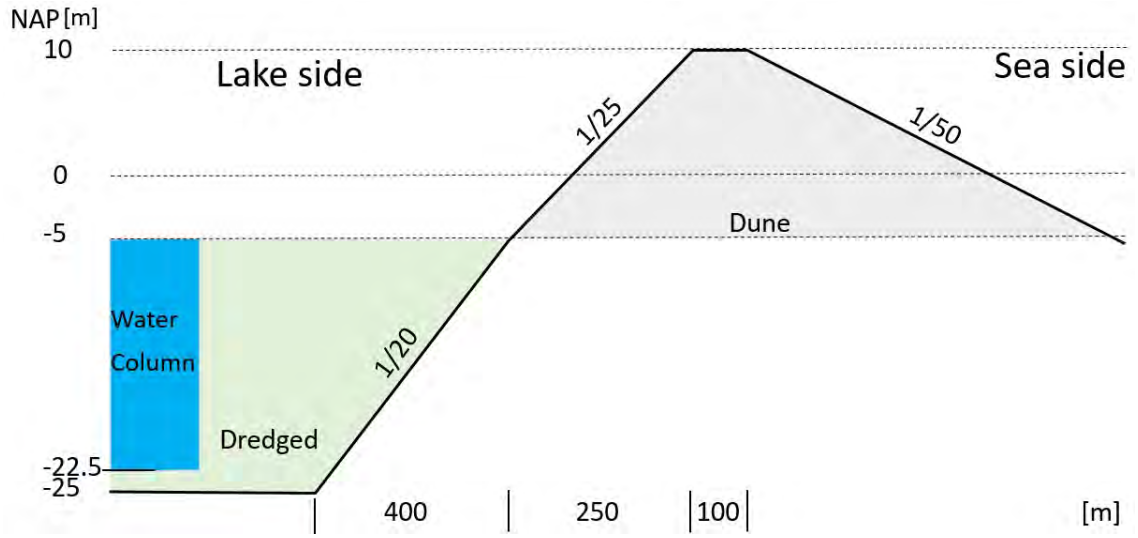

Figure 2.7: Cross section sea protection dike

2.4. Material of the Delta21 dike

The sand dredged from the energy storage lake will likely be used as building material for the dikes. In this section relevant soil parameters of the sand are described such grain size, friction angle and permeability.

In figure 2.8 the soil profile constructed from one of the CPT tests in the area is shown together with the CPT data (Paasman, 2020). Of the first 1.3m of the seabed no information is available. It is assumed that here fine sand is found. At a depth of 27m below NAP the cone resistance is higher than the maximum captured 30MN/m2. The location of the CPT is shown in figure 2.10. Other CPT profiles and their locations are shown in appendix chapter E. Because the soil profiles around the area of the energy storage lake show similar results, it would be reasonable to assume that the soil layers are horizontally continuing. However, earlier research on the Delta21 energy storage lake does not mention a clay layer between 21 and 23.5m depth. The current design, found in Ansorena Ruiz (2020), does not do this as well. For the remainder of this research it is assumed that only the fine grained sand will be used as building material for reasons of simplicity. However, the influence on stability the clay layer could have if being continuous, is being presented in section 6.6.

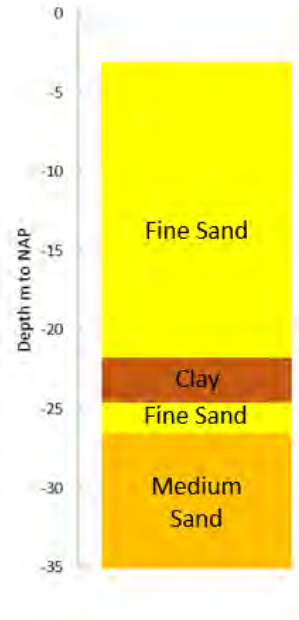

Figure 2.8: Soil profile of CPT S36H0032-01

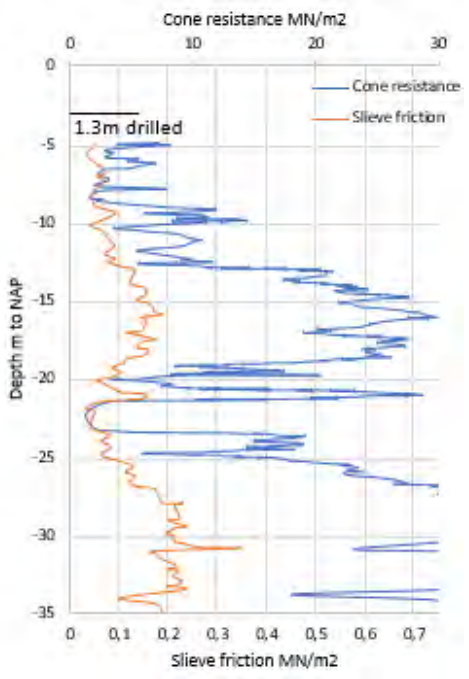

Figure 2.9: CPT S36H0032-01

Figure 2.10: location of CPT S36H00032-01 and of the sample for the grain size distribution

The grain size distribution has been found in the area as well for the purpose of a different unknown project. Figure 2.11 shows the grain size distribution of the fine sand taken from a 4-5m depth at the location shown in figure 2.10 (Geologische Dienst, 2020). The grain size distribution is gap-graded, which means that it has an deficiency of certain particle sizes. A minor part of the grains have a diameter between 0.3 and 1.0 mm. The sand consists mostly of fine sand grains smaller than 0.3mm together with 18% large grains with a diameter of 1.0mm.

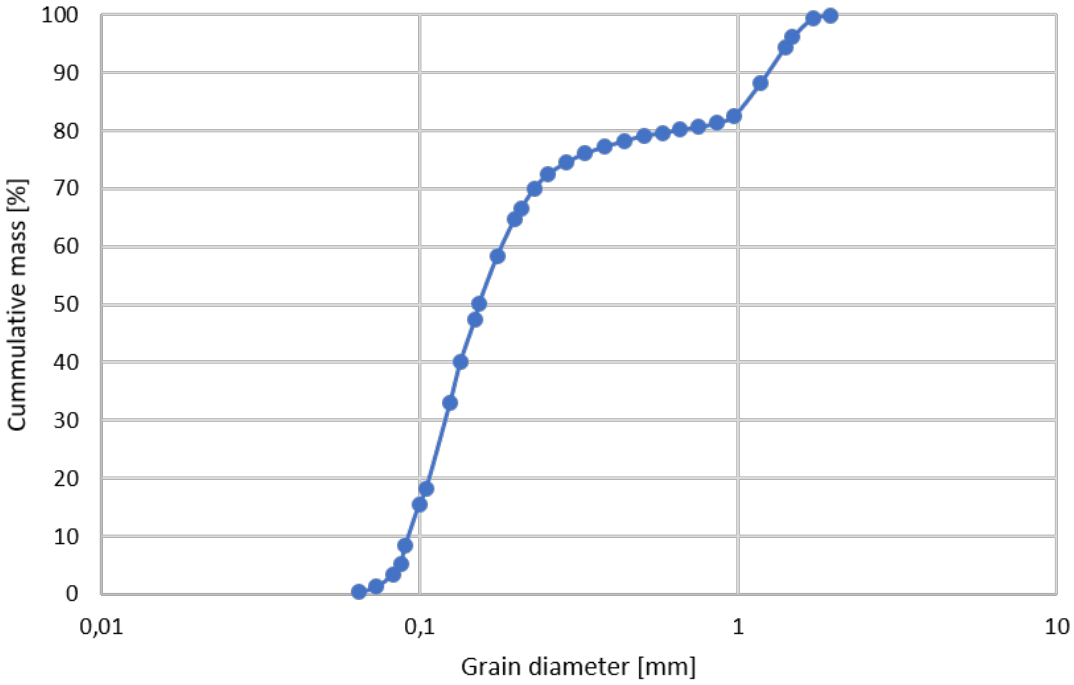

Figure 2.11: Grain size distribution

2.4.1. Relative density

The relative density is the dry density in situ, expressed in relation to two boundaries, the minimum and maximum density. The relative density based on the porosity (R_n) is generally used in Dutch practise and is given in equation 2.10. The relative density based on porosity is different than the relative density based on void ratio. The ratio between the two is shown in equation 2.12.

Relative density based on porosity:

$$R_n = \frac{n_{max} - n}{n_{max} - n_{min}} = \frac{\rho_d - \rho_{d;min}}{\rho_{d;max} - \rho_{d;min}} \tag{2.10}$$

Relative density based on void ratio:

$$R_e = \frac{e_{max} - e}{e_{max} - e_{min}} = \frac{\rho_{d;max}}{\rho_d} \frac{\rho_d - \rho_{d;min}}{\rho_{d;max} - \rho_{d;min}} \tag{2.11}$$

Relative density based on porosity and relative density based on void ratio are related together as given in equation 2.12.

$$R_e = \frac{\rho_{d;max}}{\rho_d} R_n = \frac{1+e}{1+e_{min}} R_n = \frac{1-\eta_{min}}{1-\eta} R_n \tag{2.12}$$

The minimum and maximum densities are defined by standard tests which are described in the Netherlands by Standaard RAW Bepalingen (CROW, 2020). Although these tests are not executed with sand from the location of the Delta21 lake, they are 5km north of the location at the Maasvlakte II. The following in-situ soil parameter information from the horizontal continuing fine grain soil material is achieved from the Maasvlakte II (Booster et al., 2008):

n_{max}	0.4630	[-]
n_{min}	0.3596	[-]
ϕ	33	[°]

Table 2.1: soil properties from Maasvlakte II analysis (Booster et al., 2008)

The relative density of the sand depends for a large part on sand placing technique. The Maasvlakte II project is constructed with the following techniques:

- Dumping (DU) by a Trailing Suction Hopper Dredger (TSHD);
- Rainbowing (RB) by a TSHD;
- Pumping (PU) through steel pipelines (hydraulic reclamation)
- Back filling through the suction pipe (BF)
- Spraying by using a spray pontoon (SP)

Sand can be dumped through the bottom doors of the TSHD when enough water depth is available compared to the draught of the TSHD. When the dumping area becomes too shallow for dumping, rainbowing is usually applied to place sand in the fill. Pumping through steel pipelines is applied for reclamation above water in areas that are out of reach for rainbowing. Spraying is used, when slope design requires precise placing of the sand within predefined tolerances (Vessies, 2012).

Activity	Relative Density R_n
Dumping under water (<10 m)	0.30.-0.40
Dumping under water	0.40-0.60
Spraying under water	0.20-0.40
Rainbowing (below lowest astronomical tide (LAT))	0.20-0.40
Rainbowing (Above LAT)	0.60-0.70
Hydraulic reclamation (below LAT)	0.20-0.40
Hydraulic reclamation (above LAT)	0.60-0.70
Compaction by bulldozers & trucks	+0.10
Compaction by vibro compaction	to 1.00

Table 2.2: Relative density for different kinds of placement techniques (CROW, 2004)

Vessies (2012) shows that the Maasvlakte II project sand is placed mostly with dumping under water if possible. Where this is not the case hydraulic reclamation and rainbowing techniques are adopted. Table 2.2 shows that rainbowing or hydraulic reclamation results approximately in an equal density.
It is assumed that the Delta21 project will apply the same construction techniques as the Maasvlakte II project. However, the depth of the seabed in the area of the Delta21 project is around 4 meter below NAP. That makes dumping under water not a suitable option. Therefore the sand is placed with Rainbowing or hydraulic reclamation between the seabed to the top of the dike. The lowest astronomical tide in the area is measured to be around 0m, equal to the average water height in the North Sea (Windfinder, 2020). It is assumed that at this height compaction by bulldozer trucks has effect, causing an average relative density of 0.75 above the LAT and a relative density of 0.3 below. This equals a porosity of respectively 0,432 and 0,385 and a void ratio of respectively 0,761 and 0,623. Below LAT the sand can be treated with additional compaction methods such as dynamic compaction or vibroflots. Although this is likely to increase stability the costs are high and therefore under water compaction is not take into account.

For the estimation of the density of the sand already in place, the emperical relation of (Schmertmann, 1976) was used. This relationship uses several constants and cone resistance from CPT data.

$$R_n(\%) = \frac{100}{C_2} ln\left(\frac{q_c(MPa)}{C_o(\sigma'_{vc})^{C_1}}\right)\frac{\rho_d}{\rho_{d;max}} \tag{2.13}$$

where C_0 =0.05 C_1 = 0.70 and C_2 = 2.91 (Schmertmann, 1978) The cone resistance can be found by analysing the CPT data in the Delta21 area and is taken to be 15 MPa. This results in an estimated average relative density of 64% and void ratio of 0.66. The assumend relative density's of the different layers are shown in figure 2.12. Different relative density's due to depth difference within the layers are not taken into consideration. The relative density of the sand below 5m NAP is the most important relative density, because the water level is always below this height.

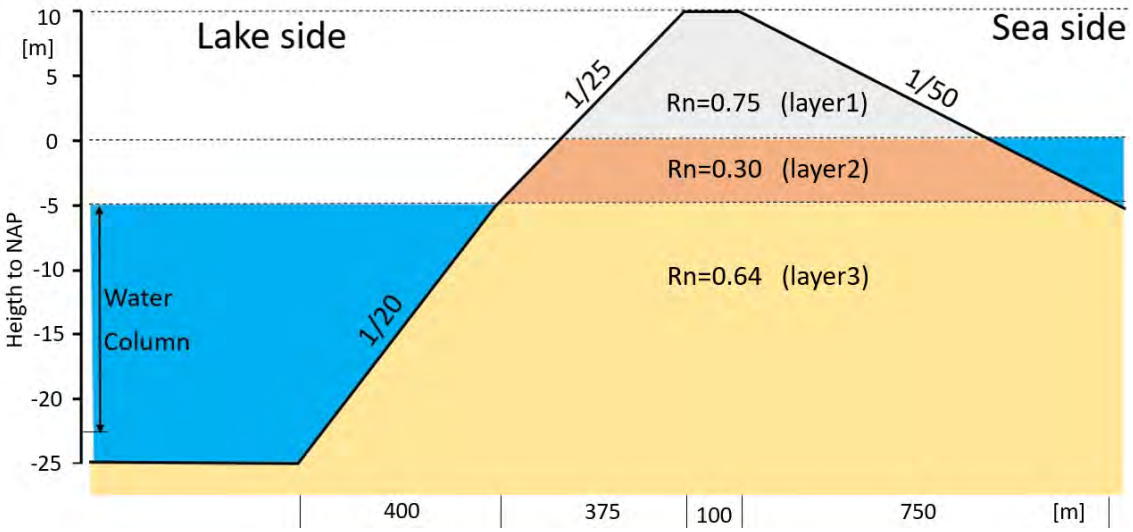

Figure 2.12: Cross section Delta21 dike with relative density

2.4.2. Stiffness

To estimate the average stiffness of the material the paper of Prof. Pieter Vermeer (2003) is used. A combination of reference pressure and cone resistance (q_c) is used to estimate the needed stiffness parameters. The cone resistance is taken to be 15 MPa and reference pressure as 100kPa. ($E_{oed}, *E_{50}, E_{ur}$) are estimated respectively 50, 44 and 175 MPa.

The stiffness is not uniform in the soil body. To find the dependency of soil stiffness on stress level the equations 2.14 to 2.16 (Plaxis, 2019). These are the same as used in the numerical model. The effect void ratio has on stiffness is not taken into account. An increase in density increases stiffness (Gao et al., 2015).

$$E_{50} = E_{50}^{ref} \left(\frac{c' cos\phi' - \sigma_3' sin\phi'}{c' cos\phi' + p^{ref} sin\phi'} \right)^m \tag{2.14}$$

$$E_{ur} = E_{ur}^{ref} \left(\frac{c' cos\phi' - \sigma_3' sin\phi'}{c' cos\phi' + p^{ref} sin\phi'} \right)^m \tag{2.15}$$

$$E_{oed} = E_{oed}^{ref} \left(\frac{c' cos\phi' - \frac{\sigma'}{K_0^{nc}} sin\phi'}{c' cos\phi' + p^{ref} sin\phi'} \right)^m \tag{2.16}$$

Where σ_3' = confining pressure [kPa]
m = Power component, 0.5 for sand [-]
p^{ref} = reference pressure (kPa)
c' = cohesion (kPa)
ϕ' = internal friction angle (°)
E_{50} = Stress dependent stiffness modulus for primary loading [kPa]
E_{50}^{ref} = Stress dependent stiffness modulus for primary loading at the reference pressure[kPa]
E_{ur} = Stress dependent stiffness modulus for re- and unloading [kPa]
E_{ur}^{ref} = Stress dependent stiffness modulus for re- and unloading at the reference pressure [kPa]
E_{oed} = oedometer stiffness modulus [kPa]
E_{oed}^{ref} = oedometer stiffness modulus at the reference pressure [kPa]

2.4.3. Hydraulic conductivity

To estimate the hydraulic conductivity of the sand, the grain size distribution is used. With the permeability and d_{10} known the widely accepted Kozeny-Carman equation can be used for the estimation of hydraulic conductivity. It is an appropriate function for soil with an effective size below 3mm with the exception of clayey soils (Carrier III, 2003).

$$K = \frac{g}{\nu} * 8{,}3 * 10^{-3} \left[\frac{n^3}{(1-n)^2} \right] d_{10}^2 \tag{2.17}$$

Where K = Hydraulic conductivity $[m/s]$
g = Gravitational acceleration [m/s^2]
ν = Kinematic viscosity (m^2/s)
n = Porosity (−)
d_{10} = Diameter where 10% of particles are smaller (by weight) (m)

As discussed in section 2 the dike is less stable during rapid draw down with a lower hydraulic conductivity. The hydraulic conductivity is linearly dependent on the kinematic viscosity, which depends on the salinity and the temperature of the water.

The water in the energy storage lake is fresh during bad weather conditions. In this case fresh water from the Haringvliet flows in the lake. The predominant situation is during normal weather conditions when salt water from the sea is pumped in the lake. Salt water has a lower viscosity and therefore leads to conservative stability estimations. Accordingly, the dynamic viscosity for salt water has been used.

The temperature of the water has an effect on the kinematic viscosity as well. Lower temperatures causes the water to have a higher viscosity. The lowest water temperature during the year of the North Sea in front of Rotterdam is 5°(ITTC, 2011). When assumed average sea salinity the dynamic viscosity of the water is in that case 1.5762E-06 m^2/s.

Relative density	Hydraulic conductivity	
0.75	$5{,}82 m/day$	$7.51{*}10^{-5} m/s$
0.30	$8{,}36 m/day$	$9.67{*}10^{-5} m/s$
0.64	$5{,}49 m/day$	$6.74{*}10^{-5} m/s$

Table 2.3: hydraulic conductivity in relation to void ratio

2.4.4. Soil water retention curve

The soil water retention curve (SWRC) is the relationship between soil/water matric potential (Φ) and volumetric soil-water content θ at equilibrium above the reference (zero) level represented by the free water table at atmospheric pressure (Novák and Hlaváčiková, 2019). In literature large number of measurement methods have been proposed to find the θ-Φrelationship. Arya et al. (1981) and (Kovács, 2011) describe two well known formulations, which are based on basic geotechnical properties. Mayor (2014) found positive results obtained from paired measurements of suction and θ in an instrumented dike, from laboratory tests and based on estimations from grain size distribution. Because the Modified Kovacs predicted the SWRC in the field more effectively, it was recommended. Peñuela (2015) compared the Modified Kovacs as well with lab tests performed according to Fredlund and Xing (1994). Peñuela (2015) states that the results were highly comparable, indicating that the use of this method might be of practical use in general geotechnical practice, if the long time required to determine the parameters in the laboratory tests is not available. Therefore the Modified Kovacs was used in this research as well.

The Modified Kovacs model considers that water is held by capillary forces and adhesive forces, which both are calculated independently. The capillary saturation is obtained from a cumulative pore size distribution function, while the equation for the adhesive saturation is given by an interaction law with van der Waals type attraction between grain surface and water dipoles. The capillary component is more important at relatively low suction values while the adhesive component becomes dominant at higher suction when most

capillary water has been withdrawn. Both components are added together and converted to the volumetric water content θ as shown in equation 2.18 to 2.23.

$$S_r = \frac{\theta}{\eta} = 1 - \langle 1 - S_a \rangle (1 - S_c) \tag{2.18}$$

$$S_c = 1 - (h_{co}/\Phi)^2 + 1]^m exp[-m(h_{co}/\Phi)^2] \tag{2.19}$$

$$S_a = a_c * C_\Phi \frac{(h_{co}/\Phi_n)^{2/3}}{e^{1/3}(\Phi/\Phi_n)^{1/6}} \tag{2.20}$$

$$C_\Phi = 1 - \frac{ln(1 + \Phi/\Phi_r)}{ln(1 + \Phi_0/\Phi_r)} \tag{2.21}$$

$$h_{co}(cm) = \frac{0.75}{[1.17 * log(C_u) + 1]e * d_{10}} \tag{2.22}$$

$$\Psi_r(cm) = 0.86\sqrt{h_{co}} \tag{2.23}$$

Where S_r = Degree of saturation (-)
θ = Volumetric water content (m^3/m^3)
η = Initial porosity of the soil (-)
S_a = Adhesion component of the degree of saturation (-)
S_c = Capillary component of the degree of saturation (-)
h_{co} = Equivalent capillary height related to an equivalent pore diameter and the solid surface area (cm)
ρ_s =Density of the soil grain in (kg/m^3)
Φ_r = Soil suction represented as a head or length (cm)
m = Pore-size coefficient taken as $1/C_u$ (-)
a_c = Adhesion coefficient (0.01) (-)
Φ_n = Normalization parameter equal to 1 (-)
Φ_0 = Suction head corresponding to complete dryness (cm)
d_{10} = Diameter corresponding to 10% passing on the grain size distribution (cm)
C_u = Uniformity coefficient equal to d_{60}/d_{10} (1.96) (-)

Maqsoud et al. (2012) developed an extension on the Modified Kovacs model to predict hysteresis in the water retention curve. This was done summarizing all possible mechanisms for hysteresis in a single parameter, the contact angle, as this was identified as the main cause of hysteresis. The contact angle for sandy soils is proposed as values between 30°and 80°. Because the material in the area of the Delta21 project consists out of a pure sand a low 30°was chosen here. The estimated SWRC by the Modified Kovacs with hysteresis is shown in figure 2.13.

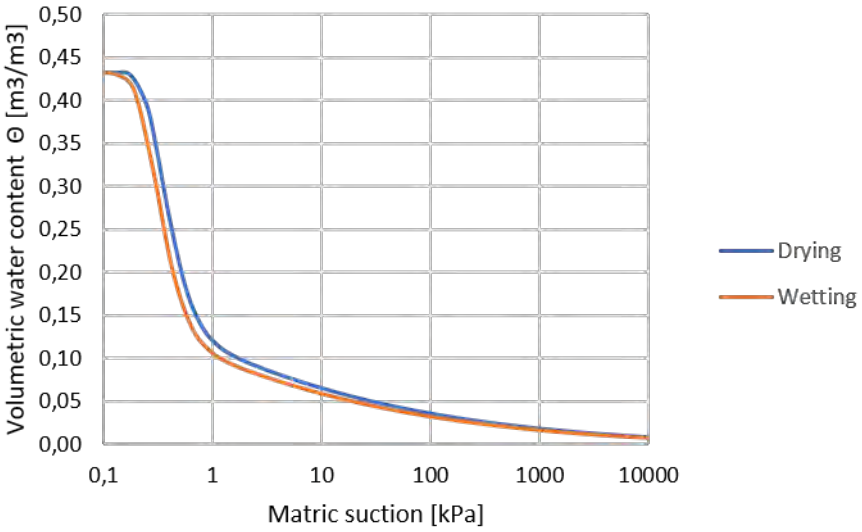

Figure 2.13: Soil water retention curve found with Modified Kovacs method (Kovács, 2011)

2.4.5. Hydraulic conductivity in unsaturated conditions

As described in section 2.2.4 the hydraulic conductivity reduces in the unsaturated zone. The relative hydraulic conductivity (K_r) is the ratio between the unsaturated hydraulic conductivity to the saturated one. $K_r = K_{unsat}/K_{sat}$, which is a ratio between 0 and 1, where 0 represents no flow and 1 the hydraulic conductivity as in the saturated zone. The method of Burdine et al. (1953) is used to find the relationship of relative hydraulic conductivity to pressure head ψ. It can be expressed by the following formulation:

$$K_r(\theta) = \theta_e^{\alpha} \left[\frac{\int_{\theta_r}^{\theta} \psi^{-\beta}\, dy}{\int_{\theta_r}^{\theta_s} \psi^{-\beta}\, dy} \right] \tag{2.24}$$

with

$$\theta_e = \frac{\theta - \theta_r}{\theta_s - \theta_r} \tag{2.25}$$

Where α = Emperical parameter equal to 2 (-)
β = Emperical parameter equal to 2 (-)
θ_s = saturated volumetric water content (-)
θ_r = residual volumetric water content taken as 0.01 (-)

The relationship between the relative hydraulic conductivity to pressure head for the Geba sand is shown in figure 2.14.

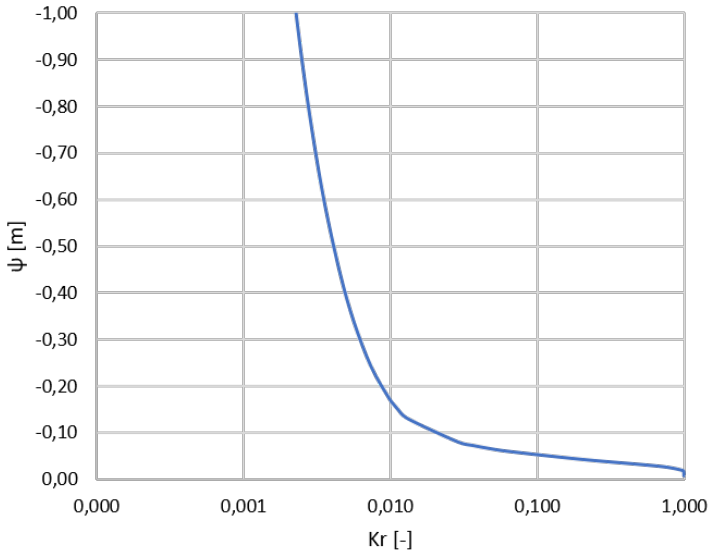

Figure 2.14: Relative hydraulic conductivity function after Burdine et al. (1953)

2.4.6. Shear modulus reduction curve

The dynamic shear modulus (G) represents soil stiffness in shear. It is valuable in proper evaluation of soil response to dynamic loads. Figure 2.15a shows a hysteresis loop, the path of stress versus strain during cyclic loading. The secant shear modulus of the soil element changes with the cyclic shear strain amplitude, which is large at low strain amplitudes and decreases as the shear strain amplitude increases. As shown in figure 2.15b, the locus of tips of the hysteresis loops of different cyclic shear strain amplitudes form the backbone curve. At the origin the maximum value of the shear modulus G_{max} can be found. At greater shear strain amplitudes, the modulus ratio G/G_{max} drops to values less than one. Therefore, to precisely represent the behaviour of the soil under the cyclic loading, both G_{max} and modulus reduction curve are required (Xu and Fatahi, 2015).

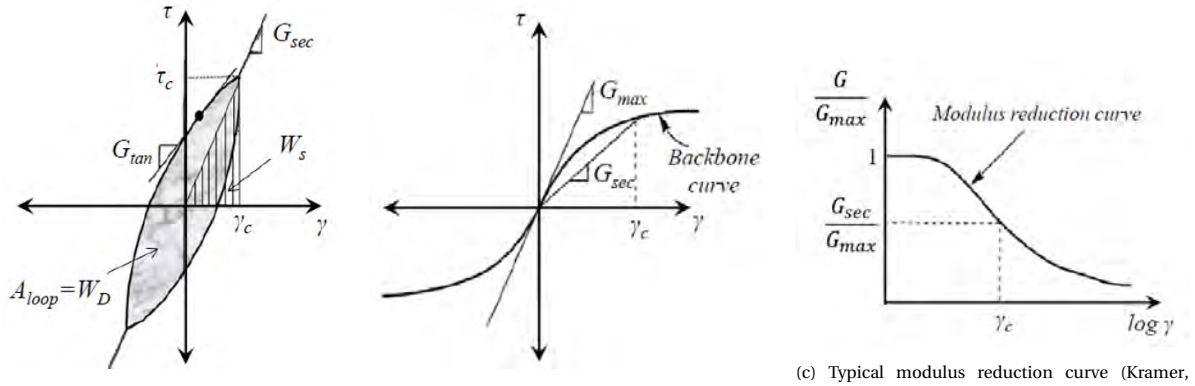

(a) Hysteretic stress-strain relationship

(b) Backbone curve

(c) Typical modulus reduction curve (Kramer, 1996))

Figure 2.15: Stress strain relationships adapted from Kramer (1996))

Finding the modulus reduction curve with cyclic triaxial systems is rare and difficult, because of the small strain ranges (Ghayoomi et al., 2017). Therefore the method proposed by Hardin and Black (1966) is used:

$$G_{max} = A\frac{(a-e)^2}{1+e})\left(\frac{p}{p_{atm}}\right)^n p_{atm} \tag{2.26}$$

A, a and n are constants specified for different sands based on roundness of the grains. The proposed constants by Wichtmann et al. (2015) are used:

$$A = 1563 + 3.13 * C_u^{2.98} \tag{2.27}$$

$$a = 1.94exp(-0.066C_u) \tag{2.28}$$

$$n = 0.4C_u^{0,18} \tag{2.29}$$

These results in a G_{max} of 108.6Mpa. With this Stokoe's equation can be filled in to get the S shaped small strain stiffness curve (Stokoe et al., 1999):

$$\frac{G}{G_{max}} = \frac{1}{1 + (\gamma/\gamma_r)^{\alpha}} \tag{2.30}$$

with :

$$\gamma = 6.521^{-4} exp|-0,59ln(C_u)| \tag{2.31}$$

For a discussion of various empirical equations for damping ratio the interested reader is referred to Wichtmann and Triantafyllidis (2013). There it has been demonstrated that the previous mentioned empirical relationship are suitable to reproduce a large number of experimental data for various sands collected from the literature. Furthermore, it has been shown that the extended empirical formulas work well also for stepwise-linear, gap-graded, S-shaped and other smoothly shaped grain size distribution curves (Wichtmann et al., 2015).

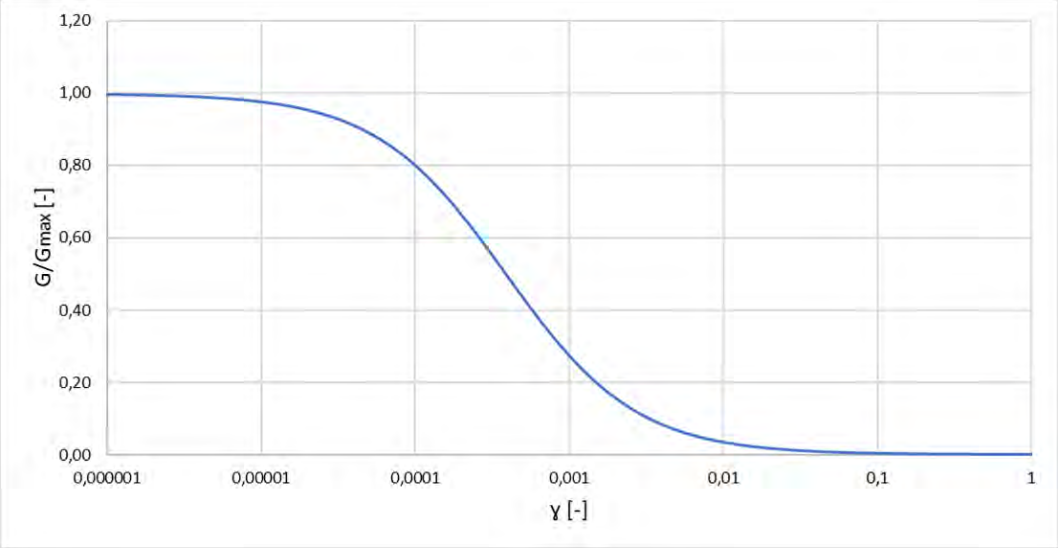

Figure 2.16: Modulus reduction curve

2.4.7. Summery geotechnical properties

A summery of the geotechnical properties for the three different sand layers shown in figure 2.12 are captured in table 2.4. This table presents the most important geotechnical properties of the sand together with the modulus reduction curve shown in 2.16 and the hydraulic parameters, shown in figure 2.13 and 2.14.

Geotechnical properties sand Delta21 dike		layer 1	layer 2	layer 3
Relative density [-]	γ_{sat}	0.75	0.30	0.64
Porosity [-]	γ_{sat}	0.38	0.43	0.39
Saturated weight [kN/m^3]	γ_{sat}	20.2	19.5	20.1
Unsaturated weight [kN/m^3]	γ_{unsat}	16.4	15.2	16.2
Stress dependent stiffness modulus for primary loading [kN/m^2]	E_{50}^{ref}	37000	37000	37000
Oedometer stiffness modulus [kN/m^2]	E_{oed}^{ref}	35000	35000	35000
Stress dependent stiffness modulus for re- and unloading [kN/m^2]	E_{ur}^{ref}	147000	147000	147000
Cohesion [kN/m^2]	c'_{ref}	0	0	0
critical state friction angle[°]	φ	33	33	33
Dilatancy angle [°]	ψ	3	3	3
Youngs modulus [-]	v	0.2	0.2	0.2
Reference pressure [kN/m^2]	P_{ref}	100	100	100
Coefficient of lateral earth pressure [-]	k_0	0.46	0.46	0.46
Permeability [m/day]	$K_x = K_y$	5.82	8.36	5.49

Table 2.4: Soil parameters sand used in Delt21 dike

3

Modelling Methodology

3.1. Numerical model with PLAXIS2d

The results from the centrifuge model are compared with the results from PLAXIS2D, a Finite Element Model (FEM). This is a numerical method where the 2D dike and subsoil get divided into a number of smaller elements. From the nodes of the elements the balance equations can be solved. Every time step the equations for all the smaller elements are solved and are then put together to approximate the solution for the entire, large, complicated model. For soils and groundwater flow, PLAXIS is a widely used FEM-program as it is user friendly, but can still incorporate a lot of features found in the real world. As the posed problem is represented in 2 dimensions, PLAXIS 2D is used for the calculations. Within PLAXIS a special module is developed called PLAXflow which is used to calculate pore water pressures in the soil subjected to changing hydraulic circumstances.

Dilatancy in the dike can cause shear effects which generate additional pore water pressures. Therefore it is not correct to think that in case of rigid material only flow based analysis is sufficient (Pinyol et all, 2008). A fully coupled flow-deformation analysis in PLAXIS can solve the full interaction between deformations, consolidation and groundwater flow simultaneously in the same phase. This calculation combines staged construction and transient groundwater flow. It considers a reduced permeability and degree of saturation in unsaturated zone. In the following section an explanation is provided about the calculations of PLAXIS based upon the theory on unsaturated flow from section 2.2.

3.2. Groundwater flow in the coupled analysis

To describe the hydraulic behavior of unsaturated soils a Soil Water Retention Curve (SWRC) is used. The SWRC describes the capacity of the soil to keep water at different stresses by relating the volumetric water content $\vartheta$and suction ψ. There are many models that describe the hydraulic behaviour of unsaturated soils. However, these require many soil parameters. Therefore PLAXIS gives another option of finding the SWRC by using the textural classification of the soil. Based on particle fraction the soil is placed in a textural class such as sand, silty sand and clay. A general set of hydraulic parameters is given to every soil placed in a that textural class.
Several data sets are developed which use different definitions of the textural classes and different assigned hydraulic parameters. The USDA soil textural triangle uses twelve different classes while the Hypres data set uses only six.

3.2.1. Bishop's effective stres

The effective saturation is used to calculate suction according to Bishop's stress. Furthermore, it has influence on the unsaturated hydraulic conductivity and is used as a ratio between the unsaturated and saturated weight.

$$S_{eff} = \frac{S - S_{res}}{S_{sat} - S_{res}} \tag{3.1}$$

Where S_{eff} = Effective saturation
S_{res} = Residual saturation
S_{sat} = Saturation level of the pores

The effective saturation is multiplied with the matric suction to prevent the suction to become unrealisticly large at low water content. At full saturation Bishop's stress is equal to Terzaghi's stress. (Galavi, 2010). During this research suction is taken as as a negative pressure.

$$\sigma' = (\sigma - u_a) + S_{eff}(u_a - u_w) \tag{3.2}$$

Where σ' = Effective stress
σ = Total stress
u_a = Unit weight of the pore fluid
S_{eff} = Effective saturation
u_w = Pore water pressure

3.3. Factor of safety

To find the factor of safety, the phi/c reduction or strength reduction method is used. Hereby the parameters $tan(\phi')$ and cohesion (c') as well as the tensile strength are successively reduced until failure of the structure occurs. The dilatancy angle is constant, only when the friction angle is equal to the dilatancy angle, these is lowered as well. The ratio available strength and strength at failure gives the safety factor at failure.

$$\sum Msf = \frac{tan\phi'_{input}}{tan\phi'_{reduced}} = \frac{C'_{input}}{C'_{reduced}} = \frac{s_{u,input}}{s_{u,reduced}} = \frac{Tensilestrength_{input}}{Tensilestrength_{reduced}} \tag{3.3}$$

When collapse is reached, PLAXIS stops calculating because of unrealistically large deformations. Collapse is assumed when the applied load reduces in magnitude in X successive calculation steps and the current stiffness parameter (CSP) is less than 0.015. The CSP is defined as:

$$Stiffness = \int \frac{\Delta\epsilon * \Delta\sigma}{\Delta\epsilon\Delta^e\Delta\epsilon} \tag{3.4}$$

This measures the amount of plasticity occurring. The CSP parameter is used in the calculation for the global error. The global error is defined as:

$$Global\,error = \frac{|\,unbalance\,force\,|}{|\,load_{currently\,activated}\,| + CSP * |\,load_{previously\,activated}\,|} \tag{3.5}$$

Where the unbalance force is the difference between the external and internal reactions. The global error is fixed to 1%. The denominator becomes smaller close to failure due to reduced stiffness and less load added. Therefore the unbalance is lower close to failure (R, 2020).

3.4. Constitutive models for unsaturated soils

For the simulation of soil behaviour several models can be applied in PLAXIS. In this report the Mohr-Coulomb and the Hardening soil with small strain stiffness (HSsmall) will be discussed.

3.4.1. Mohr-Coulomb model

Framework
The Mohr-Coulomb is a well-known linear-elastic perfectly-plastic stress strain model. Since soil behaviour is nonlinear and depends at least on stress level, stress path and strain level, this is a simplified approach. Still it gives a reasonable first order of the stress-strain relationship of a soil and can therefore be very well used for a first estimation of soil behaviour. The Mohr-Coulomb model uses a constant average stiffness, which results in fast computations.

The failure criterion is an extension of the friction law of Coulomb to general stress states. The occurrence of plastic strains can be determined using a so called 'yield function' which is denoted with f. The failure surface of the Mohr-Coulomb model is a cone with a hexagonal cross section in the deviatoric stress space and can be seen in figure 3.1. The hexagonal shape is caused by a combination of six yield functions. When one of the functions has the condition $f = 0$ plastic yielding occurs. Before that pure elastic strain are generated.

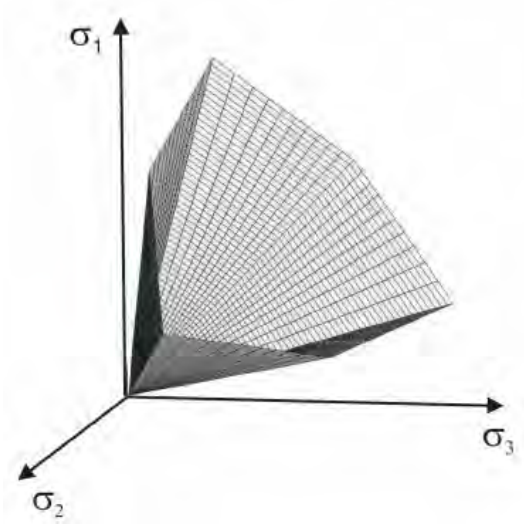

Figure 3.1: Mohr-Coulomb yield surface in principal stress space (Plaxis, 2019)

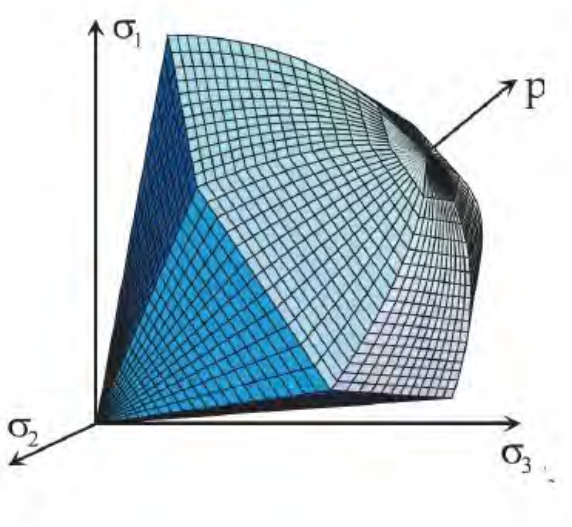

Figure 3.2: HSsmall yield surface in principal stress space (Plaxis, 2019)

For the determining the direction and magnitude of plastic straining, a plastic potential function g is introduced. In plasticity a distinction can be made between associated and non-associated plasticity. With associated plasticity the yield function and plastic potential function are the same and the direction of plastic strains is normal to the yield surface. As a result of this assumption a symmetric elasto-plastic material stiffness matrix is obtained. This reduces the calculation time. However, a non-associated plasticity framework is used in this model because theory of associated plasticity will overestimate dilatancy.

Results of existing studies on numerical simulation of the problems by Mohr-Coulomb constitutive model revealed that this model offers reasonably accurate results for frictional materials such as sand and gravel(Vermeer and De Borst). However, there are several disadvantages. It has a constant average stiffness for primary re- and unloading at different stress levels, which can cause inaccurate deformations. The MC model is not a critical state model and does not include time-dependency (creep) (Plaxis, 2019).

Parameters
The Mohr-Coulomb model only requires the parameters shown in table 3.1, which can be obtained from basic tests on soil samples.
In some problems an area with tensile stresses may develop. Failure due to tension instead of shear can be included with the Tension cut-off and tensile strength. In this case Mohr circles with positve principal stresses are not allowed.

E	:	Young's modulus	$[kN/m^3]$
ν	:	Poisson's ratio	[-]
C	:	Cohesion	$[kN/m^2]$
φ	:	Friction angle	[°]
Ψ	:	Dilatancy angle	[°]
σ'	:	Tension cut-off and tensile strength	$[kN/m^2]$

Table 3.1: Required soil parameters for Mohr-Coulomb model

3.4.2. Hardening soil model

Framework
The Hardening soil is a second order model often used for sand like materials. It is like the Mohr-Coulomb an elastoplastic model and both the shear locus and the yield cap have the hexagonal shape of the classical Mohr-Coulomb yield surface as can be seen in figure 3.2. In contrast to the MC model, the yield surface of a hardening plasticity model is not fixed in principal stress space, but it can expand due to plastic straining. Two different types of hardening can be distinguished:

Shear hardening: This type of hardening is used to model irreversible strains due to deviatoric loading.

Compaction hardening: This type of hardening is used to model irreversible strains due to compression in oedometer loading and isotropic loading situations.

The 2D representation of the yield surface in mean -deviatoric stress space is represented in figure 3.3. The cohesion is equal to zero in this figure. Since the Hardening soil model obeys the linear Mohr-Coulomb failure criterion, the state of stress in plastic range is described by means of friction angle and cohesion as for the MC model.

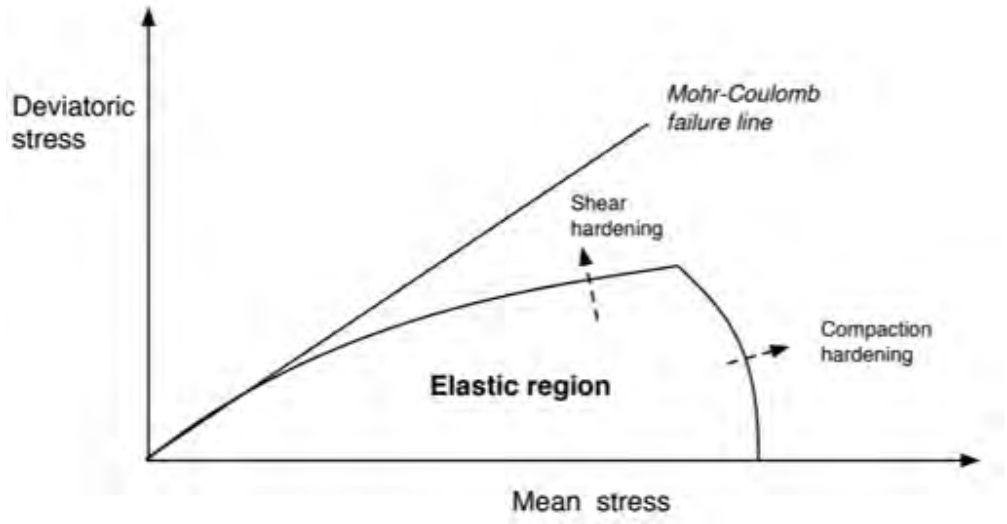

Figure 3.3: yield surface of the HSsmall model in mean-deviatoric stress space

Parameters
Some parameter of the MC model coincide with parameters of the hardening model.

Failure parameters as in Mohr-Coulomb :			
E	:	Young's modulus	kN/m^3
ν	:	Poisson's ratio	[-]
C	:	Cohesion	$[kN/m^2]$
φ	:	Friction angle	[°]
Ψ	:	Dilatancy angle	[°]
σ'	:	Tension cut-off and tensile strength	$[kN/m^2]$
Basic parameters for soil stiffness:			
E_{50}^{ref}	:	The drained triaxial loading stiffness	$[kN/m^2]$
E_{oed}^{ref}	:	The oedometer primary loading stiffness	$[kN/m^2]$
E_{ur}^{ref}	:	The drained triaxial unloading/reloading stiffness	$[kN/m^2]$
m	:	Power for stress level dependency of stiffness	[-]
Advanced parameters			
ν_{ur}	:	Poisson's ratio for unloading/reloading	[-]
p^{ref}	:	Reference stress	$[kN/m^2]$
K_0^{nc}	:	The K_o value for normal consolidation	[-]
R_f	:	Failure ratio q_f/q_a	[-]
σ_t	:	Tensile strength	$[kN/m^2]$
G_0^{ref}	:	Reference shear modulus at very small strains ($\eta < 10^{-6}$)	$[kN/m^2]$

Table 3.2: Required soil parameters for HSsmall model

Soil stiffness is described by defining three different stiffness corresponding to the loading condition as:E_{50}^{ref} ,E_{ur}^{ref} and E_{oed}^{ref}. This results in much more accurate soil stiffness as described in figure 3.4. As disadvantage more soil parameters are necessary.

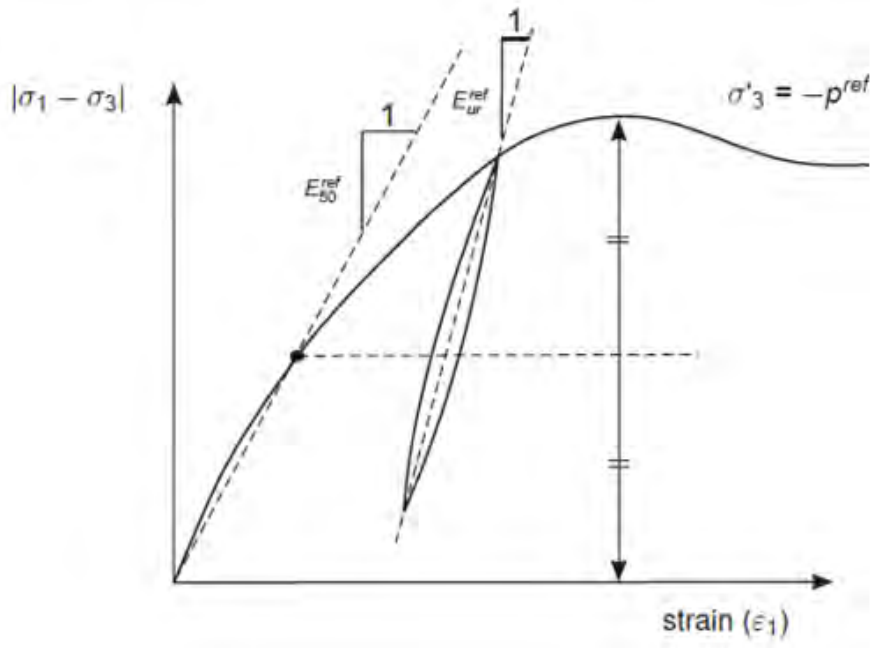

Figure 3.4: Defenition of E_{50}^{ref} and E_{ur}^{ref} for drained triaxal test results (Plaxis, 2019)

3.4.3. Hardening soil model with small-strain stiffness

The addition of the HSsmall model is a modification of the HS model that accounts for increased stiffness of soils at small strains. At low strain levels most soil exhibit a higher stiffness. To describe this behaviour an additional two parameters; the small-strain shear modulus G_0^{ref} and the shear strain level at which the hear modulus has reduced to about 70% of the small-strain modulus $\gamma_{0.7}$. (Vermeer and De Borst). The degradation of stiffness with increasing strain is described by a hyperbolic law developed by Dos Santos and Gomes Correia (2001):

$$\frac{G_s}{G_0}\frac{1}{1+0.385*\frac{\gamma}{\gamma_{0.7}}} \tag{3.6}$$

This relationship holds when the value of G lies between G_o and G_{ur} (unloading reloading shear modulus). Between these values there is a degradation of stiffness. When G decreases G_{ur} the behaviour is dominated by the model parameters E_{50}^{ref} and E_{oed}^{ref}

Another advantage of the HSsmall model is the introduction of hysteretic material damping during dynamic calculations. This is visualized in figure 3.5. Starting from the small-strain shear stiffness G_0, the actual stiffness will decrease with increasing shear strain. Upon load reversal the stiffness will restart from G_0 and will decrease again until the next load reversal. This can cause weakening when multiple cycles of loading are applied. (Plaxis, 2019).

The main advantages of the HSsmall model compared to the MC model are the estimation of stiffness and hysteresis. The increase in necessary soil parameters are a drawback. Soil stiffness has minor influence on the stability as mentioned earlier in the literature review in chapter 2.1. However, the addition of hysteretic behaviour can give insight in the effect of multiple cycles of loading on stability. Therefore the HSsmall model is chosen to be used further in this research.

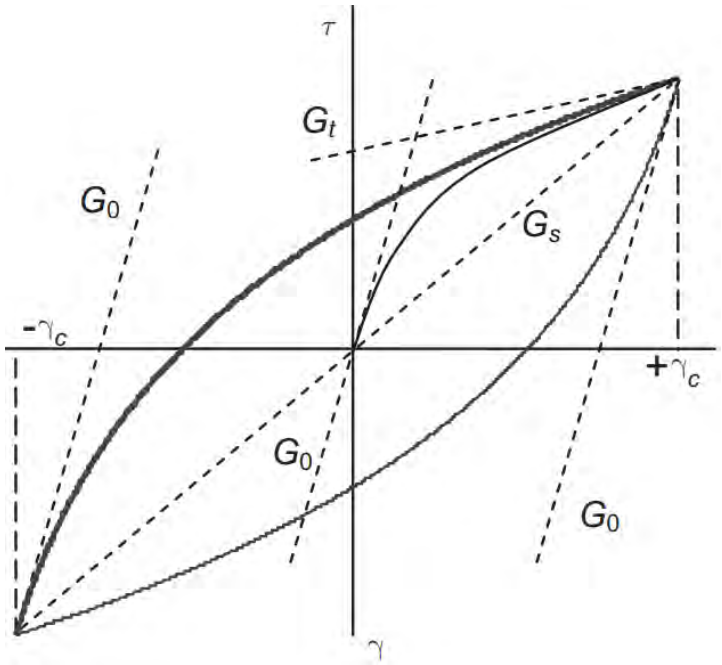

Figure 3.5: Hysteretic behaviour in the HSsmall model (Brinkgreve et al., 2007)

4

Verification

To understand and to verify the correctness of the numerical model it was compared with several tests found in literature. Full scale tests are preferred, because they offer the closest resemblance to situations in the field. For a good comparison between a full scale test and a numerical model, the full scale test or field test needs to have certain components. First of all, to check if the factor of safety is correct, the field model needs to fail and preferably only due to rapid draw down. A combination of failure causes like earthquakes or construction work make verification more difficult. Secondly, a simple homogeneous dam made of sand is preferred. The numerical model is limited to 2D and fractures and other heterogeneous soil characteristics are difficult to mimic. Thirdly extensive measurement data and documentation of the field test needs to be accessible. A field test subjected to all of the desired requirements could not be found. Therefore besides a field test, two centrifuge tests are used.

The first centrifuge test described is a test executed by Deltares. It has the purpose to validate the failure contour and FoS of the numerical model. With a second centrifuge test, performed by the ETH Zurich the pore pressure and saturation level will be validated. And last of all the pore pressure development will be double checked with a field test.

Centrifuge modelling is exploited as it can partly overcome the scaling problems induced when using a small scale model. Therefore it can give understanding in the failure mechanism, effect of the parameters and validation of the numerical model. In the centrifuge tests a model with geometry N times smaller than the prototype is constructed and is tested under centrifugal acceleration field with magnitude of N times the Earth's gravity (schofield 1980). This situation provides a gradient of body stresses within the model similar to the prototype, which ensures similar effective stresses and groundwater pressures at equivalent depths. Centrifuge modelling enables the geotechnical engineer to replicate complex features in an inexpensive and time-efficient way (Taylor, 2018).

4.1. Scaling laws explained

Due to the difference in scale between the prototype in a centrifuge and the field-model scaling laws apply. The ratio between the dimensions of parameters between the prototype and field model, the modelling scale, can be defined as follows:

$$D_M / D_P = 1/N \tag{4.1}$$

Where N is the modelling scale. The most important scaling laws for physical modelling rapid draw down conditions in the centrifuge can be found in table 4.1. The theory behind the scaling ratio's is explained in appendix C.

Term [Dimension]	Prototype	Model
Length (macroscopic) [L]	1	1/N
Length (grain scale) [L]	1	1
Seepage velocity (macroscopic and grain scale) [L/T]	1	N
Seepage time /(macroscopic) [T]	1	$1/N^2$
Seepage time /(grain scale) [T]	1	$1/N^2$
Time	1	$1/N^2$
Hydraulic gradient (macroscopic) [L/L]	1	N
Density	1	1

Table 4.1: scaling laws of the geotechnical centrifuge

4.2. Deltares centrifuge test

The first of two centrifuge tests is executed by Deltares (Bezuijen and Den Adel, 2006). In this report the stability of a dike was investigated during loading with a ground water flow from the centre of the dike to both slopes. This was an loading situation for an existing dike where damage occured after a drink water supply-pipe broke. Different failure mechanisms were possible: 'Seepage from the core to the dike can endanger the slope stability due to slip circle instability.' and 'The seepage from the core creates a flow along the slope of the dike leading to erosion of the surface. To gain insight in the failure mechanisms of the damaged dike a series of centrifuge tests were performed with a increasing water pressure inside the dike. The test set up is described below.

The tests were preformed in a strongbox, made of 1 cm thick aluminium. The box is 0.9 m long, 0.2 m wide and 0.5 m high. A 5cm thick perspex window forms the front side of this box allowing for imaging during flight. The model is made with Baskarp sand and can be seen in figure 4.1. The strongbox was filled with de-aired water. Sand was poured into this water and compacted by repeatedly applying mechanical shocks to the strongbox, so the resulting relative density is roughly 60%. Excess water was drained until a slight under pressure was reached. The dike profile was carefully shaped out this volume of sand. At ground level underneath the crest of the dike a brass filter is present. By pressurizing this water supply, the phreatic level inside the dike can be raised. The pore pressure in the centre of the dike is slowly raised in steps of e.g. 5 kPa, during three minutes. Then the pressure is kept constant for roughly half an hour after each step in order to reach equilibrium and accumulation of possible damage. This procedure was repeated until serious damage had occurred. The steps of water level rising can be seen in table 4.2.

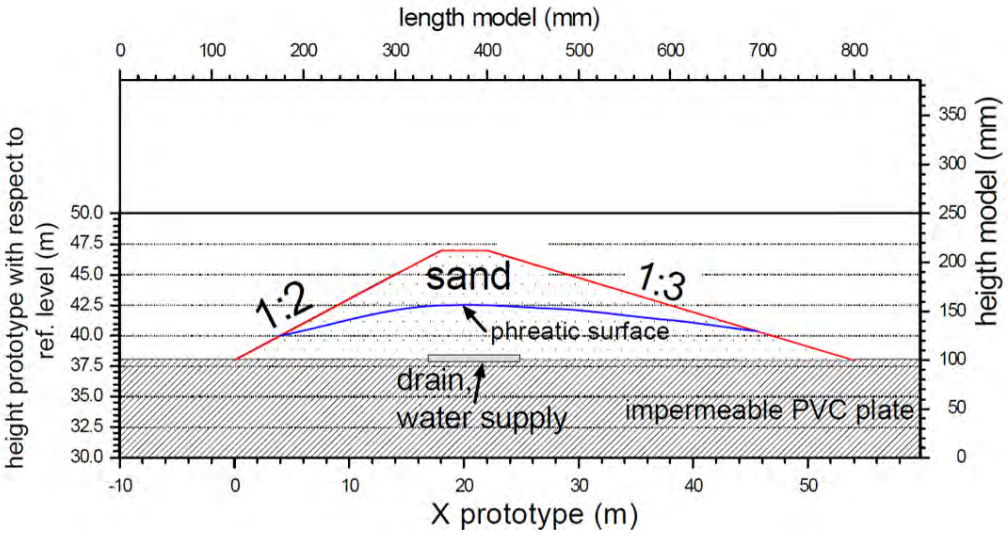

Figure 4.1: Test set-up of 1:80m model from Deltares centrifuge test (Bezuijen and Den Adel, 2006)

Step	Pressure [kPa]	Start (day)	End (day)
0	0	0,0	2,8
1	9,5	2,8	4,1
2	19,4	5,2	9,8
3	29,3	10,9	13,9
4	39,3	15,2	20,2
5	40,5	21,5	31,7

Table 4.2: Steps of increasing water pressure

The expected failure mechanism according to the dutch guidelines was macroscopic slope failure caused by a reduction in effective stress due to the hydraulic gradient (TAW, 2001). As described in section 4.1, both weight of the soil and hydraulic gradient have the same scaling factor N, similar to the corresponding upward force on an element. Therefore no problems were expected with the performance of a small scale model in the centrifuge. However, at the geotechnical chamber of Deltares, where the centrifuge is placed, a low ambient air pressure (5kPa) is applied for tests performed at 30g and higher. A lower air pressure influences the capillary pressure and therefore stability of the dike. To investigate the effect of air pressure several tests were performed at low g-levels and atmospheric pressure and tests at high g-levels with a lower air pressure. Afterwards it was concluded that the air pressure has only limited influence on the overall stability of the dike.

The expected macroscopic failure of the dike occurs just after the water pressure is increased for the fifth time in the test at 80g. Figure 4.4 shows the centrifuge model at this moment of failure. The crest is not smooth anymore and a larger body of soil has moved. At this moment the water pressure at the core is estimated to be 40.5kPa and the fissure occurs at the reference height of 1.5m. However, visibility is low and according to the paper: 'insufficient optical resolution of the video system prevents the observation of moving grains at Ng'. Still it can be seen in figure 4.3 have moved at the toe of the dike before the macroscopic failure. Grains have been flowing out at the toe of the dike and thus creating a micro instability as failure mechanism. Both the 1:2 and the 1:3.3 tests showed this micro instability. According to the Dutch guidelines for dike stability (TAW 1985 and TAW 2001) micro instability has a factor of safety of 1.2 for a slope of 1:3.3. Therefore it is concluded that the dutch guidelines underestimated micro instability for a sandy dike.

To find out how to prevent the micro instability, tests with a clay cover and one with a drain at the toe were performed. In the report is stated that the drain was an effective measure against micro instability. No micro instability was detected at the maximum load of the experiment, an internal pressure of 20kPa. To test the clay protection two tests were performed. One of them with a thick soft clay cover and an other one with a thin stiff clay cover. With the stiff clay cavities formed underneath the top layer and it did not increase the safety of the dike. With the thick soft clay layer it was expected that the clay would follow any deformations and therefore prevent the formation of cavities. But cracks were formed in the clay in which water flowed away. As a result the concentrated flow of water led to enhanced removal of sand. It was concluded that a clay cover does not contribute significantly in preventing micro instability.

Figure 4.2: Before visible deformation

Figure 4.3: Grains flush out at the toe

Figure 4.4: Larger failure (40.5kPa)

4.2.1. Numerical estimation of Deltares centrifuge test

The centrifuge test described before is simulated in a numerical PLAXIS model. A coupled analysis is executed in PLAXIS with a Mohr-Coulomb model. It does not use a HS small model because the needed stiffness parameters could not be found in reliable sources. In spite of using a different stress strain curve, The Mohr-Coulomb has the same failure criterion as the HS small model as earlier described in chapter 3.1. The soil class is chosen as 'coarse' from the Hypres data set, due to the soil size fragments. This is the coarsest soil class in the data set. From this class the input parameters for the Van Genuchten equation A.1 are taken, used for the water retention curve, which can be seen in appendix D.

Homogeneous soil parameters throughout the height of the dike are assumed. All geotechnical soil characteristics are similar to the centrifuge model as described in table 4.3. Not all soil characteristics could be found in the report, consequently the friction angle and stiffness are taken from another report which uses the same type of Baskarp sand (Dijkstra et al., 2008). Parameters as size and time are multiplied with the scaling laws described in Appendix C.

In figure 4.5 a cross section of the PLAXIS model can be seen. In PLAXIS only half of the dike is modeled, because it saves computational effort and time. Hereby the assumption is made that in the middle of the dike only vertical movements are occurring and no horizontal movement. The pressure is increased to 40.5kPa, because this was the pressure were macroscopic failure occurred in the centrifuge test.

Geotechnical properties Baskarp sand		
Saturated weight [kN/m^3]	γ_{sat}	19,9
Unsaturated weight [kN/m^3]	γ_{unsat}	16,0
Initial void ratio [-]	$e_{initial}$	0,34
Young's modulus[kN/m^2]	E	10000
Cohesion [kN/m^2]	c'	0
Internal friction angle [°]	φ	37
Dilatancy angle [°]	ψ	8
Poisson's ratio [-]	ν'_{ur}	0,2
Soil fragment [%]	<2 µm	10
Soil fragment [%]	2 µm - 50 µm	13
Soil fragment [%]	>50 µm	77
Permeability [m/day]	$K_x = K_y$	7.776

Table 4.3: Soil parameters Baskarp sand used in numerical model

4.2.2. Results numerical model and comparison with centrifuge model

The numerical model has a FoS of 2.05 before the water level increase and does not reach a FoS smaller than 1 until the water pressure is 40.1 kPa. The incremental deformation of the numerical model at this moment can be seen in figure 4.5 and zoomed in at the toe of the dike in figure 4.6. The incremental deformation is the deformation within the current calculation step. It is used here because it gives an indication of the shape of the failure contour. Figure 4.5 shows a small failure with the largest deformations at the toe of the dike. The shape of the failure contour looks quite similar and happens at almost the same time as in the centrifuge test (40.1 vs 40.5 kPa).

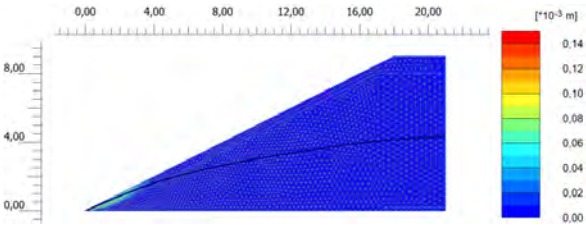

Figure 4.5: Incremental deformation at failure at 40.1 kPa, zoomed in at failure contour

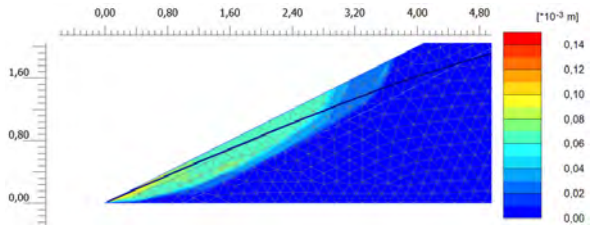

Figure 4.6: Incremental deformation at failure at 40.1 kPa, zoomed in at failure contour

Erosion

The pictures taken during the centrifuge test show that some grains have moved at lower pressure levels, flushed out by the water. The numerical model shows deformations at lower water pressure levels as well. The total deformation until the water pressure is increased to 22kPa predicted by the numerical model is shown in figure 4.7, figure 4.8 shows the zoomed in version. The numerical model shows some deformation due to the increased water level and larger deformations at the toe. It seems that PLAXIS, although it does estimate deformation at the toe, does not simulate the erosion well.

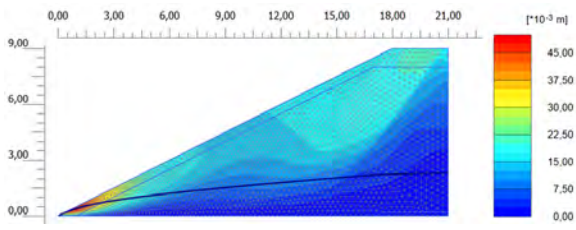

Figure 4.7: Total deformation until water pressure is at 22kpa at inlet

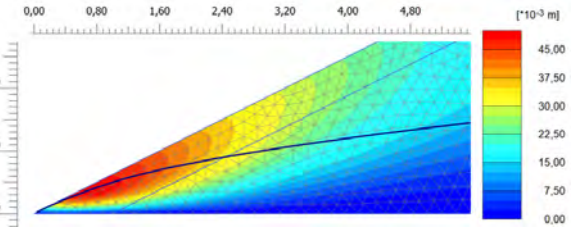

Figure 4.8: Total deformation until water pressure is at 22kpa at inlet ,zoomed in at failure contour

Addition of Cohesion

Last figures showed that the failure contour concentrates around the toe of the dike. One way to prevent grains from flushing out and the development of very small failures is the addition of cohesion. Therefore, in the top 0.5m a cohesion of $0.1 kN/m^2$ was added. However, as can be seen in figure 4.10, with the added cohesion the failure contour looks comparable as before. The FoS is again lower than 1 at 40.5kpa, indicating that overall stability is not significantly increased. The addition of cohesion is arguably not realistic in the field as well.

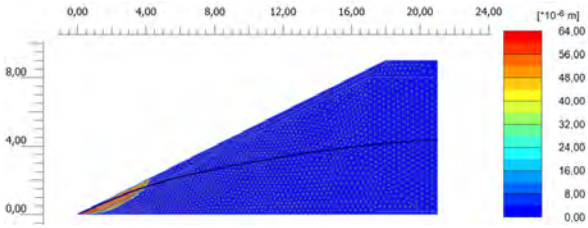

Figure 4.9: Incremental displacement of numerical model with extra cohesion, water pressure 40.5kPa at inlet

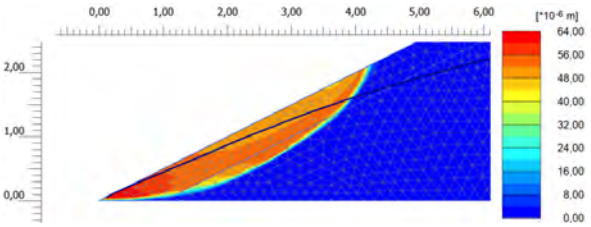

Figure 4.10: Zoomed in at failure contour of numerical model with extra cohesion, water pressure 40.5kPa at inlet

High permeable toe

To prevent hydraulic failure at the embankment, toe filter protection in the form of non-cohesive granular material is used more often since the 1970s (Brandl and Szabo, 2013). It is advices by Verruijt (2012) as good way to prevent failure by horizontal flow. It can be more realistically applied in the field than a addition of cohesion of the top layer. Therefore it is tested in the numerical model as well.

The toe filter is shown in figure 4.11. It is only 1m high of the total 9m height of the dike. It is made of a gravel, with a high permeability of 250m/day, an internal friction angle of 40°and zero cohesion. Other soil parameters can be found in table D.1 in appendix D.0.1. As can be seen in figure 4.12 the phreatic level is on average much lower than without the permeable toe, especially close to the drain. The size of the failure contour increased. Furthermore, the FoS is increased to 1.435 from FoS<1 for the previous modeling attempts. This can be due to the lower phreatic surface in the dike and the high internal friction angle of the gravel. Overall the use of a non-cohesive granular material as toe filter seems highly effective in increasing the stability of the dike.

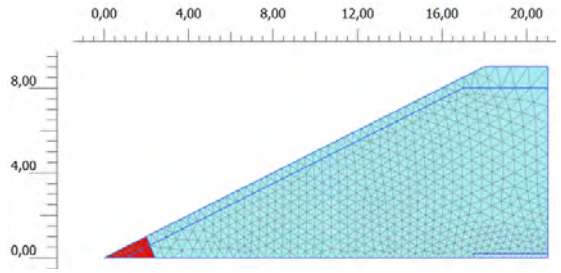

Figure 4.11: Shape of numerical model with high permeability toe, where high permeability toe is shown in red

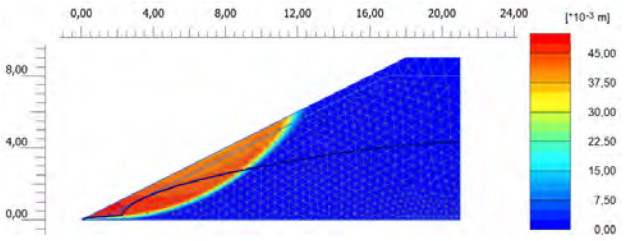

Figure 4.12: Incremental deformation of numerical model with high permeability toe, water pressure 40.5kPa at inlet

4.3. Centrifuge test of ETH Zurich

To confirm the correctness of the pore pressure and saturation level of the coupled analysis during heavily changing water levels, the numerical model is compared with a centrifuge test executed by Peñuela (2015).

The centrifuge test was part of a PhD research called 'River dike failure modeling under transient water conditions'. This research tries to consider the influence of infiltration and saturation changes on the failure mechanisms developed in the river dike. This is done by field testing, centrifuge testing and numerical modeling. While the field test focuses on a large part on the effects of overflow of dikes, the small scale tests look into rapid draw down conditions before overflow as well.

The centrifuge tests were performed as reference to the numerical model and to test the effect on stability of several different setups. These different setups were various slope angles, a cut-off wall and a toe filter.
The centrifuge test chosen to be compared with the PLAXIS model was made of homogeneous sand and has slopes 1:3. The cross section can be seen in figure 4.13. It has besides pore pressure tensiometers (PPT's), time domain reflectometry (TDR) sensors, which measures moisture content. A TDR works by sending electromagnetic waves along a coaxial cable to a sensor, which is placed in the soil. Part of the electromagnetic wave is reflected at the beginning of the sensor, caused by the impedance difference between the sensor and the cable. The remainder of the wave propagates through the sensor and is reflected at the end. By comparing the measured reflection to the initial pulse the average moisture content can be calculated by using an equivalent circuit as a reference (Noborio, 2001). The prototype was placed in a rounded strong box to prevent

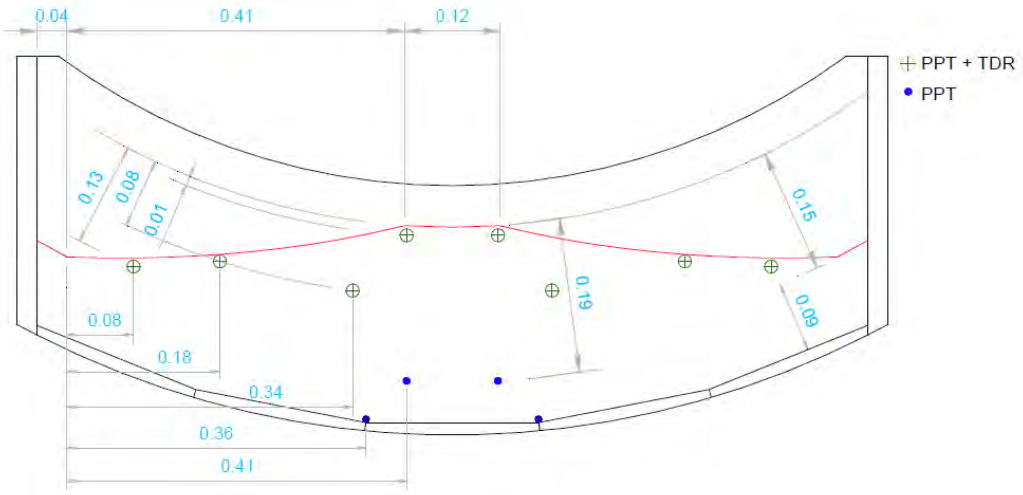

Figure 4.13: Cross section of the centrifuge model of the dike with slopes 1:3.0 (dimensions in m) (Peñuela, 2015)

the model in the corners of the box gaining extra centrifugal forces. To prepare the sample the box was filled completely with sand by dry pluviation, with particles falling freely with a small depositional intensity from a constant height of 0.90 m from the bottom of the box. Secondly, the sand was saturated by adding water from the bottom of the model until water height was slightly above the soil surface. Afterwards gravimetric water

content of 13% was achieved by using drainage and pumps. Lastly the sand is shaped by cutting away excess sand.

During the test a centrifugal force of 33.3g is used. Two cycles of water level lowering and rising are applied in the test before letting the dike overflow. The water level rise is shown in figure 4.18 as the applied water pressure. The part where the dike is overflown is not shown here.

In the centrifuge tests, no instability events were observed on the water-side slope during rapid drawdown. It was concluded that this was due to the high hydraulic conductivity of the soil, which allowed the pore water to drain and any residual pore water pressure to be dissipated rapidly. After overflowing the dike failure occurred and the research determined that a toe filter is highly effective in stabilising the dry side of the dike. The cut-off wall improved stability on the dry side of the dike slightly and increased the required time to failure. Nevertheless, it is not as effective as the toe filter. It is therefore recommended to prevent local instabilities. According to the research the results from their numerical simulations matched, in almost every sense, the results obtained from the centrifuge modeling. However, recommendation is given to use a coupled numerical model instead of the used decoupled numerical model, where the soil body is assumed to be rigid. Furthermore it is advised to pay close attention to the unsaturated soil mechanics which can be tricky. The SWRC used was not only measured in the lab but with an empirical formula as well.

4.3.1. Numerical estimation of centrifuge test

In the Numerical calculation of PLAXIS the Mohr-Coulomb model was used, similar to the previous verification due to insufficient data for the preferred HS small strain model. Furthermore coupled analysis is used. The shape of the model with the initial phreatic water level and the used mesh are shown in figure 4.14. The element size is around 60cm resulting in 468 elements, all with 15 nodes. A coarser mesh results in less accurate results and a faster computational time. It is assumed that this mesh is sufficiently accurate in estimating saturation and negative pore pressures. The centrifugal acceleration was 33.3, consequently the size of the numerical model is increased by the same factor. The model is made up from Perth sand with homogeneous properties shown in figure 4.4. These are the same properties as reported in the used paper.

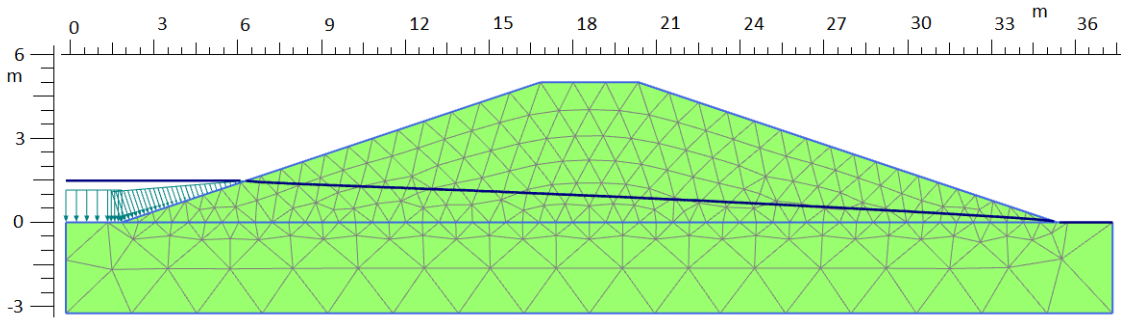

Figure 4.14: Mesh with water level of numerical model

Suction in the numerical model is based upon Bishop's law using the effective saturation. This is taken from the soil water retention curve (SWRC). To find the SWRC the Modified Kovacs method is used, described in section 2.4.4. The method of Burdine et al. (1953) is used for the relative hydraulic conductivity function. However, for these emperical relationships many soil parameters are needed. PLAXIS does give another option to find the SWRC. In this case the soil is placed in a textural class based on particle fraction, such as sand, silty sand and clay. A general SWRC and Relative hydraulic conductivity function are assigned to the soil class. Several data sets are developed which use different definitions of the textural classes and different assigned hydraulic parameters. The USDA soil textural triangle uses twelve different classes while the Hypres data set uses only six. For one of the numerical estimations the soil class is taken as 'coarse' from the Hypres data set. The SWRC connected with this soil class can be found in figure 4.15. The soil class used is the coarsest soil class in the Hypres data set, still it is not as coarse as the Perth sand of the centrifuge prototype. The soil fractions can be seen in table 4.5. For the third numerical estimation the USDA data set is used, which has more different soil classes and the coarsest soil class has a higher percentage of sand as can be seen in table 4.5.

Geotechnical properties of Perth sand		
Saturated weight [kN/m^3]	γ_{sat}	18,83
Unsaturated weight [kN/m^3]	γ_{unsat}	16,7
Initial void ratio [-]	$e_{initial}$	0,56
Young's modulus[kN/m^2]	E	28000
Cohesion [kN/m^2]	c'	0
Internal friction angle [°]	φ	31
Dilatancy angle [°]	ψ	1
Poisson's ratio [-]	v'_{ur}	0,35
Soil fragment [%]	<2 µm	6
Soil fragment [%]	2 µm - 50 µm	11
Soil fragment [%]	>50 µm	83
Permeability [m/day]	$K_x = K_y$	14,25

Table 4.4: Soil parameters Baskarp sand used in numerical model

soil class		>2 µm [%]	2 µm -50 µm [%]	50 µm -2 mm [%]
Centrifuge test	Perth sand	0	0	100
Hypres data set	coarse	10	13	77
USDA data set	sand	4	4	92

Table 4.5: particle size per soil class

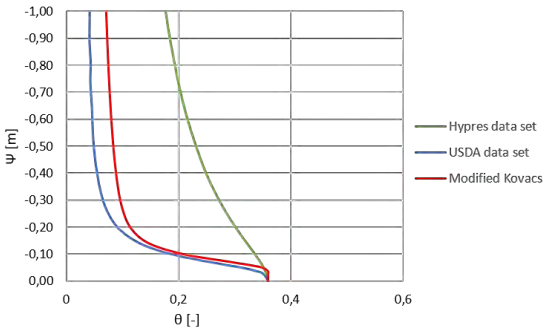

Figure 4.15: Soil water retention curve estimations of Perth sand

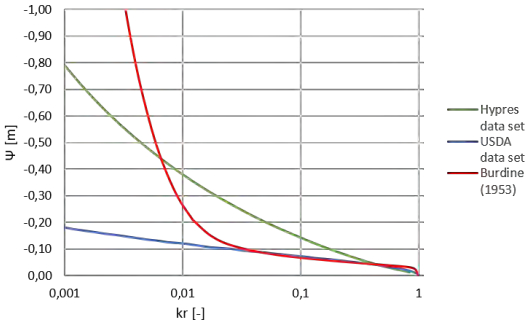

Figure 4.16: Estimation of the relative hydraulic conductivity function of Perth sand

In figure 4.19 the pore pressures of PPT1 is shown, it can be seen that the numerical estimations of the positive pore pressures are very accurate. However, when pore pressures are negative, the numerical results are poor. PPT 5 and 8, show the worst results and are therefore shown in figure 4.20 and 4.21.

Estimating the SWRC with the Hypres data set resulted in an overestimated suction. This could be due to the soil class being to fine. Due to the coarser grains it has a steeper soil water retention curve with less negative pore pressures at the same saturation level.
The numerical model with the SWRC from the USDA data set estimates the suction levels better. Nevertheless, suction is consistently underestimated.
The SWRC by the Modified Kovacs method based on Kovács (2011) make a slightly more accurate prediction. The pore pressure estimations are closely related to the results of the USDA data set, caused by a fairly similar SWRC.

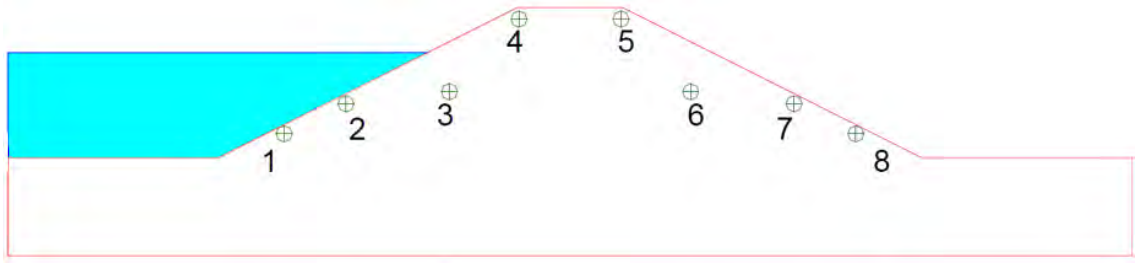

Figure 4.17: numbering of the sensors (Peñuela, 2015)

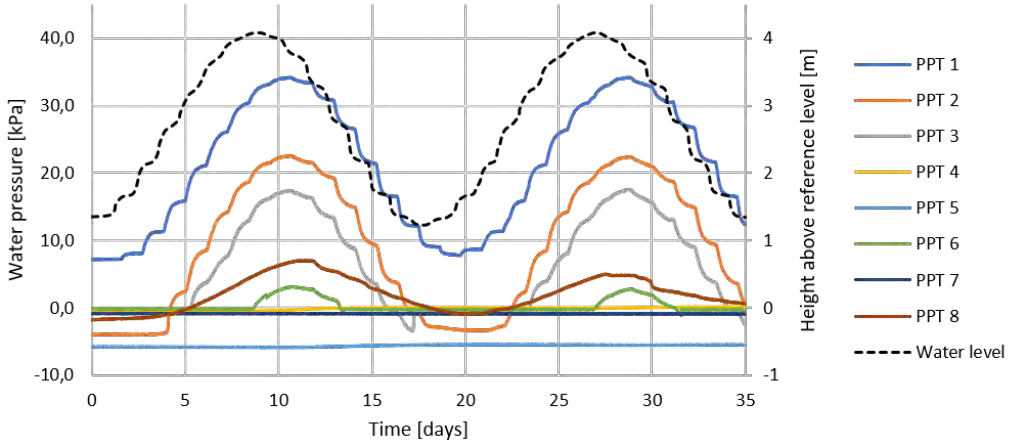

Figure 4.18: Pore pressure measurements of the centrifuge test done at the ETH university and applied water level change(Peñuela, 2015)

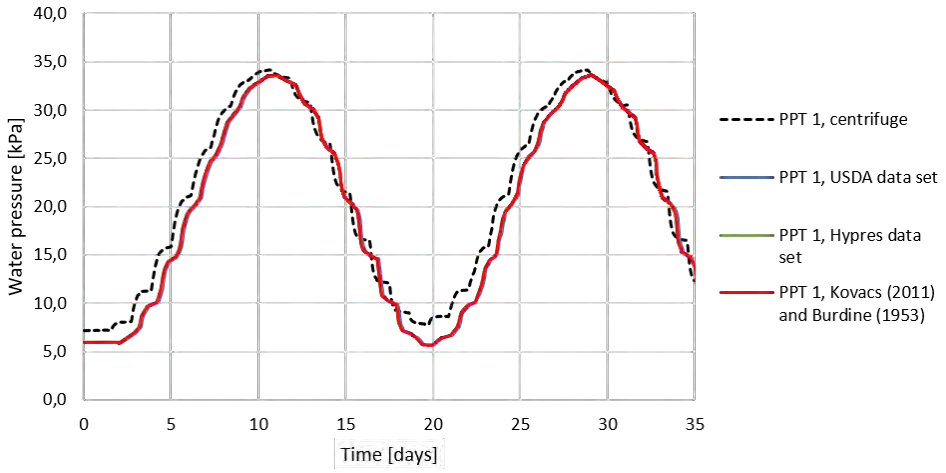

Figure 4.19: Pore pressure estimation of PPT 1

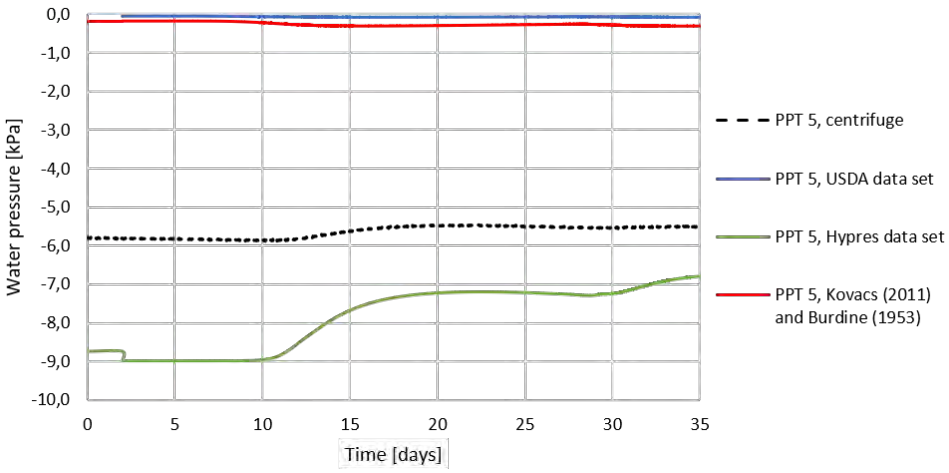

Figure 4.20: Pore pressure estimation of PPT 5

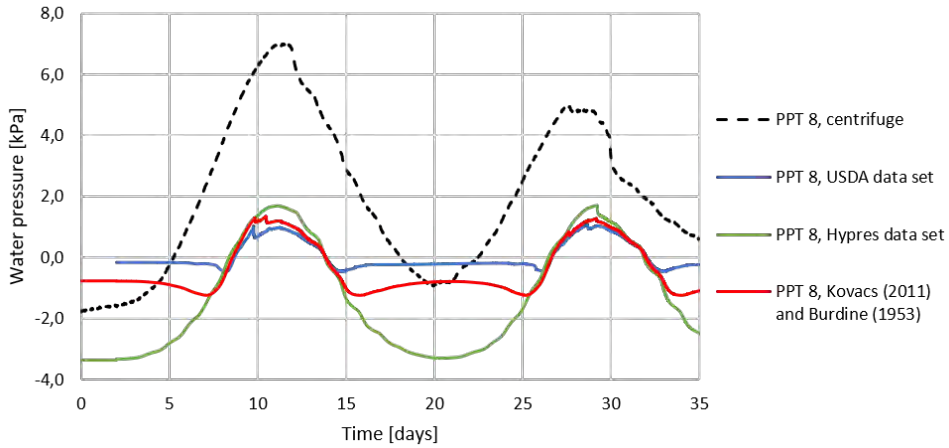

Figure 4.21: Pore pressure estimation of PPT 8

The volumetric water content was measured with TDR sensors. TDR 1,5 and 8 are shown in figure 4.23 4.24 and 4.25. Similar to the PPT results, it seems that the Hypres data set overestimates the saturation and the USDA data set underestimates the saturation. The method of Burdine et al. (1953) underestimates the saturation as well, although the results are slightly better. It is concluded that none of the three methods give reliable results of saturation and suction. The calculated unsaturated soil parameters from the empirical formulations give the most accurate results and will be further used in this research. Due to the underestimation of suction this method will develop conservative stability results.
Next to wrongly estimated input parameters for the SWRC, the nonexistence of hysteresis in the computed SWRC of PLAXIS can cause poor predictions of negative pore pressures. Negative pore pressures or suction increase stability in the area right above the phreatic water level. Due to poorly predicted suction in this area stability estimations are less reliable.

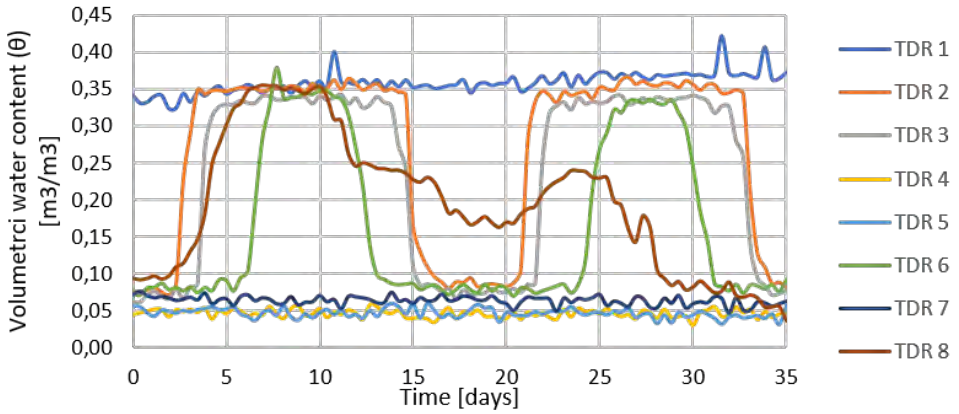

Figure 4.22: Volumetric water content measurements of the centrifuge test done at the ETH university (Peñuela, 2015)

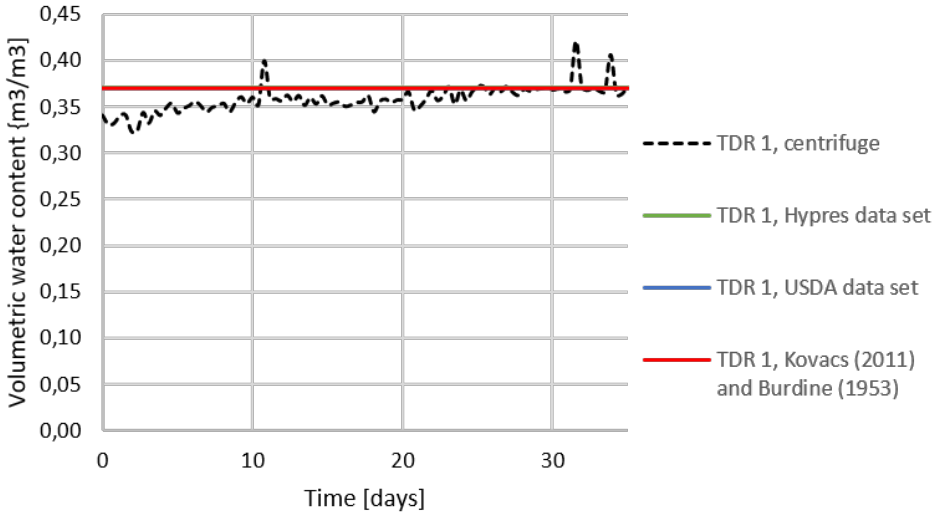

Figure 4.23: Volumetric water content estimation of TDR1

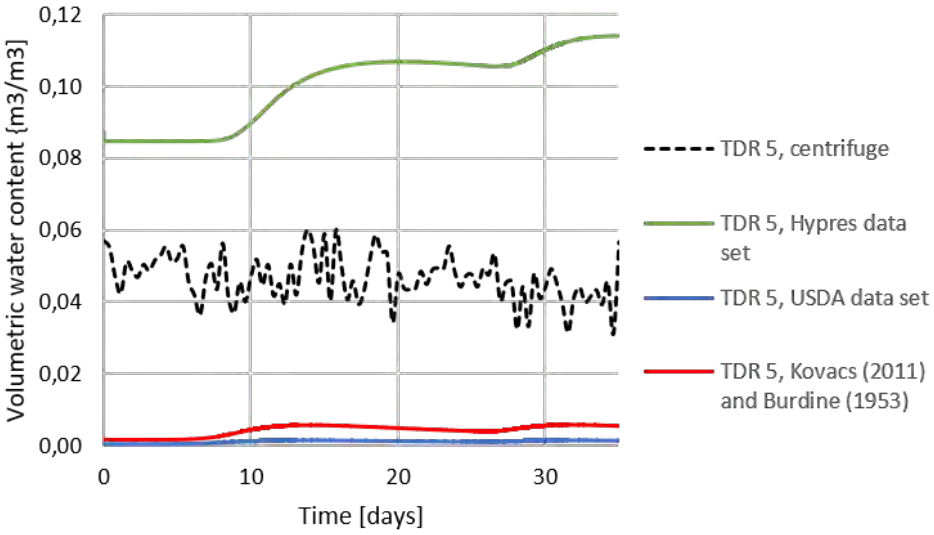

Figure 4.24: Volumetric water content estimation of TDR5

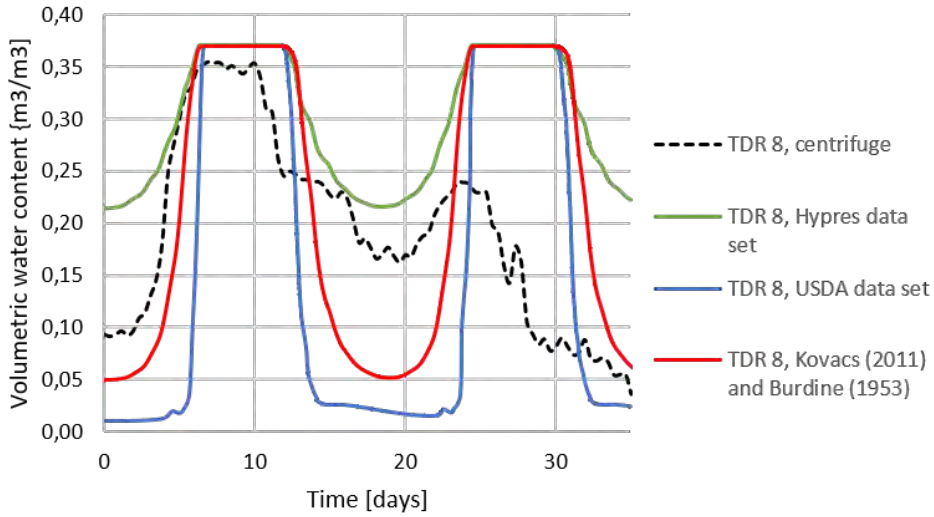

Figure 4.25: Volumetric water content estimation of TDR8

4.4. Glen Shira lower dam field test

The Glen Shira lower dam is chosen as field test to be analysed. It is part of a pumping storage scheme in Northern Scotland. The reservoir was expected to experience rapid drawdown rates and this situation prompted the field experience reported by Paton and Semple (1961). The dam consists of a concrete core wall reaching 16m high with a surrounding morainic fill. A graded filter and a rock fill, both with a higher permeability, form the outer layers of the dam. The morainic fill is a compacted non-plastic soil. According to Alonso Pérez de Agreda and Pinyol Puigmartí (2009) it is a well-graded material with a maximum size of 15cm. It has a much lower permeability than the previous used sands in this report. The rock fill has a high porosity of 0.4 and only a dry weight of 16.7 kN/m^3. Just like the graded filter it has a high permeability. For the model the graded filter has an estimated permeability of 100m/day. However, soil characteristics of the graded filter could not be found and are assumed, except for the permeability, to be similar to the rock fill. The dam is built in a single step on an impermeable rock layer. Alonso and Pinyol (2016) stated that the Glen Shira dam was probably the best-documented case histories concerning the effect of drawdown on earth dams. It does not experience failure, but the geometry can be modelled with PLAXIS and pore pressure sensors are in place.

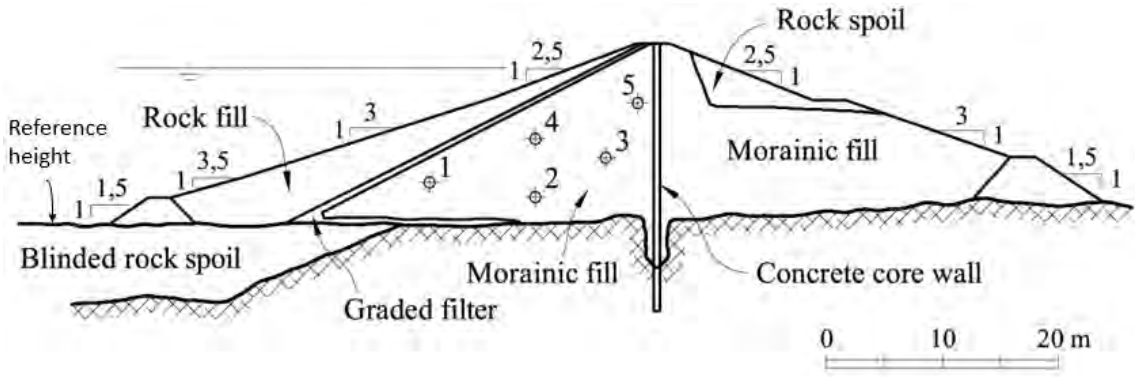

Figure 4.26: Cross section of the Glen Shira lower dam (Alonso Pérez de Agreda and Pinyol Puigmartí, 2009)

Geotechnical properties of Morainic fill and Rockfill			
Properties	symbol	Moraine	Rockfill
Saturated weight [kN/m^3]	γ_{sat}	20,9	20,5
Unsaturated weight [kN/m^3]	γ_{unsat}	19,8	16,6
Initial void ratio [-]	$e_{initial}$	0,2	0,6
Young's modulus[kN/m^2]	E	10000	10000
Cohesion [kN/m^2]	c'	0	0
Internal friction angle [°]	φ	35	45
Dilatancy angle [°]	ψ	3	12
Poisson's ratio [-]	ν'_{ur}	0,3	0,3
Soil fragment [%]	<2 µm	6	4
Soil fragment [%]	2 µm - 50 µm	11	4
Soil fragment [%]	>50 µm	83	92
Permeability [m/day]	$K_x = K_y$	1.38*10^3	8.64

Table 4.6: Soil characteristics used in numerical model for Moraine soil and rockfill Glen Shira lower dam

The pore pressure sensors consist of five porous stone piezometer disks, previously calibrated against mercury columns. It is stated in by Paton and Semple (1961) that errors are 'of minor order and can be neglected' No significant pore water pressures were recorded during construction. Positive pore pressures were measured only after reservoir filling. On one hand side the dike is dry and on the other side a lake with changing water level is present. Before increasing the water level, it is constant long enough to create hydrostatic water conditions throughout the dike towards the concrete core wall. Afterwards the water level is slowly increased during 5 days and then lowered with 4 steps. Afterwards the water level is increased again. The water level

fluctuations are visualised in figure 4.27 to 4.32.

4.4.1. Numerical estimation of field test

Similar to previous verification's a coupled analysis is used in PLAXIS2D, combined with a Mohr-coulomb model. The unsaturated soil parameters are taken from the Hypres data set, described in the previous section 4.3. The shape of the dike is similar to the one in figure 4.26, except only the part left of the concrete wall is modeled. This can be done under the assumption that the concrete wall is impermeable and undeformable. The cross section can be seen in figure 4.26. The pore pressures at the place of the five piezometer disks are estimated with the numerical model shown in figure 4.26. The pore pressures calculated in PLAXIS are added with the height of the point above reference height times 10, with the reference height being the base of the undeformable and impermeable rock layer. In this way it can be compared with the piezometer disks from the field test which show a water pressure in meters above reference level. During the numerical test the water level is altered just as in the field model according to figure 4.27.

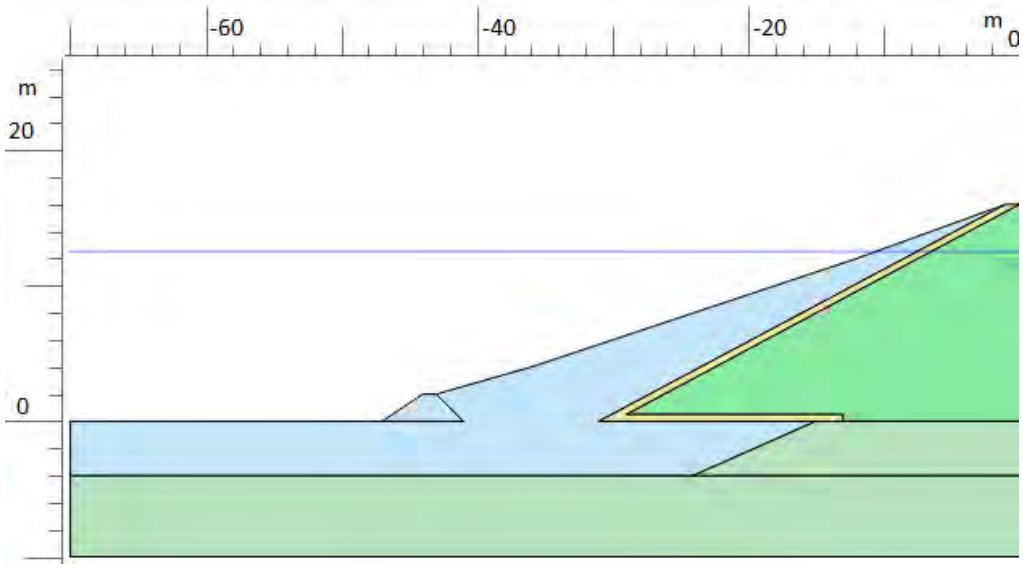

Figure 4.27: Numerical model of Glen Shira lower dam

The numerical solutions of the pore pressure estimation are visualised with the field measurements. Firstly the Young's modulus of the morainic fill is taken as 10MPa, as described in the paper. This first numerical estimation gives a good estimation of the pore pressures, especially for points 1 2 and 4, which are further from the centre of the dam.
The points 3 and 5 are close to the core of the dam. Therefore they have a slower response to the water level changes. The numerical results of these points are less related with the field measurements as well. This divergence could be due to inhomogeneous soil properties in the morainic soil, other wrongly estimated soil characteristics or measurement errors. These mistakes could cause a larger error in pore pressure response in point 3 and 5 than the ones close to the side of the dam.

An increased stiffness could cause a slower pore pressure response in a coupled model because the soil takes up more of the load initially (Alonso Pérez de Agreda and Pinyol Puigmartí, 2009). To show this effect the results of the numerical model with a Young's modulus of 20MPa was added. It does give a slightly slower pore pressure response and an improved estimation of pore pressures. However, it does not give satisfying results as well and to double the Young's modulus is not realistic either.

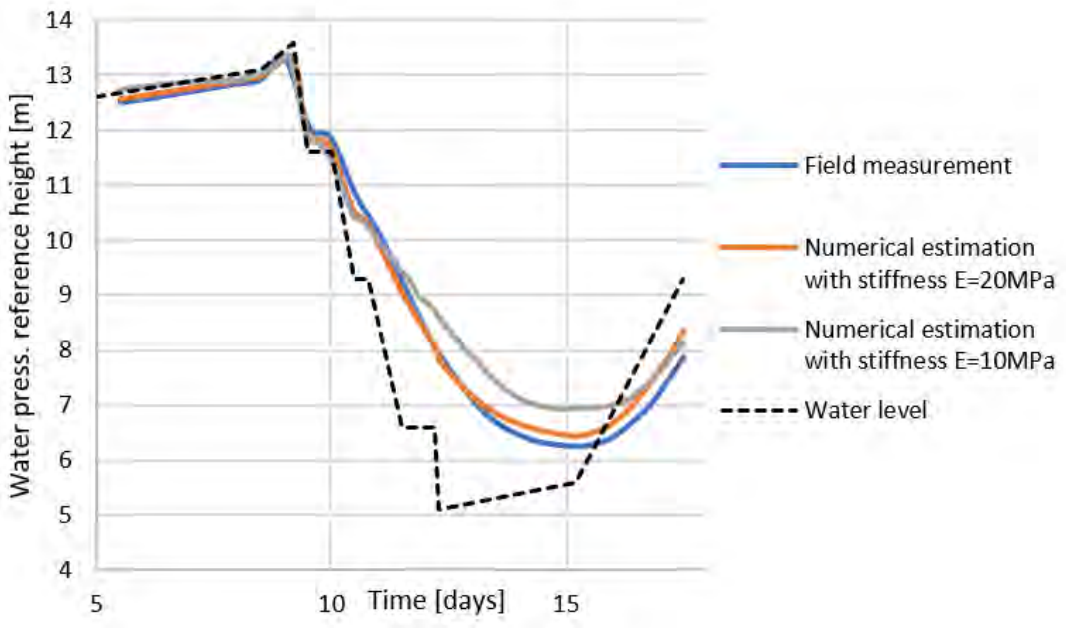

Figure 4.28: Pore Pressure point 1

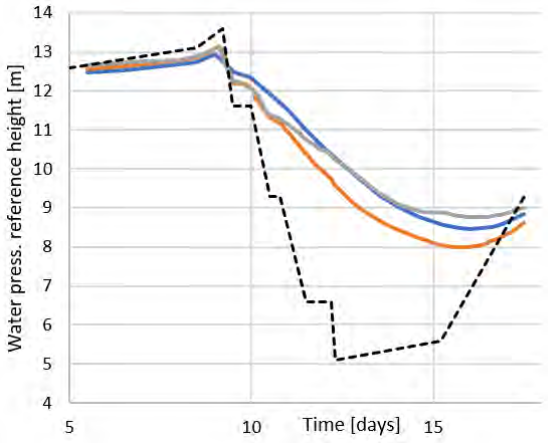

Figure 4.29: Pore Pressure point 2

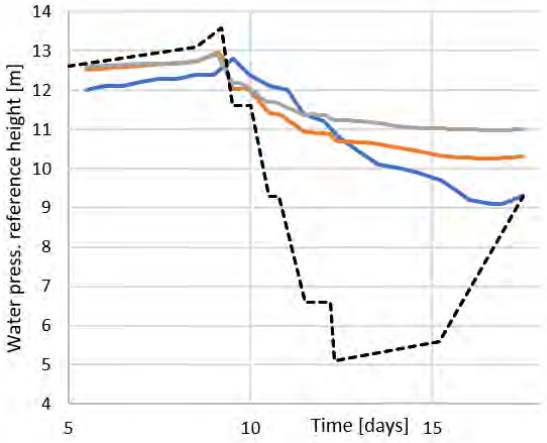

Figure 4.30: Pore Pressure point 3

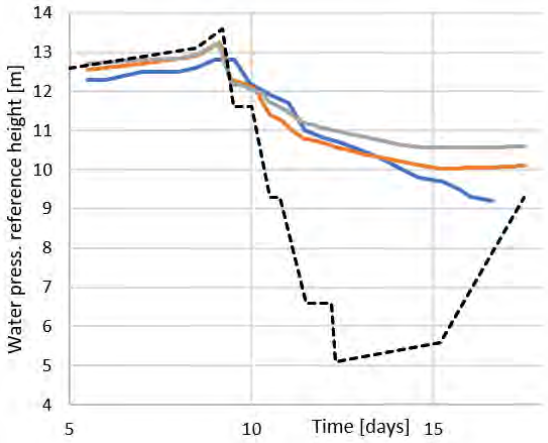

Figure 4.31: Pore Pressure point 4

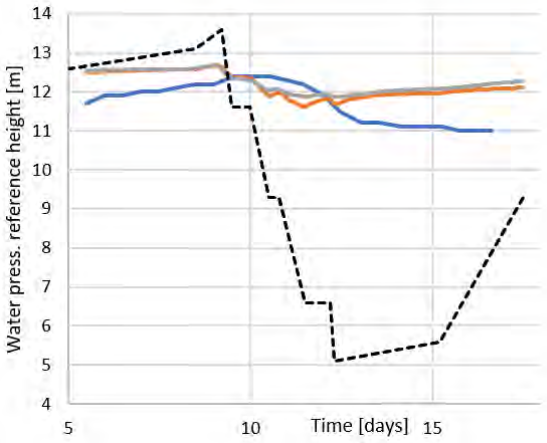

Figure 4.32: Pore Pressure point 5

5

Physical modelling

This chapter describes a centrifuge test from which the results are analysed with the numerical model of PLAXIS. The centrifuge test is performed with the purpose of tracking the movement of the grains at failure. The numerical model has been compared on several components as pore pressure, saturation and FoS with tests from literature. However, tracking displacement will give a better understanding in the failure development during rapid draw down and in the correctness of estimating displacement by PLAXIS.

5.1. Specification of the TU Delft Centrifuge

The centrifuge test is performed at the TU Delft geotechnical centrifuge, which is located at faculty of Civil Engineering and Geo-sciences. This device has a diameter of 2440 millimeters and has the functional capacity of being tested at 300 times the gravitational acceleration (Alderlieste et al., 2011). A schematic view of this centrifuge is illustrated in Figure 5.1.

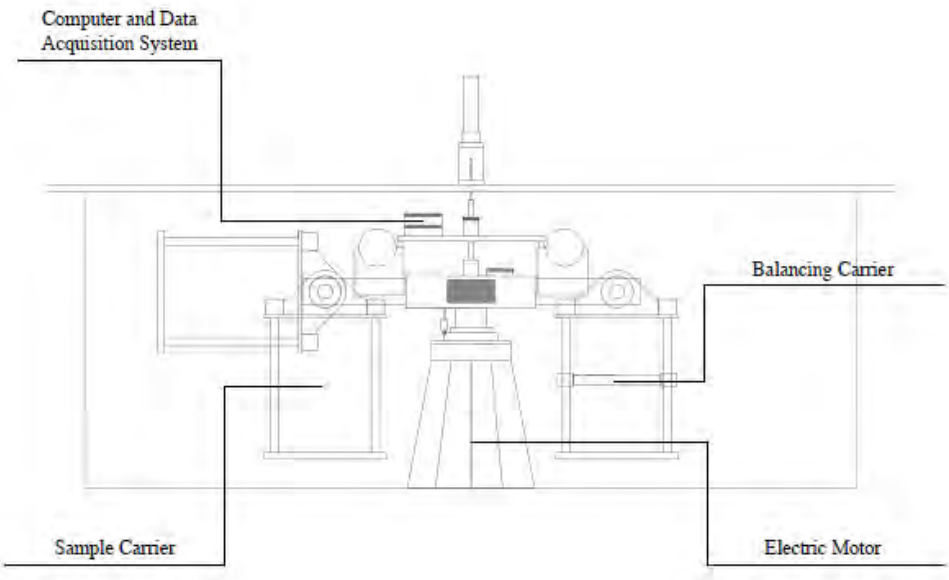

Figure 5.1: Cross section of the geotechnical centrifuge (Alderlieste et al., 2011) adapted by (**?**)

A computer and data acquisition system is mounted on the mainframe of the centrifuge. With this system the actuator of the centrifuge can be controlled using which, lateral and vertical displacements can be controlled (Alderlieste et al., 2011). The specifications of this centrifuge are summarized in table 5.1.

Table 5.1: Specifications of the TU Delft Centrifuge

Element	Quantity	Unit
Maximum Sample Size	300 x 400 x 450	mm^3
Centrifuge Arm Radius	1220	mm
Maximum Design Acceleration	300g	m/s^2
Maximum Design Payload at 300g	40	kg
Carrier Dimension	500 x 240 x 380	mm^3

5.2. Material properties

A very fine, uniform silica sand is used in the experiments of this study, called Geba-sand (Krapfenbauer, 2016). This material is often used in lab tests, especially at the geotechnical laboratory of the Technical University of Delft, therefore many soil characteristics can be found in literature.
Krapfenbauer (2016) documented many of the relevant properties of the Geba sand. The adopted averages of the soil characteristics are shown in table 5.2. The shown peak friction angle is found with the help of a direct shear test at at vertical effective stress of 54.19kPa and with a relative density of 0.96% of the sand. All results of this direct shear test are shown in figure F.1 and F.2 in appendix chapter F.

Gs	Cc	e_{min}	e_{max}	γ_{min}	γ_{max}	ϕ_{cv}	ϕ_{peak}
[-]	[-]	[-]	[-]	[kN/m3]	[kN/m3]	[°]	[°]
2.67	1	0.64	1.07	12.9	16.3	34	44

Table 5.2: geba sand properties according to Krapfenbauer (2016)

The lateral earth pressure coefficient at rest K_0 was estimated by an empirical approach as proposed by Jaky (1944). Within this formulation the internal friction angle was used to come to an estimation. This resulted in K_0 being equal to 0.44 based on the residual friction angle. Jaky's formula is shown below:

$$K_0 = 1 - sin(\phi) \tag{5.1}$$

Krapfenbauer (2016) performed permeability tests and several sieve tests to find the grain size distribution curve of the Geba sand. Hereby several samples were taken from a laboratorial sample. Additionally a further sample was the Geba sand straight from the producer (Bs, 'bagsand'). Afterwards the extracted sand was dried in an oven at 105 degrees for a minimum of 24 hour to evaporate all water. The results of the sieving tests for six different samples are shown in figure 5.2.

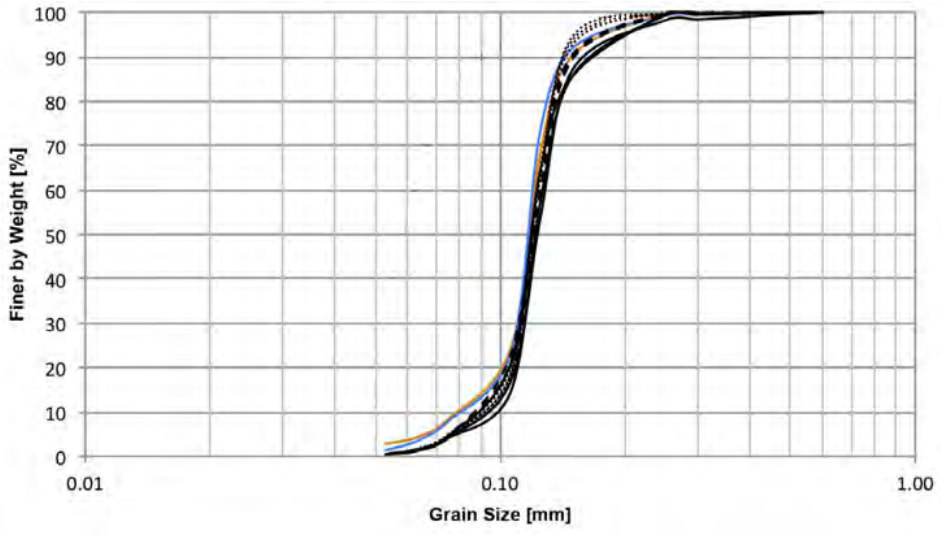

Figure 5.2: Grain size distribution of six different samples of Geba sand from (Krapfenbauer, 2016)

The hydraulic conductivity was taken from a test performed by Gregor Portman of the Hochschule Luzern. He performed a falling head test with geba sand with a void ratio of 0.805 and found a hydraulic conductivity of $1.8x10^{-5} m/s$.

5.2.1. Stiffness parameters

A previous study of Chavez Abril (2017) went further into describing the geba sand. Using the data collected by Krapfenbauer (2016) soil stiffness parameters for the use of the Hs model were added, such as the oedometer stiffness between 50-100kpa pressure. The reference pressure is taken as the standard 100kPa. The oedometer stiffness at this pressure is 15000kPa.

According to Chavez Abril (2017), Geba sand showed a rough correlation that approximates the unloading-reloading stiffness by multiplying the Oedometer stiffness E_{oed} by a factor that was found to be between around $[4 \div 7]$. From previous studies performed by Schanz and Vermeer (1998), it was stated that for sands a rough correlation of $E_{ur} \approx [4 \div 5] xEoed$ may be used. By relating this correlation with the obtained results, a relation of $E_{ur} = 4xEoed$ was adopted for this research project.

Geba sand shows a relatively flexible response compared to medium-loose sands (Chavez Abril, 2017). An expression $E_{oed} \approx [1 \div 1.5] xE50$ may be applied from normally consolidated sands (Schanz and Vermeer, 1998). Here $E_{oed} = 1xE50$ was used, because Chavez Abril (2017) found satisfying results with it.

5.2.2. Soil water retention curve

As described in the chapter 3.1, for the estimation of unsaturated flow and suction the SWRC is needed. Chapter 4.3 showed that the estimation of the unsaturated soil behaviour of a sand by placing the soil in a soil class, is not sufficiently accurate and that the Modified Kovacs method can lead to more accurate results. The estimated SWRC by the Modified Kovacs with hysteresis is shown in figure 5.3. It should be noted though that hysteresis in the SWRC is not an available input in PLAXIS as described in chapter 3.1. The drying curve was adopted as input as drying is more influential than wetting in rapid draw down conditions.

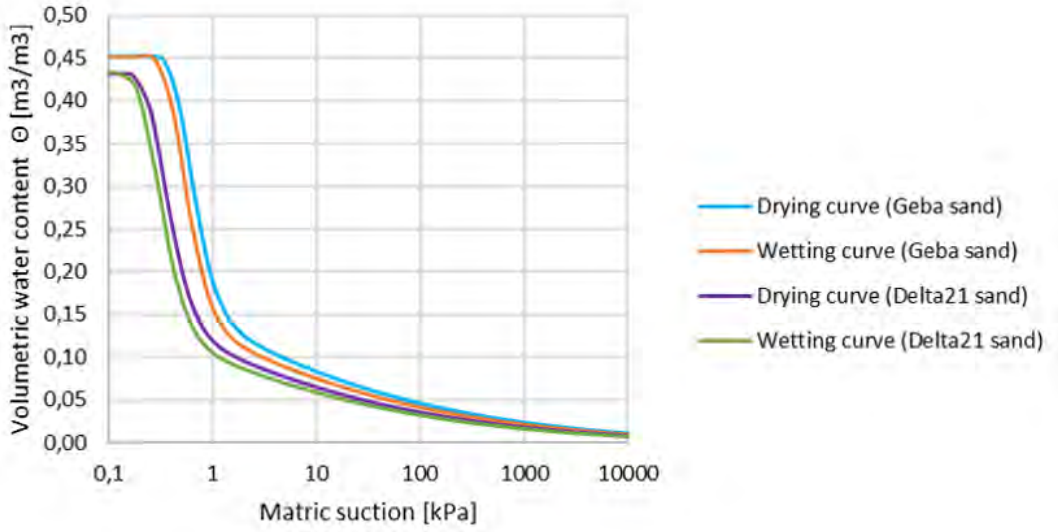

Figure 5.3: Soil water retention curve of Geba sand and sand of the Delta21 dike

Figure 5.3 show the unsaturated soil behaviour of both the Geba sand and the sand for the dike of the Delta21 project. The Geba sand has a higher saturation level at the same level of matric suction. This is as expected as the Geba sand is a finer sand. PLAXIS multiplies the effective saturation with the matric suction as part of the calculation to find the suction. This would result in a higher suction for the Geba sand than the sand in the Delta21 dike.

5.2.3. Relative hydraulic conductivity relationship

The relative hydraulic conductivity function is shown in figure 5.4 for both the Geba sand as the sand of the Delta21 project calculated according to the method of Burdine et al. (1953) as described in section 2.4.5. It can be noted that the Geba sand has a higher K_r at the same pressure head. This is because the method of Burdine et al. (1953) is based on saturation as an input parameter and the Geba sand has a higher saturation at the same pressure head

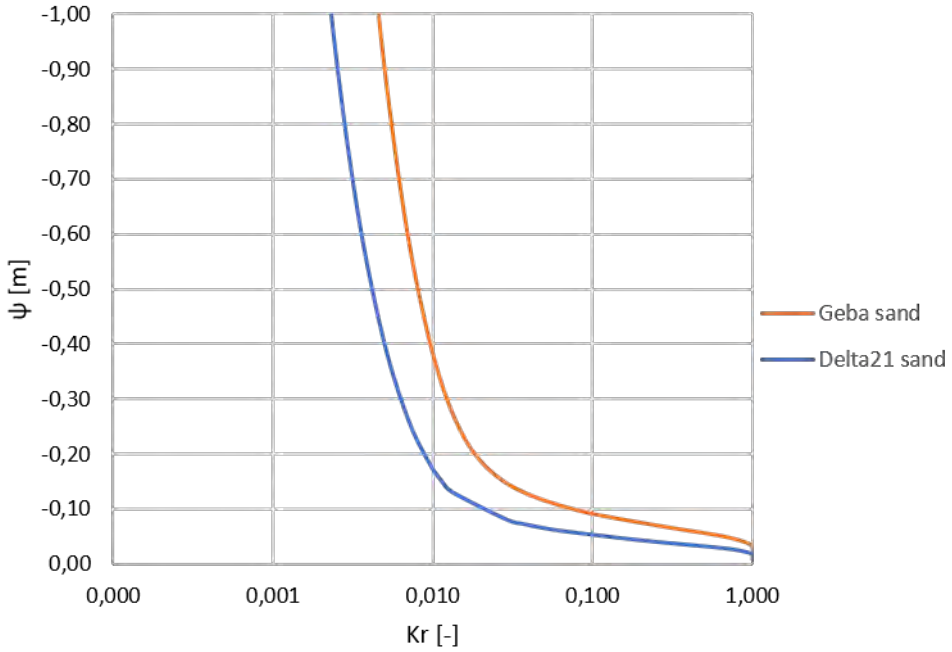

Figure 5.4: Relative hydraulic conductivity function with method of Burdine et al. (1953)

5.2.4. Modulus reduction curve

To find the modulus reduction curve the same method was applied as in section 2.4.6, where the modulus reduction curve of the sand for the delta21 dike was found. figure 5.5 them for both sands. The Geba sand has a higher G/G_{max} for the same amount of strain. This results in a more elastic behaviour.

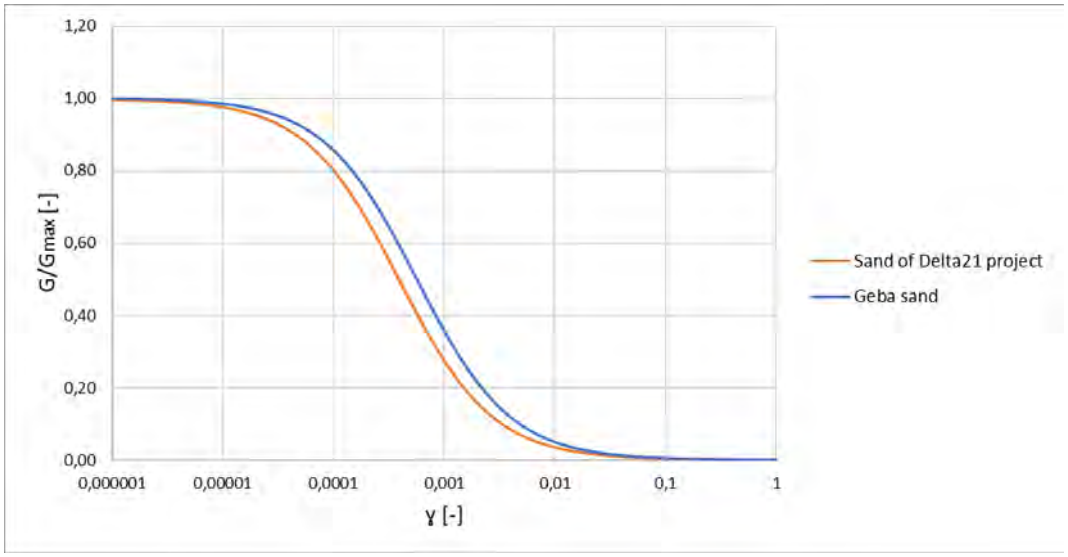

Figure 5.5: Modulus reduction curve

5.2.5. Summery geotechnical properties

A summary of the geotechnical properties of the Geba sand are captured in table 5.3. Sand Layer 3 of the Delta21 dike is added as well. This is the layer below the water level described in section 2.3.
Both sands have an almost similar relative density and strength parameters. However, the sand of the Delta21 project is among other things stiffer and has a higher hydraulic conductivity.

Geotechnical properties		Geba Sand	Sand layer 3 of Delta21 dike
-Relative density [-]	γ_{sat}	0.65	0.64
-Porosity [-]	γ_{sat}	0.43	0.39
-Saturated weight [kN/m^3]	γ_{sat}	19.4	20.1
-Unsaturated weight [kN/m^3]	γ_{unsat}	15.1	16.2
-Particle size at which 10% of the soil particles by weight are finer [mm]	$d10$	0.086	0.095
-Particle size at which 60% of the soil particles by weight are finer [mm]	$d60$	0.111	0.25
-Stress dependent stiffness modulus for primary loading [kN/m^2]	E_{50}^{ref}	15000	37000
-Oedometer stiffness modulus [kN/m^2]	E_{oed}^{ref}	15000	35000
-Stress dependent stiffness modulus for re- and unloading [kN/m^2]	E_{ur}^{ref}	60000	147000
-Cohesion [kN/m^2]	c'_{ref}	0	0
-Critical state friction angle[°]	φ	34	33
-Dilatancy angle [°]	ψ	4	3
-Youngs modulus [-]	v	0.2	0.2
-Reference pressure [kN/m^2]	P_{ref}	100	100
-Coefficient of lateral earth pressure [-]	k_0	0.44	0.46
-Permeability [m/day]	$K_x = K_y$	3.63	5.49

Table 5.3: Geotechnical parameters Geba sand and sand layer 3 of Delta21 dike

5.2.6. Other materials used

Next to the geba sand a fine gravel is used as a high permeable drain at the toe of the dike. It has a high internal friction angle of 38°and the grains of this sand are 2-4mm in diameter. This gives an estimated hydraulic conductivity of 30m/day (Oosterbaan and Nijland, 1994). Because it is not in the shear band of the expected failure and therefore of lesser importance, it is assumed that all other soil properties are similar to the Geba sand.

5.3. Test setup and monitoring

The samples were build within a strongbox which was placed in the centrifuge. The goal of the strongbox is to accommodate the prototype while simulating changing water levels and providing support for measurement equipment. In this way rapid draw down conditions in a dike can be simulated, while changing shape, water level and pressures are monitored.

the strongbox consists of seven separate containers and has a length, height and width of respectively 615, 405 and 220mm. Chamber 3, shown in figure 5.6, will be housing the prototype. It's size is 450 x 200 x 90 mm and is therefore the largest chamber in the strong box. It is air-tight, to prevent turbulent air streams influencing the test.
The upper water container acts as a water reservoir during the test, which contains a maximum of 1.62 liter when filled to the edge. From this upper water container water can flow through valve 1 down into the second chamber, within the water head is controlled. From chamber 2 the water can flow through group valves 3 to enter chamber 3, or through valve 2 to a water reservoir at the back of the strongbox. This chamber 7 acts as a reservoir to store the water.

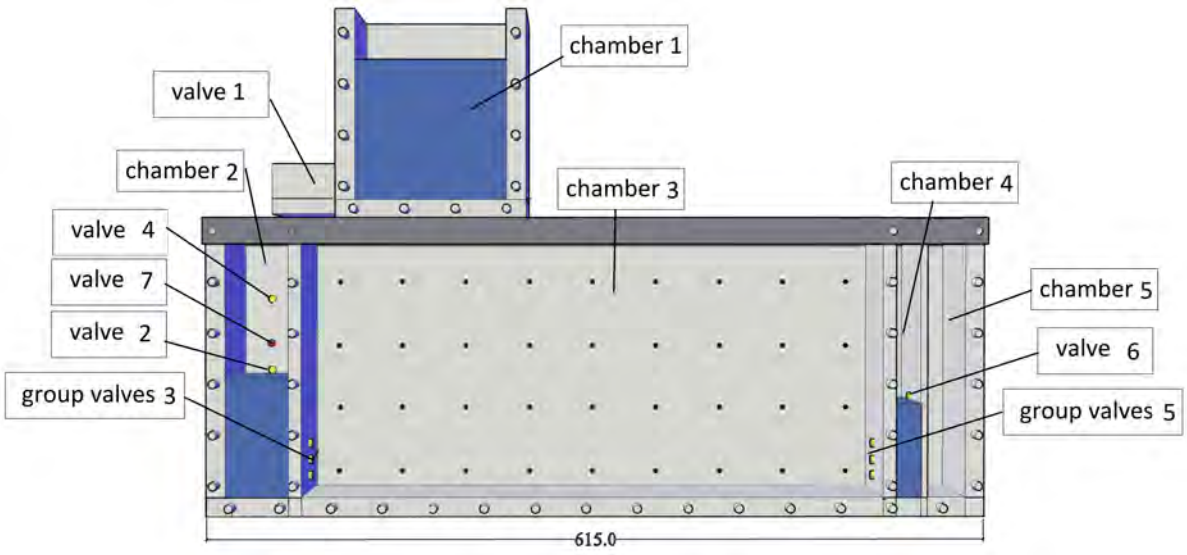

Figure 5.6: front view of the strongbox

In chamber 3 or main chamber the sample was build. The shape of the prototype can be seen in figure 5.7. Granular material was placed at the sides next to the inflow and outflow valves. This layer has a high hydraulic conductivity so water can flow out faster. Simultaneously the layer prevents erosion during inflow by creating a more homogeneous distribution and reduction of kinetic energy. The coarse sand is placed at the toe of the dike as well. The higher hydraulic conductivity and internal friction angle reduce possible erosion at the toe of the dike by the outflow of water.

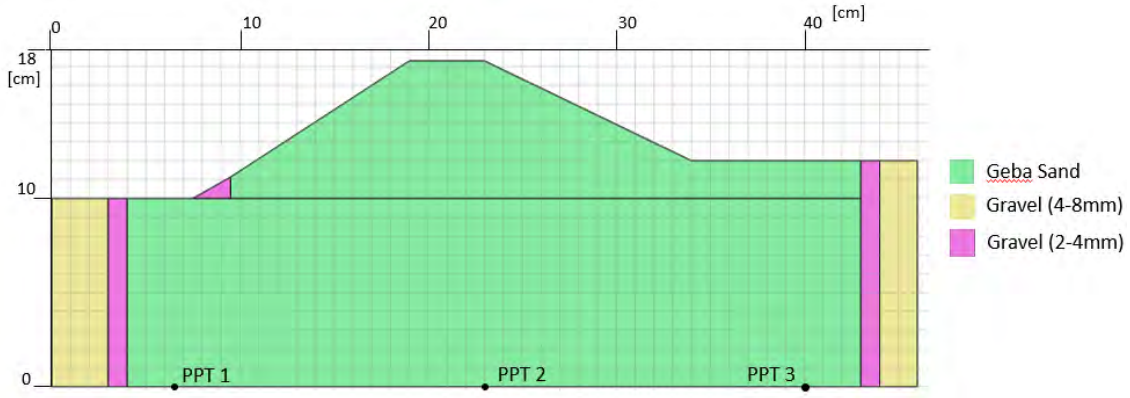

Figure 5.7: cross section of the sample

5.3.1. Centrifuge monitoring

The sample was monitored in three ways; water pressure sensors allow to measure the change in pore pressure, Particle Image Velocimetry (PIV) will be used to measure the soil deformation, and last of all an extra camera was placed to give a general overview of the situation.

In the geotechnical lab seven water pressure sensors were present and ready to be used. In all of water reservoirs, chamber 1, 2, 4 and 5, a sensor was placed. In this way it can be checked if the valves work correctly and no water has been leaked from the setup. The other three sensors were placed in the prototype. The PPT's are placed on the floor of the strongbox, resulting in a minimum influence on stability.

PIV is the deformation measurement which uses digital photography to capture images of planar soil deformation (White et al., 2003). Target markers are installed on the strong box so resulting displacement vectors can be made. These vectors are made by tracking the textural patches within a predefined search zone from

one image to the subsequent one, and this procedure is followed for a series of images. The movement of each patch is represented by a vector on the original image, based on this tracking (Askarinejad, 2015). The vectors give among other things insight in the failure envelop of the dike.

5.4. Sample preparation

Before the sample is build, 1% of the geba sand is colored with black ink. An earlier performed test without coloured grains showed that the camera used for the PIV analysis could not track individual grains due to the low divergence between the grains. To color the sand 10ml of Indian black ink is mixed with 100g of sand. The ink is water resistant and opaque. The bottle can be seen in figure 5.9. After the ink and sand is mixed the sand is dried in the oven for 18hours on 101°Celsius. Then it is mixed with the white geba sand and water by weight proportion of 10%. Afterwards it was stored for one day in a sealed plastic bag. This ensures a uniformly distributed water content all over the sample. The black ink proved to be adhesive and water resistant.

Figure 5.8: black geba sand

Figure 5.9: black ink used to color geba sand

Preparation of the model box

The inside of the model box or chamber 3 was coated with vaseline to decrease the friction between the model and the box, which could potentially negatively influence the test. The chamber was filled with a layer of water and was constructed below water. A previous attempt constructed in dry conditions was disturbed when water was later added, which resulted in a loss of stiffness of the top layer of sand. This can be seen in the difference between figure 5.10 and 5.11. Both these figures show the top view of the left hand side of the prototype, one before and one after the water level increase.

Figure 5.10: topview left side strongbox before remodelling toe and increasing water level

Figure 5.11: topview left side strongbox after remodelling toe and increasing water level

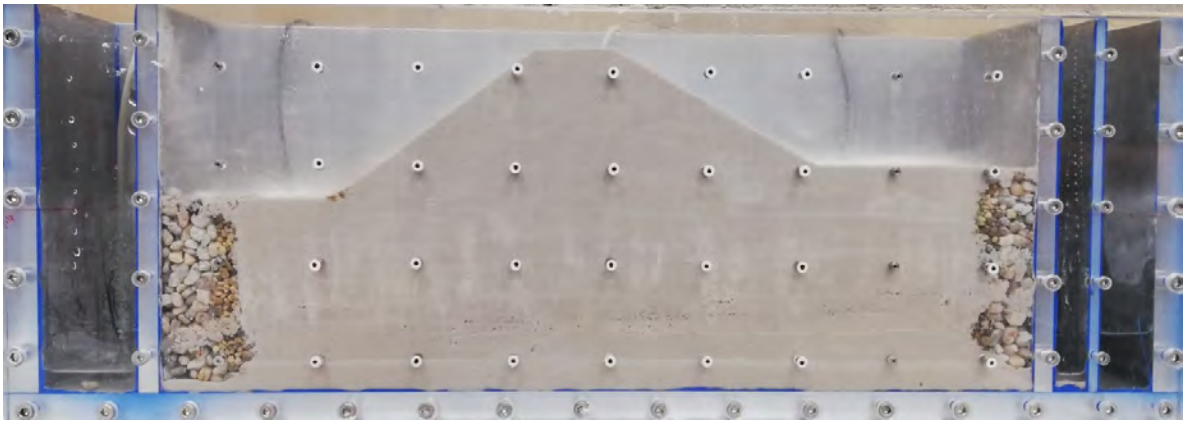

Figure 5.12: front view of dry prototype

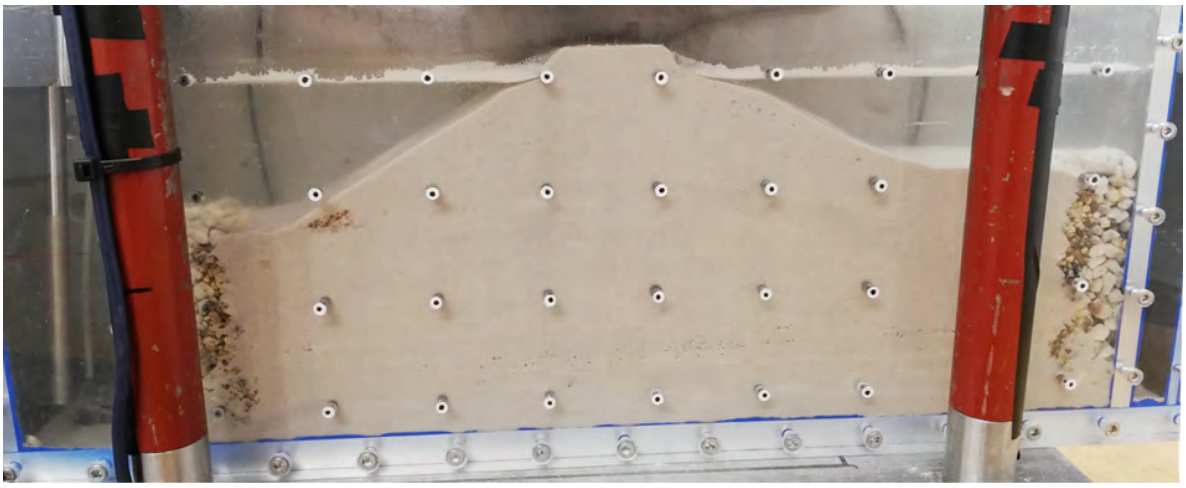

Figure 5.13: front view of prototype after water level increase

The sealed plastic backs where the geba sand were stored in, contain the amount of sand to fill the entire model box with a layer of 2cm in height, based upon an expected void ratio of 0.81. After half the bag was emptied it was compacted. By measuring the height of each layer it can be insured that the correct effective stress state is reached.
Every two layers the geba sand at the sides at the place of the drainage layer was removed with a spatula and replaced with material of the drainage layer. On the left hand side of the prototype, this drainage layer consists of a 3cm wide column of 4-8mm gravel and 1cm wide column of 2-4mm gravel, to give a total of 4cm wide column. On the right hand side the drainage layer was made up from 2cm of the coarse gravel and 1cm of the finer gravel. This was repeated until the entire model box is filled. During the process of building the sample the geba sand filled the voids in the filter layer partly, which can be seen in figure 5.14.

Once the whole box was filled it was placed in the geotechnical centrifuge and spun for 2 minutes at a gravitational acceleration of 100g. This procedure makes sure that all voids are filled with water. Afterwards the void ratio was measured at both sides of the strongbox. A metal ring was pushed in the sample and removed again with a spatula. Extra sand was removed and the full ring was weighed. By knowing the volume and weight of the sand in the ring the void ratio can be calculated. The resulting void ratio left and right was respectively 0.765 and 0.775.
To visualize the right shape the model a drawing of the dam section was placed on the model box. Than excess soil was removed with a spatula. For precision a metal plate in the shape of the dam was scraped back and forth over the model, so all excess sand was removed. Because to much of the coarse sand of the toe was removed, some was added again. Afterwards water was slowly added by pouring it in from above on the filter layer to a height of 16.7cm.

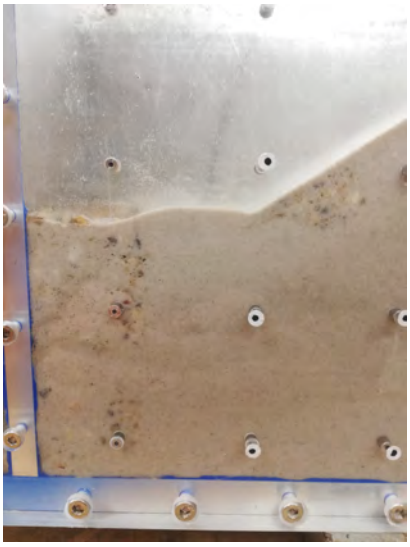

Figure 5.14: filter layer filled with geba sand

5.5. Testing program

The testing programm consisted of two separate runs in the centrifuge. In the first run the sample had a constant water table of 16.7cm. The gravitational acceleration was brought to 100g and stayed there for 2 minutes. This had the function to fill all voids with water and consolidate the sample. After this run the centrifuge was slowed down and water was added to bring the water level up to the original level. Then the centrifuge was brought again to the same rotational speed achieving a gravitational acceleration of 100g. After two minutes at this rotational speed the water level was lowered on the left side of the sample. The water level drops from 16.7cm to 10cm height. The rate of water drop down depends on the filter layer in place and the diameter of the holes in the strongbox. In total two tests were performed; One with a slow drawdown and one with a rapid draw down.

First the test with a slow drawdown was performed. Afterwards the model was reshaped and the filter layer replaced. Because the filter layer was clocked with geba sand in the first test, the second test will experience a faster drawdown.
The desired gravitational acceleration in the sample is 100G, achieved by rotation of the centrifuge. The gravitational acceleration is dependent on the rotational speed and distance to the rotational axis, as shown in equation 5.2

$$a = \omega^2 * r \tag{5.2}$$

The radius from the sample towards the axis of the centrifuge is linearly increasing the rotational acceleration. This radius is not the same for the whole prototype. The top of the prototype is almost 18cm closer towards the centre than the bottom. This would imply that the centrifugal acceleration at the top of the prototype is almost 15% smaller than at the bottom. It was expected that the area just above the toe of the dike is the weakest point, therefore the centrifugal acceleration should there be most closely to the desired acceleration of 100g. This resulted in an rotational speed of 287 RPM.
Not only is there vertical difference in centrifugal acceleration. The same applies in the lateral direction. At the left side this causes an increase in centrifugal acceleration of 1.5%. At the right side this is 2.2%. Not only is the centrifugal acceleration larger at the sides it also has a different direction. The angle differs 11.8°at the bottom right and 9.5°on the bottom left. This direction of the centrifugal acceleration stretches the model.
Figure 5.15 shows the cross section of the prototype with the centrifugal acceleration acting on it. In red the maximum acceleration is shown going as high as 112.6 in the right bottom corner, in the top of the box the acceleration is as low as to 91.7 shown in blue.

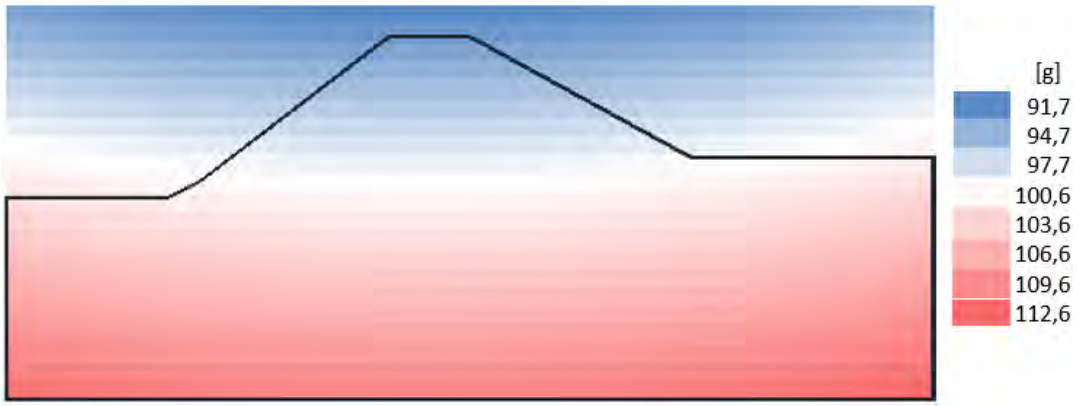

Figure 5.15: Centrifugal acceleration in the model box. In red the maximum acceleration is shown, in blue the minimum

5.6. Results from centrifuge tests

5.6.1. Slow drawdown

The drawdown at the first of the two centrifuge tests is a very slow one as it takes at least 9 minutes in the centrifuge. Figures 5.16 and 5.17 show the results of the pore pressure sensors. The locations of the ppt's are shown in figure 5.7. With a gravitational acceleration of 100g and the scaling law for time N^2, this results in a drawdown of around 60days if performed on large scale. Only the first instant after the valve is open the drawdown is relatively fast compared with the rest of the test. The geba sand, which infiltrated the filter layer, clocks the holes of the mesh decreasing the water flow.

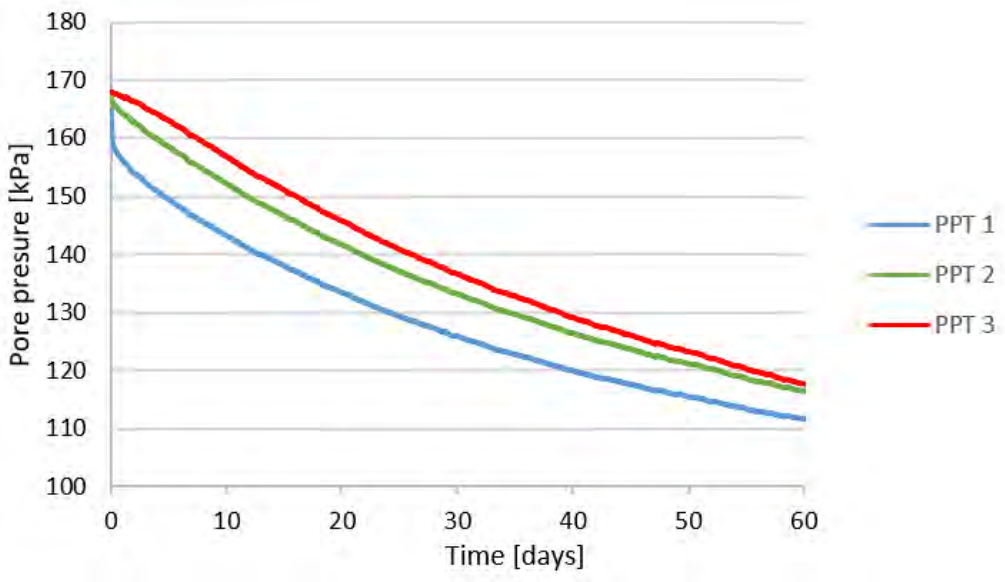

Figure 5.16: Pore pressure of the slow drawdown test

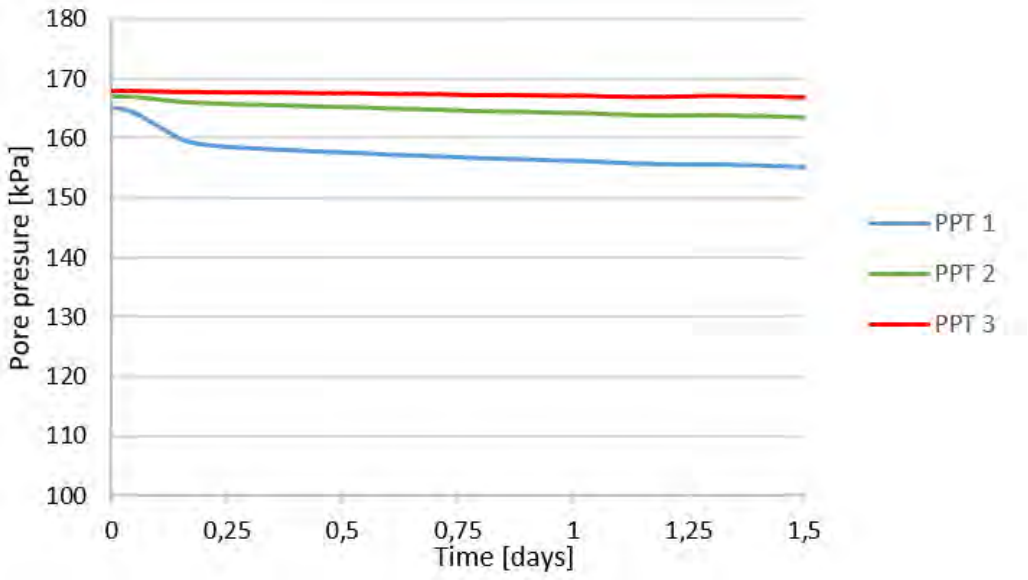

Figure 5.17: Pore pressure during first 1.5 days of the slow drawdown test

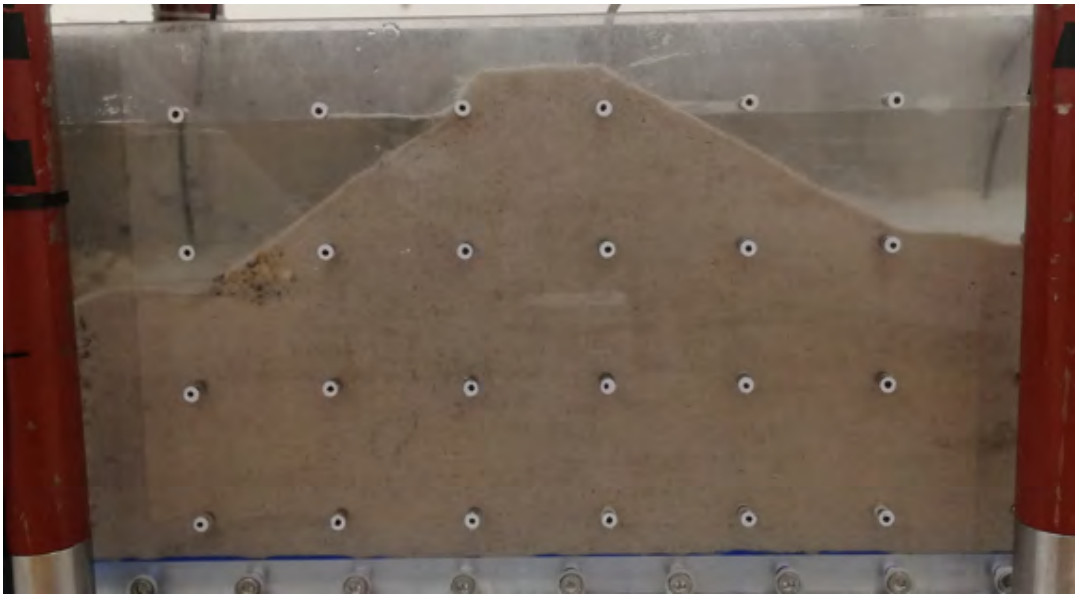

Figure 5.18: Prototype before slow drawdown

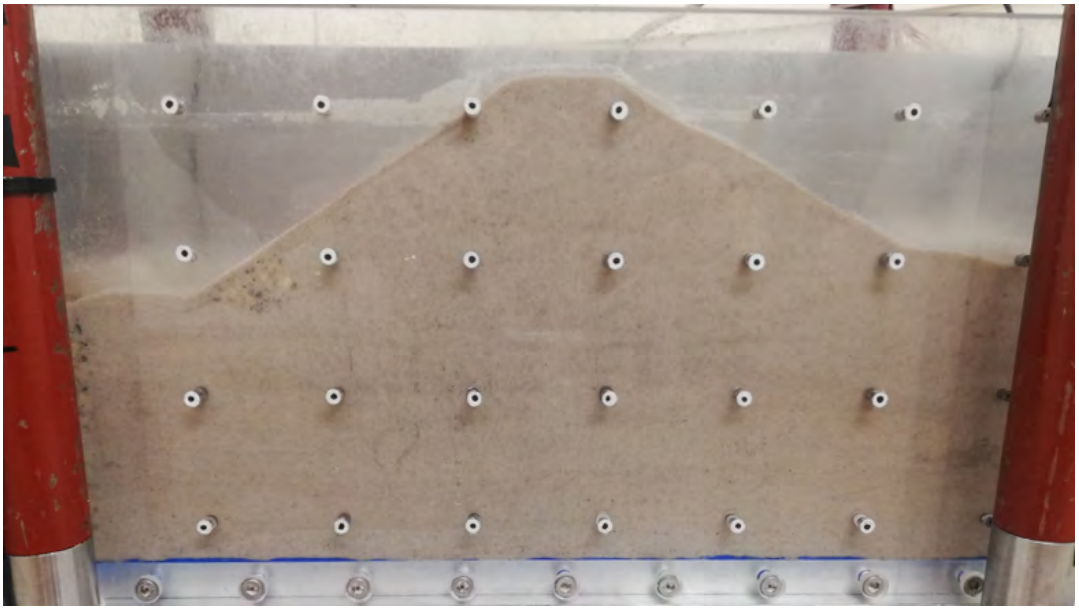

Figure 5.19: Prototype after slow drawdown

figure 5.18 and 5.19 show the prototype respectively before and after drawdown. Only slight changes in the prototype can be seen. The larger grains of the toe of the dike are less visible after the test, because voids became filled with geba sand. Although the prototype was compacted in the first run it seems that it compacted slightly which can best be seen at the dike crest. Here 2mm of vertical movement has occurred. Some of the sand grains stick to the glass, because of the vaseline used to make the surface smoother.
It can be seen that the overall shape of the dike did not change and that the dike was stable during drawdown. A PIV analysis was not possible, because the camera resolution was too low.

5.6.2. Fast drawdown

The drawdown of this test occurs rapidly. The water level at the left hand side of the prototype goes down from 165 to 120 kPa in 6seconds. According to the scaling laws 100g are 0.69days at a normal gravitational acceleration.

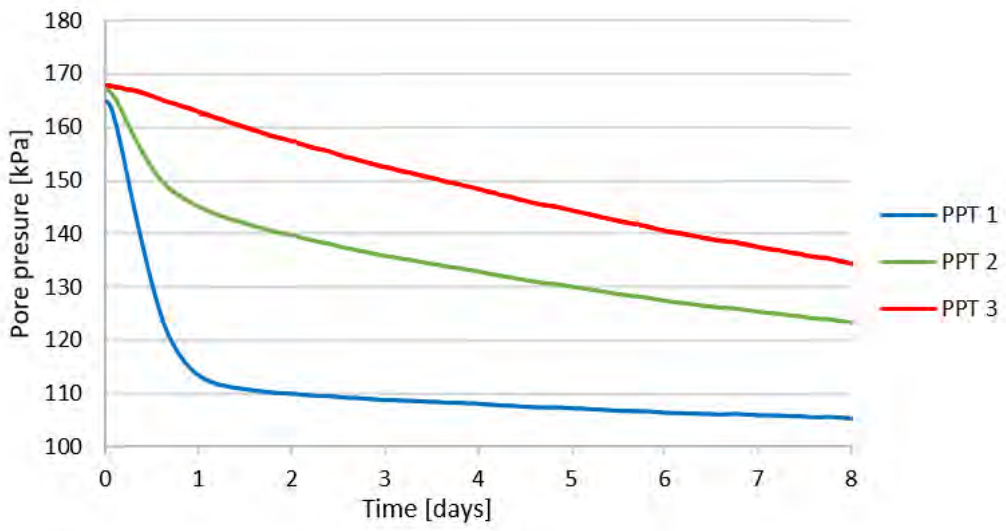

Figure 5.20: Pore pressure development

The PIV analysis shows the deformations from the reference picture towards a selected picture. The reference picture is shown in 5.22. It is taken at the start of the drawdown. The black rectangle on the picture indicate the area of interest for the PIV analysis. The movement inside this area is investigated. Not the whole image is analysed to save computational time.

The water level in the reference image does not seem to be parallel to the bottom of the strongbox. This is because the resultant force in the centrifuge is not parallel to the rotational axis. It can best be seen in figure 5.21. It is estimated that the misalignment of the water level and the bottom of the strongbox is around 1°. The reason for the misalignment is friction in the hinge of the centrifuge arm.

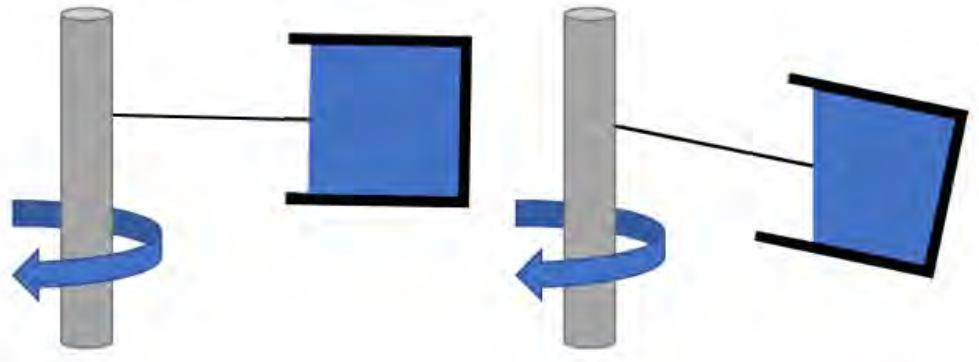

Figure 5.21: Effect of angle of rotational axis

Figures 5.22 to 5.31 show the total deformation from the start of the water level dropdown. The height of the water level is shown with the dashed line and is estimated with help of PPT 1, located at the left hand side of the strongbox.

5.6.3. Deformation during drawdown

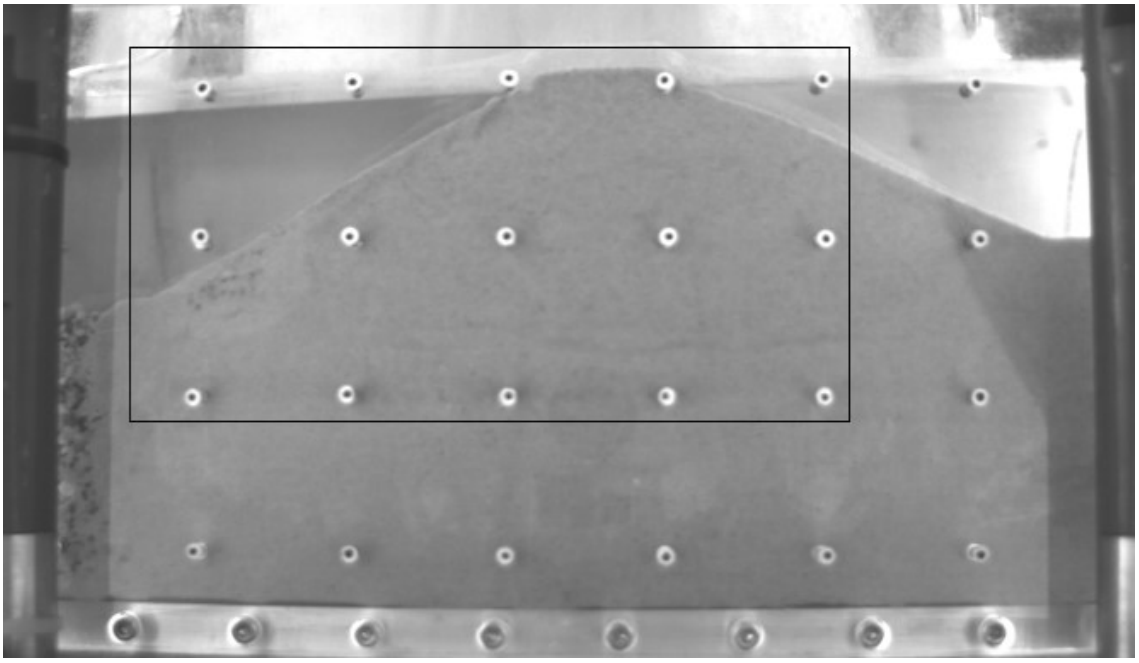

Figure 5.22: Focus area of the PIV analysis

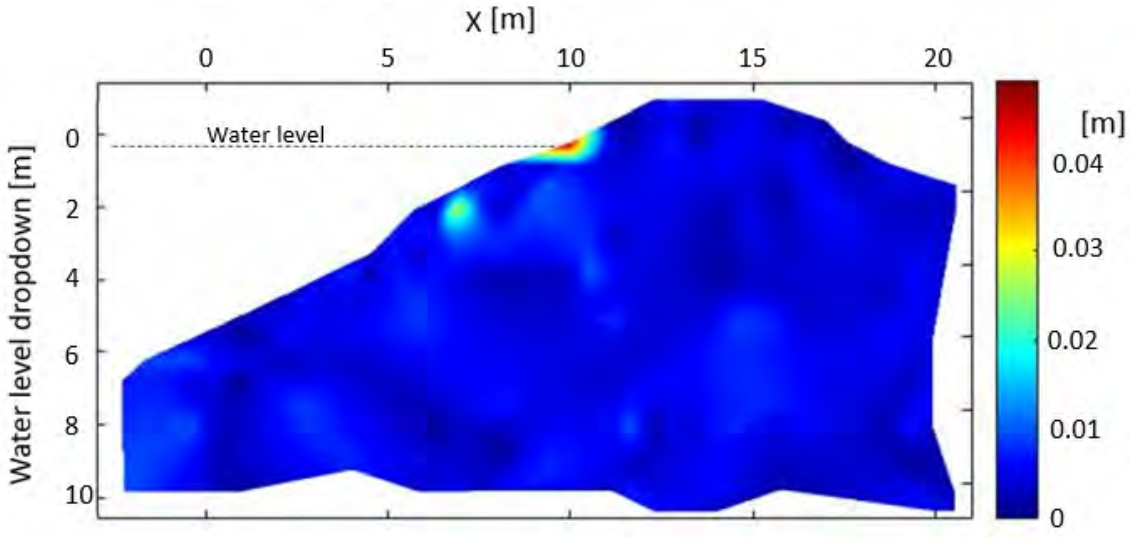

Figure 5.23: Displacement in meter 1.66 hours after rapid drawdown started based on figure G.5 from appendix G

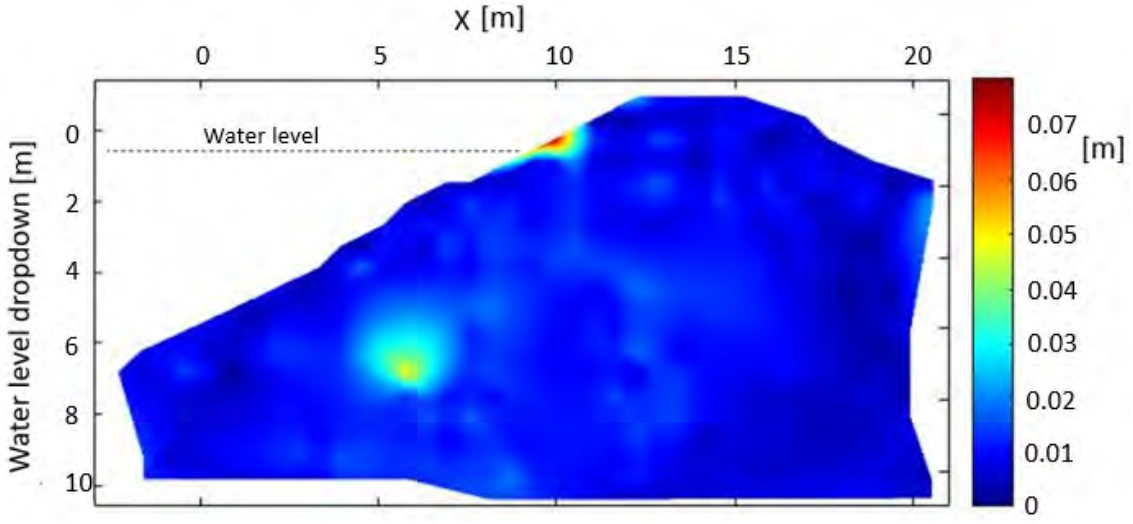

Figure 5.24: Displacement in meter 2.8 hours after rapid drawdown started based on figure G.7 from appendix G

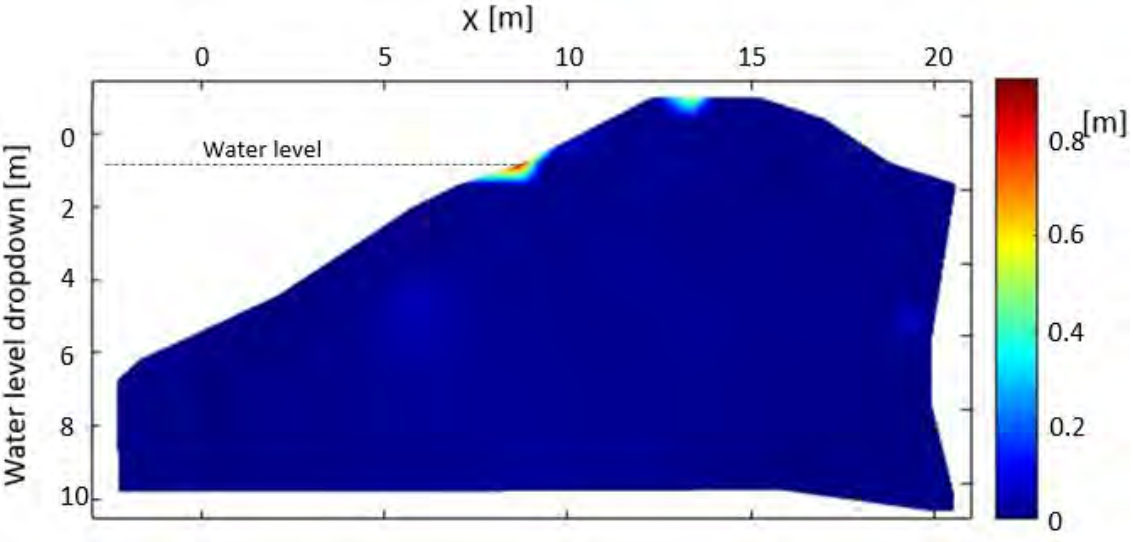

Figure 5.25: Displacement in meter 3.3 hours after rapid drawdown started based on figure G.8 from appendix G

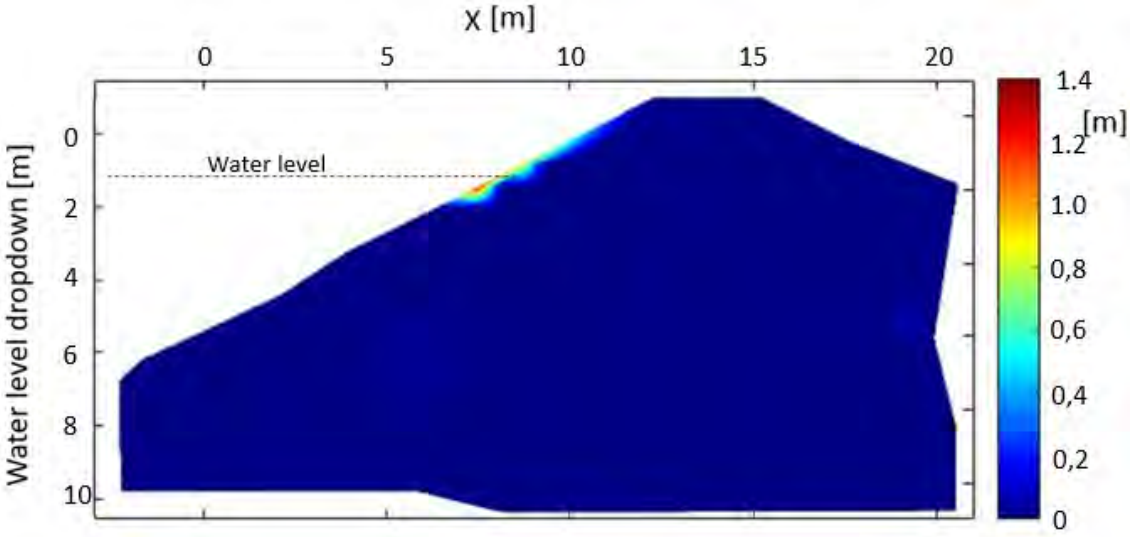

Figure 5.26: Displacement in meter 4.4 hours after rapid drawdown started based on figure G.10 from appendix G

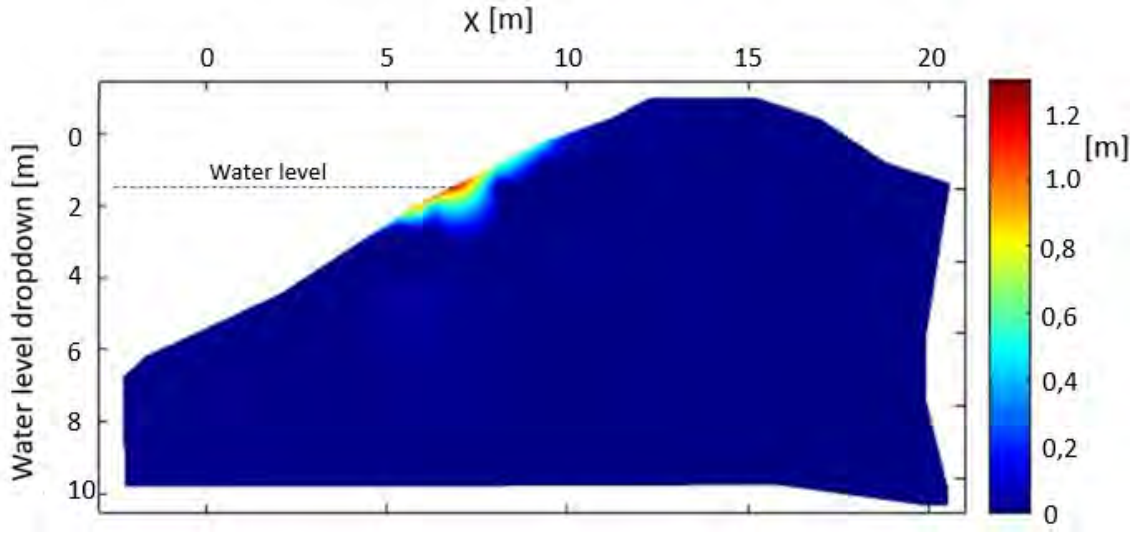

Figure 5.27: Displacement in meter 5.6 hours after rapid drawdown started based on figure G.12 from appendix G

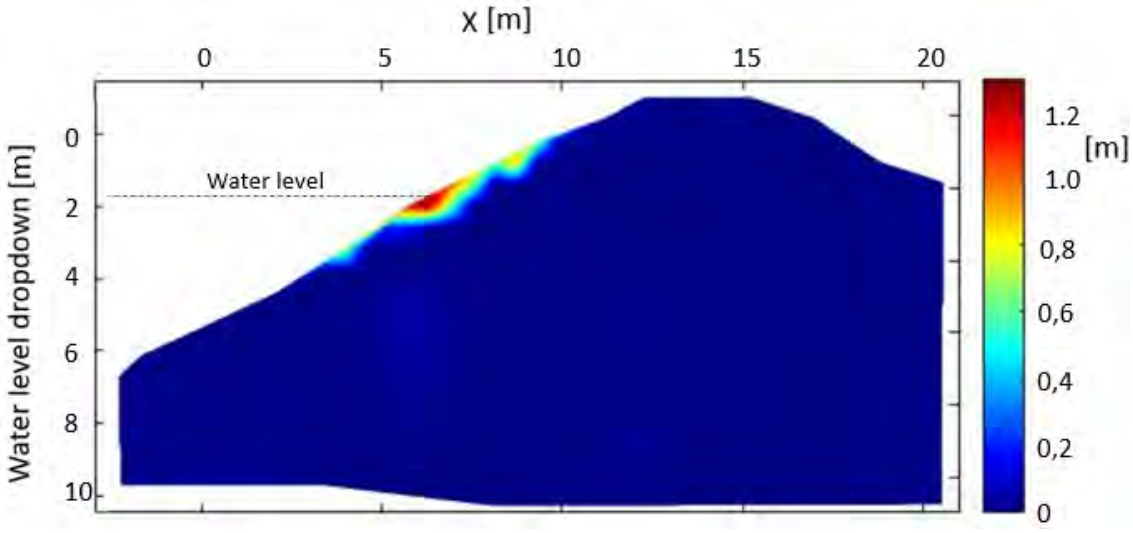

Figure 5.28: Displacement in meter 6.1 hours after rapid drawdown started based on figure G.13 from appendix G

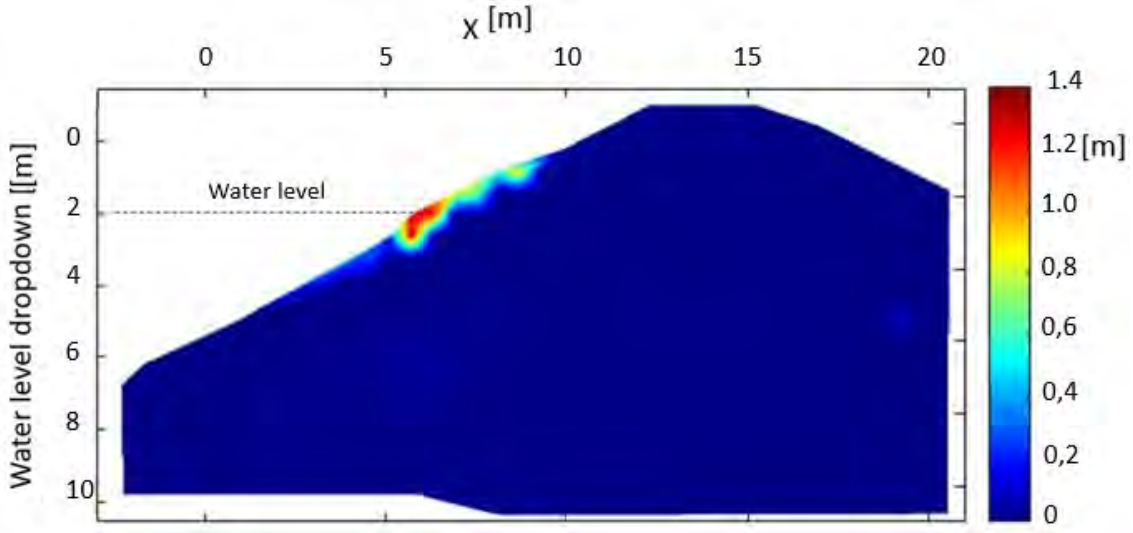

Figure 5.29: Displacement in meter 6.7 hours after rapid drawdown started based on figure G.14 from appendix G

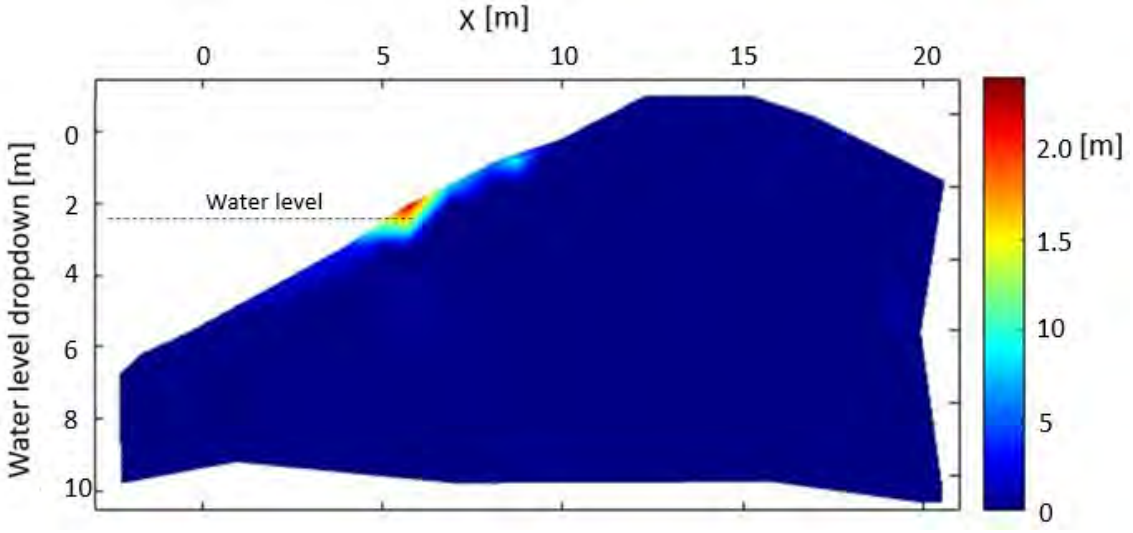

Figure 5.30: Displacement in meter 7.8 hours after rapid drawdown started based on figure G.16 from appendix G

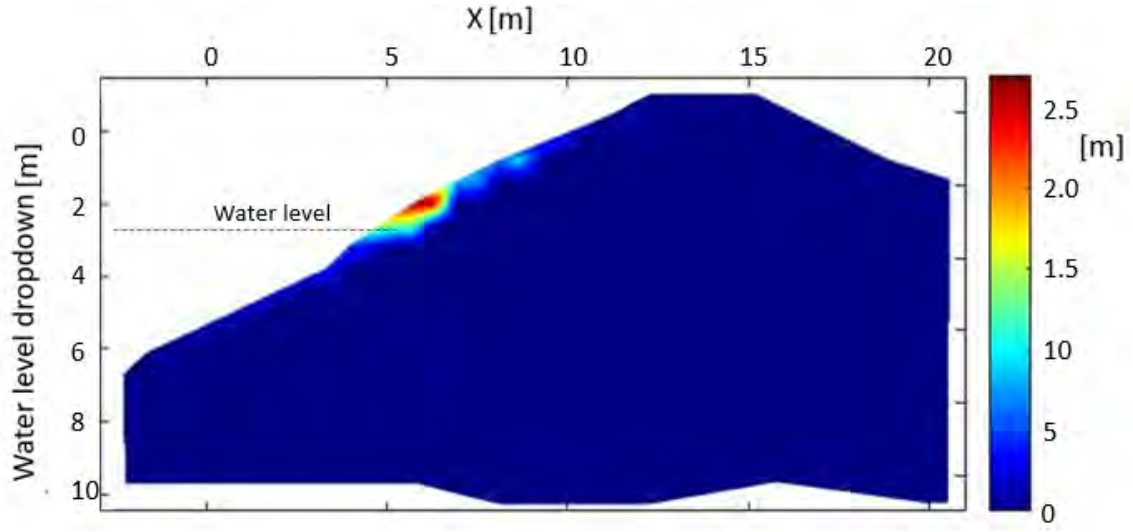

Figure 5.31: Displacement in meter 8.33 hours after rapid drawdown started based on figure G.17 from appendix G

The PIV images show a shallow failure moving down water the decreasing water level. This progressive failure causes large deformations. However, most of the dike is still standing. The same results can be seen in the photo's in chapter G. Although it seems that the area of deformation is slightly larger in the original photo's. The PIV analysis does not capture the very small movements very well.
The amount of deformation rises with the number of figures. However, figure 5.27 has a smaller maximum deformation than an earlier taken figure 5.26. It seems logical that the deformation only becomes larger, this is supported by the photo's taken during the test in G. A high standard error of the PIV analysis is most likely the reason of this unexpectancy. The maker of the software states that a standard error of 0.5 pixels indicates a good calibration. However, in this case the standard error is 2.7pixels, causing vectors to have a potentially wrongly estimated start and end point. This can create over and under estimations of the displacement. This high standard error is most likely been caused by a combination of the very fine material grains, which are hard for the software to differentiate and vibrations caused by spinning the centrifuge.

5.6.4. Comparison with results of numerical simulations

A Plaxis2d model has been made to model the centrifuge test for comparison. This model uses a fully coupled analysis with a hardening soil model as described in chapter 3. The soil parameters used are all stated in section 5.2.

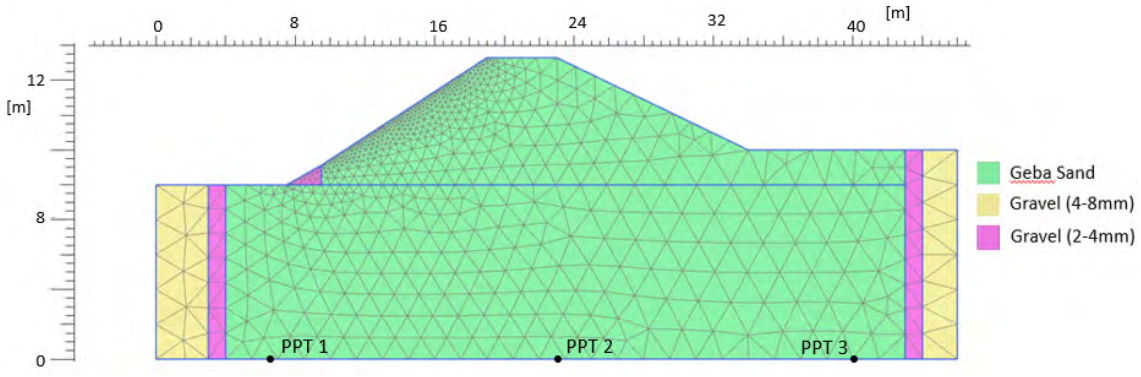

Figure 5.32: Mesh of numerical estimation of centrifuge test

Rapid draw down

The water level starts at 16.7cm and drops rapidly down within the first 8 seconds. The water level dropdown used as input for the numerical model is taken by measuring the height of the water level of the photo's taken during the centrifuge test. Here the height is taken where the water level touches the left hand side of the dike. This water level is visualised in figure G.42 of the appendix. The results of pore pressure sensors of the numerical model are shown in figure 5.33.

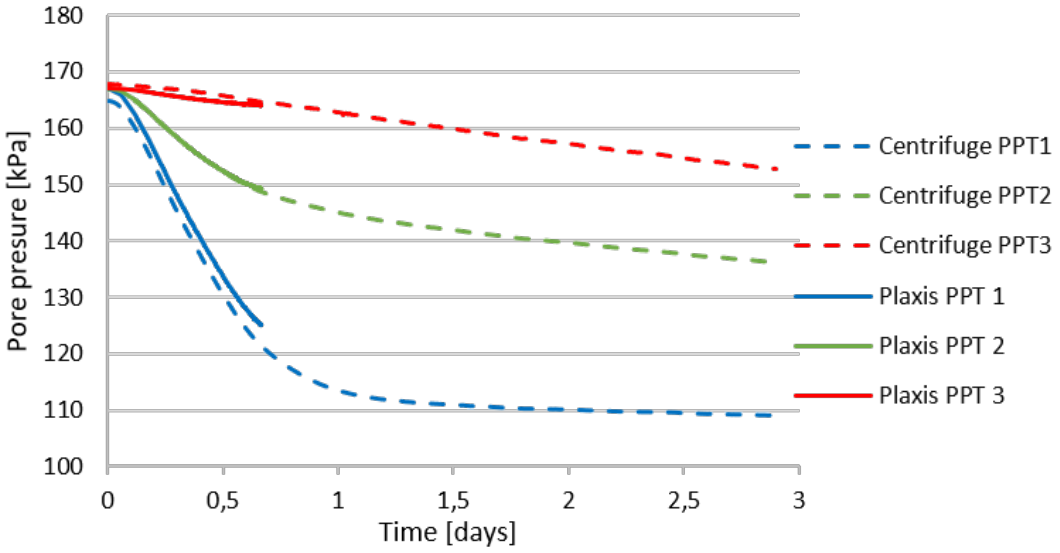

Figure 5.33: Comparison of the pore pressures from centrifuge and numerical data

The pore pressure sensors of the centrifuge give very similar results as the estimation of the numerical model. Only the starting values differ noticeably. This is due to the water level in the centrifuge not being parallel to the strong box floor as described in the previous section. While the numerical model assumes a completely horizontal water level at the start of the test. The numerical estimation stops at around 0.7 days. Afterwards the deformations became to large for the numerical model to continue calculating.

The deformation after the rapid draw down is shown in figure 5.34. The dropdown of water level is at 2.0cm at this figure. A larger dropdown is not possible in the numerical model, because large deformations cause a highly deformed mesh and a subsequent error. The maximum deformation shown in figure 5.34 is smaller than the PIV analysis at the same dropdown (figure 5.29). However, the PLAXIS results show a more traditional circular shape of failure with a larger area of deformation. While the PIV analysis displays a shallower failure with deformation focused on a smaller area. The reason for this difference could be due to PIV software which does not capture very small movements very well, or due to its high standard error. It could be due to heterogeneity in the prototype of the centrifuge test. However, most likely is that PLAXIS does not simulate the high deformations very accurately. As PLAXIS is a continuum model high deformations are difficult to capture.

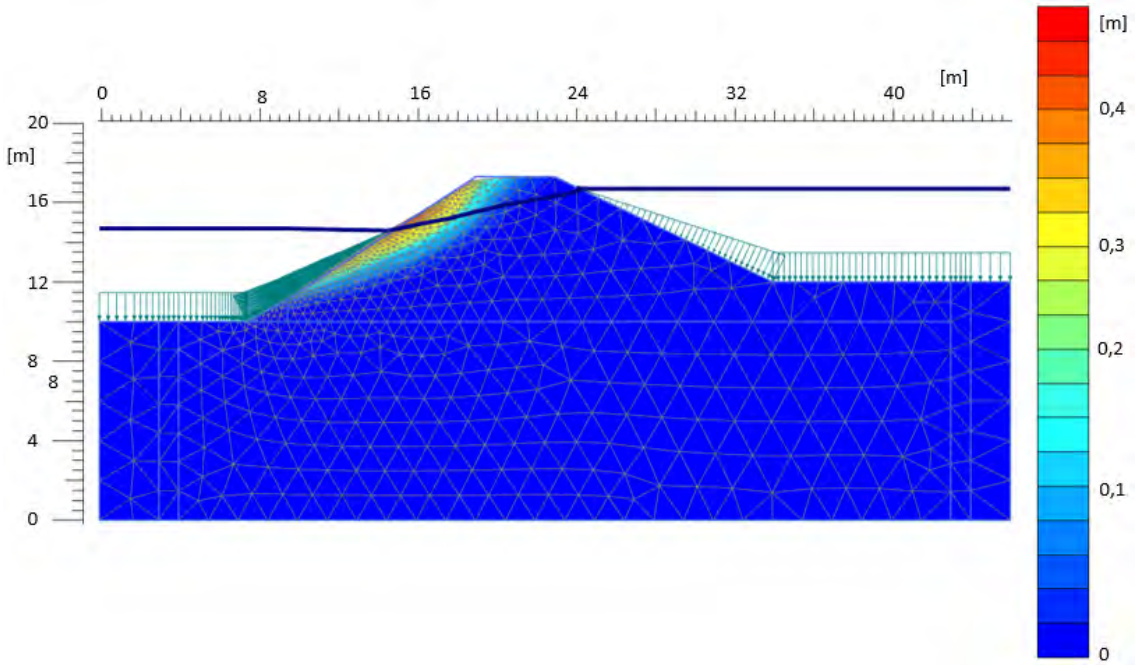

Figure 5.34: deformation after 2m of drawdown

The calculated factor of safety by the PLAXIS model are shown in table 5.4. In the first case the strength parameters are used as stated in section 5.2. In the second case a cohesion is added of 0.1. This can prevent minor failures to happen. In the last case the peak friction angle is used instead of the residual friction angle as input parameter. The centrifuge prototype was stable at the start of the centrifuge test and failed during drawdown. The PLAXIS results show the same with a FoS higher than 1 at the start of the test and a FoS lower than 1 after 2m of drawdown.

Strength parameters	FoS start of test	FoS after 2m of dropdown
phi = 34°c=0 kn/m^2	1.04	<1
phi = 34°c=0.1 kn/m^2	1.10	<1
phi = 44°c=0 kn/m^2	1.34	<1

Table 5.4: Factor of safety for different strength parameters

6

Delta21 dike

To test the stability of the Delta21 dike design, a numerical model with the same shape was made. The numerical model uses a coupled analysis and takes unsaturated soil mechanics into account as described in chapter 3. With the model the stability of the original design is modeled and the effect of the mesh on the results is shown. Afterwards the FoS for multiple different slope angles are calculated. The influence of hysteresis is found after modelling multiple cycles of drawdown. The effect of a drain or permeable layer are found and finally the risk of erosion due to outflowing water is analytically calculated.

In figure 6.1 the design by the Delta21 project can be seen. It is a very gradual slope of 1:25 and 1:20 at the side of the lake. On the seaside the slope is even more gradual with an angle of 1:50. Three layers of sand with a different relative density and properties such as hydraulic conductivity are present. The generated mesh is made with the meshing mode 'fine'. It consists of 1296 elements with 15 nodes per element. The mesh is refined at the left hand side of the dike, because failure is expected here. The mesh is shown in Appendix H figure H.1.
The water level in the lake can be constant for several days during a storm or when the energy market is not favourable for operation. In case of the lake functioning as energy storage the water level can go up and down 17.5m in 24hours. A period of constant high water table followed by rapid draw down causes the highest reduction in FoS. Therefore this path was used during the numerical modelling.

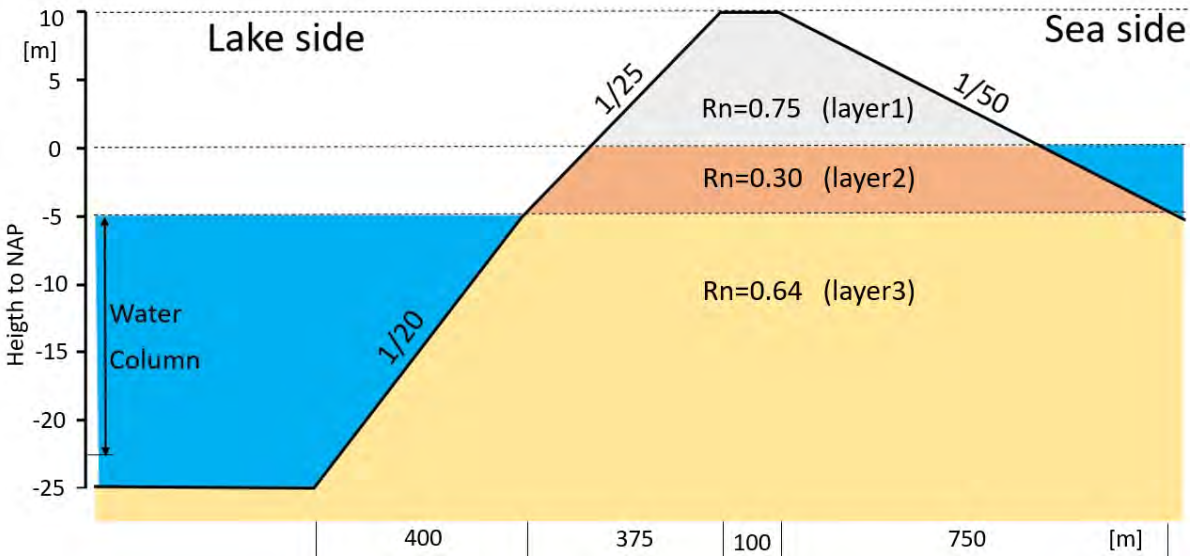

Figure 6.1: Cross section of the dune in Delta21 project

6.1. Effect of the mesh

After the appliance of the phi/c reduction method the numerical model predicts that the dike has a FoS of 6.20 after drawdown. The water level reduces here with 17.5m to a height of 2.5m above the bottom of the lake. After applying the phi/c reduction method, the modeled incremental deformation is found. The incremental deformation is the deformation within the current calculation step. Hereby it needs to be noted that the estimated amount of deformation at failure is unreliable when numerically estimated with a finite element model. The incremental deformation at failure can be seen in figure 6.2. The whole dike was modeled. However, the figure has been zoomed in at the toe of the dike, because this is where the numerical model predicts that the most deformation occurs. The failure contour is smaller than one element of the mesh. If the mesh is refined until the maximum amount at the location of failure, the FoS increases until 6.31. Mesh refinement is generally believed to decrease the FoS (Liu and Glass, 2013). However, table 6.1 does not show this relationship. It is presumably because the failure contour is in all cases smaller than one element. Such small failure contours cause the results to be unreliable.

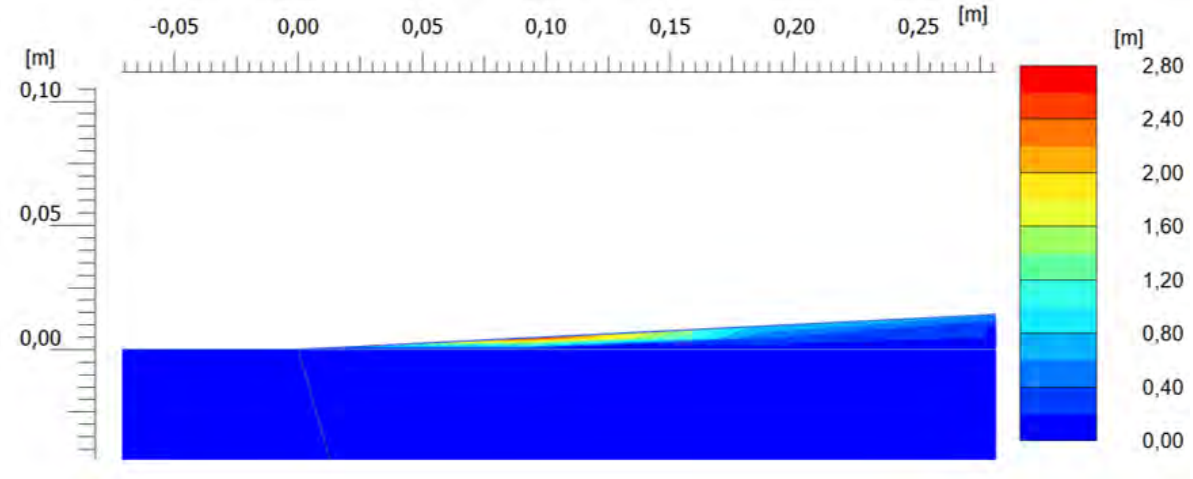

Figure 6.2: Incremental deformation at failure of the Delta21 dike

Meshing mode	Element length at toe perpendicular to sliding surface	Total amount of elements	FoS
'Medium'	0,05	642	6,45
'Fine'	0,05	760	6,08
'Fine' with refinement at left side of the dike including the toe	0,02	1078	6,20
'Very Fine' with maximum refinement at dike toe	0,02	1284	6,31

Table 6.1: effect of mesh density

6.2. Slope angle

As the slope angle increases the failure contour increases in size, while the FoS decreases. When the slope has a height/width ratio of 1/10 the modeled failure contour has increased in size considerably. Figure6.3 shows the incremental deformation at failure. The failure contour is shallow and stretched along the slope between the height of the water level at the start and end of the drop down. Table 6.2 shows the FoS for different slope angles.

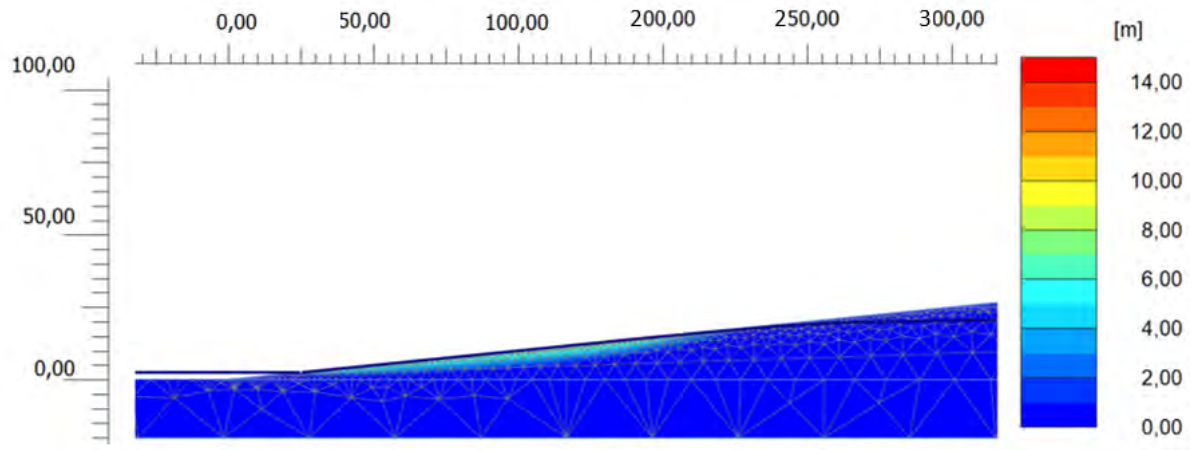

Figure 6.3: Incremental displacement at failure of the dike with height/width ratio 1/10

Slope width/height ratio	FoS before drawdown	FoS after drawdown
Combination 1/20-2/25	11.41	6.20
1/10	5.00	2.98
1/7.5	4.26	2.01
1/5	3.06	1.31
1/4.5	2.54	1.12
1/4	2.30	<1

Table 6.2: FoS of slope wiht different angles

6.3. Multiple cycles of drawdown

Due to the changing water levels within the dike the effective stress alters. As explained in section 2.4.6 multiple cycles of stress increase and decrease can cause strain accumulation and decrease in stiffness, possibly influencing stability.

Before simulating multiple cycles of drawdown the water level is kept constant for 3 days at the highest level. This increases the phreatic water level in the dike to its maximum potential height. Afterwards multiple cycles of 17.5 meter water level decrease and increase are simulated, all with the minimum potential time of 24hours per cycle. Table 6.3 shows the influence of the cycles on the FoS. Because the original design with shallow slopes caused possible unreliable results in the numerical model, a slope with width/height ratio of 1/5 and 1/7.5 are modeled.

Number of drawdowns	1	2	3	4	5	6	7	8
FoS: Slope 1/7.5	2,01	1,98	1,98	1,99	1,99	1,99	1,99	1,99
FoS: Slope 1/5	1,31	1,24	1,25	1,24	1,25	1,25	1,25	1,25

Table 6.3: Influence of multiple cycles of drawdown on FoS

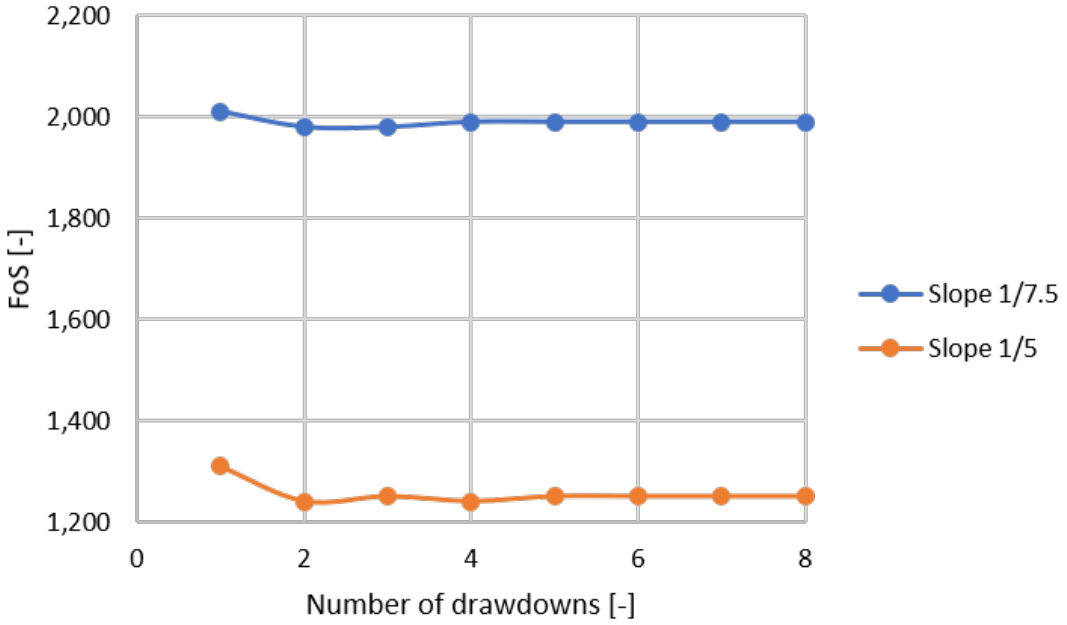

Figure 6.4: Influence of multiple cycles of drawdown of FoS

The FoS between the first and second cycle differs respectively with 0.03 and 0.07 for the slopes with height/width ratio 1/7.5 and 1/5. The drop in the FoS between the first and second cycle of drawdown is due to the development of plastic strain. After the second cycle the stability is hardly influenced further. The yield surface is expanded and new stress changes are to small to cause nonelastic strain. The higher reduction in FoS in the steeper slope indicates a higher amount of strain. This seems logical as the slope is closer to failure.

6.4. Effect of permeable toe

An increase in permeability at the toe of the dike can ward off failure due to flow out of the dike. Chapter 4.2 showed that a drain at the toe of the dike can lead to an increase in stability with respect to macroscopic failure due to rapid draw down. For the reason that it creates a lower phreatic surface in the dike and the gravel has a high internal friction angle. Table 6.4 shows the effect on stability of the slope made with height/width 1/5 potential protective measures have. A gravel drain in the shape of a triangle at the toe of the dike and a cover layer both from gravel are modeled. For the gravel is assumed that it has an internal friction angle of 39°, dilatancy angle of 9°and an hydraulic conductivity of 250m/day. This hydraulic conductivity is based on gravel with no sand in its pores. It has to be noted that over time the hydraulic conductivity of a drain can decrease due to the inflow of sand grains in the pores of the coarser material.

Slope protection	FoS
None	1,31
Gravel toe of 1m height	1,30
Gravel toe of 3m height	1,45
Gravel cover layer of 1m thickness	1,63

Table 6.4: FoS of multiple protection measures of slope height/width 1/5

Chapter 4.2 showed that a permeable toe can lead to a increase the stability. However, in that case the water level was lowered until all water was drained away. In case of the Delta21 dike the water level is altering between 2.5 and 20m height measured from the bottom of the lake. Between these heights the failure develops. For a drain at the toe to have significant influence it needs at least reach the minimum water level of 2.5m. The gravel toe of 3m height increases the FoS, although a failure can develop just above it. A gravel cover layer protects from macroscopic failure due to rapid draw down the best. The failure contour in that case is once more a shallow failure stretched over a large part of the dike.

6.5. Flushing out of grains

The sealevel is at all time at a higher than the waterlevel at the energy storage lake. In combination with the high hydraulic conductivity and the absence of cohesion of the sand, it can lead to grains flushing away. Because PLAXIS is a finite element method it is not suitable for predicting the loss of sand grains from the dike. To give insight in the likelyhood of this to happen two analytical calculation methods from the book of Verruijt were used (Verruijt, 2012). These method for cohesionless materials assumes uniform flow of water caused by a linear pressure distribution, one for flow parallel to the slope and the other horizontal outflow.

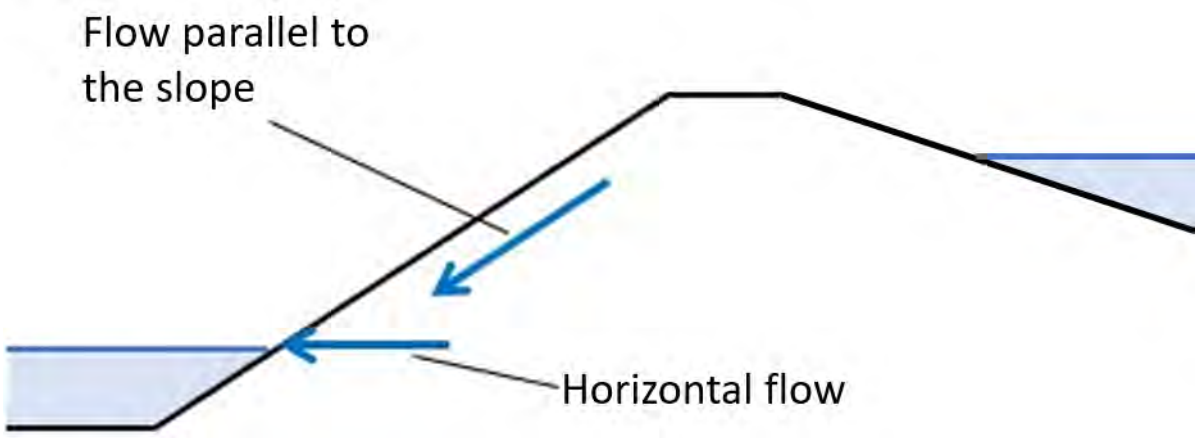

Figure 6.5: Horizontal flow and flow parallel to the slope

For flow parallel to the slope:

$$F = \frac{\gamma - \gamma_w}{\gamma} \frac{tan\phi}{tan\alpha} \tag{6.1}$$

For horizontal outflow:

$$F = \frac{\gamma - \gamma_w / cos^2\alpha}{\gamma} \frac{tan\phi}{tan\alpha} \tag{6.2}$$

Where γ = Volumetric weight
γ_w = Volumetric weight water
α = Slope angle
ϕ = Internal friction angle

As can be seen in figure 6.6, the horizontal outflow gives slightly more conservative result. For a slope angle of 2,86°(1/20) and an internal friction angle of 33°, the lowest calculated factor of safety is 6,43 for horizontal outflow. The expected flow in the Delta21 dike will have a flow direction between horizontal and parallel to the slope. This does not increase the risk of out-flowing grains to a great extent.

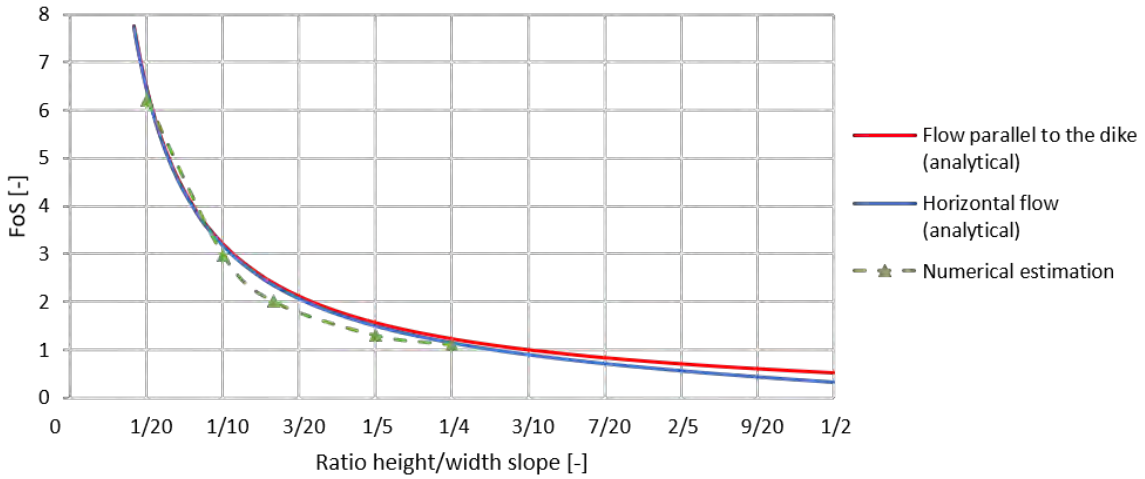

Figure 6.6: FoS of flushing out of grains by horizontal outflow of water by analytical calculation based on Verruijt (2012) and numerically estimated FoS after rapid draw down

Besides the analytical estimations, figure 6.6 shows the numerically modelled FoS after rapid draw down conditions from table 6.2. The results of the numerical model are slightly lower but closely related to the results of the analytical method. Both methods calculate the FoS according to balance equations to find the moment at which failure starts. The closely related results give confidence in the reliability of the numerical model.

6.6. Influence of a possible clay layer

During this research the assumption was made that the dike of the Delta21 project will be fully made of sand. This was assumed for the sake of simplicity and because the current design, found in Ansorena Ruiz (2020), does not include a clay layer as well. However, bore hole data shows the possibility of a clay layer between a depth of 23,5 and 25m below NAP. If this layer is continuous, it could have a large effect on the development of pore pressures and therefore stability. The clay layer could not be modeled with the numerical model used in this research. The combination of the clay layer and the large size of the dike, resulted in a large error in the flow calculation. This caused the numerical model to error. Below the possible influences the clay layer has are described.

A continuous clay layer creates an impermeable boundary for ground water flow. A horizontal flow of water will be created on top of the layer. As mentioned in the previous section 6.5, horizontal flow is more likely to cause erosion.
Furthermore, the phreatic water level in the dike will be higher during drawdown, because water flows away at a slower rate. A higher phreatic water level in the dike will decrease effective stress and therefore decrease the FoS.
The water below the clay layer can not escape causing pore pressure to decrease at a slower rate during drawdown than in a dike without the clay layer. The higher pore pressure can cause cracks in the clay and increase the risk of liquefaction of the sand trapped below the clay layer.

7

Conclusions and recommendations

7.1. Conclusion

The main goal of the research was to find the effect of the rapid draw down on slope stability. After comparing the numerical model with centrifuge tests and a field test from literature, it can be concluded that the fully coupled flow-deformation analysis of PLAXIS2D can give practical insight in the stability of a dike during rapid draw down. Especially the positive pore pressures are precisely estimated. However, the prediction of negative pore pressures are not satisfactory. This is for a large part due to inadequate estimation of saturation, potentially due to incorrect input parameters for the soil water retention curve. Although the estimation of the soil water retention curve by the empirical Modified Kovacs method is slightly better than using standard soil classes, it is not reliable.
The numerical model proved to accurately predict the moment at which macroscopic failures occur due to drawdown. Development of the failure, in terms of size and deformation could not be accurately predicted since it is a finite element model.

The dike of the Delta21 energy storage lake has a straight-forward design constructed out of a single building material. Sand was chosen, since it could be retrieved nearby. The water level changes within the lake are rapid, nevertheless this research has found that rapid drawdown causes no risk for the occurrence of macroscopic failure. This is mostly due to the gentle slope in combination with the high hydraulic conductivity of the sand. Hysteresis due to multiple cycles of draw down negligibly affects the stability. Stability could be increased by adding a gravel filter layer on the dike. The gravel has a high hydraulic conductivity, internal friction angle and is less susceptible to erosion than sand.

Sand has no cohesion and the dike is therefore susceptible for grains leaving the soil body. The water flow through the dike is not likely to be enough to cause these micro failures. Although it was found that micro and macro failures are not likely to occur, several side notes can be made. Erosion due to waves and flow perpendicular to the dike were not taken into consideration. Furthermore, soil characteristics as the strength and permeability are taken to be uniform characteristics.

7.2. Recommendations

The results of the numerical model show that the dike of the Delta21 project is stable under rapid draw down conditions. However, the design is rather staight-forward and a more sophisticated design can potentially decrease costs and increase safety.

The current slope is not susceptible to macro-failures due to changes in hydraulic pressures. An increase in slope angle would increase feasibility of the project without causing concerning safety issues. On the other hand the current design is sensitive for erosion, especially at the toe of the dike. The construction material has no cohesion and can be easily picked up by the water current. Analytical calculations predict that water flow through the dike is not enough to cause erosion. However, with the addition of flow perpendicular to the dike and wave impact, erosion seems likely. The increase of cohesion on the top surface could prevent erosion. Addition of a clay layer or cementing grains are viable options. However, the decrease in hydraulic conductivity leads to an increase in hydraulic pressures. This negatively influences macro stability and can induce water flow underneath the cohesive layer. Placing a layer of coarse gravel or rocks is therefore advised. They are less susceptible to transport by water flow and are positively influencing macro-stability. Nevertheless, sand grains can still flush through this layer.

The estimation of material properties of the sand in the Delta21 area are based on limited CPT data, samples from the adjacent Maasvlakte II and empirical relationships. A sample from the site to perform laboratory test on would be a more reliable source of information and would improve the accuracy of predictions. Especially the stress-strain curve from a simple shear test would give insight in the internal friction angle, an important material property for stability. With this information the effect of densification of the dike on stability can be found.

Further research on the effect of an extra clay layer in the dike during rapid draw down conditions with respect to stability is encouraged. Although being time consuming, physical modelling at a high gravitational acceleration level proved suitable for modeling rapid draw down conditions. The potential for centrifuge tests to gain insight in erosion could be further investigated as well. In this case PIV analysis will be a good source of information. Close attention needs to be paid to lighting as during spinning of the centrifuge it was difficult for the software to differentiate individual grains.

Improvements on the numerical modeling might include the use of advanced numerical techniques, such as large deformation models or discrete elements. These might take the erosion process into account, hence providing a better stability analysis. The use of these advanced techniques should be performed with a fully coupled analysis.

References

Alderlieste, E. A., Dijkstra, J., and van Tol, A. F. Experimental investigation into pile diameter effects of laterally loaded mono-piles. In *ASME 2011 30th international conference on ocean, offshore and arctic engineering*, pages 985–990. American Society of Mechanical Engineers Digital Collection, 2011.

Alonso, E., Pérez de Agreda and Pinyol Puigmartí, N. M. Slope stability under rapid drawdown conditions. In *First Italian Workshop on Landslides*, pages 11–27, 2009.

Alonso, E. E. and Pinyol, N. M. Numerical analysis of rapid drawdown: Applications in real cases. *Water Science and Engineering*, 9(3):175–182, 2016.

Alonso Pérez de Agreda, E. and Pinyol Puigmartí, N. M. Slope stability under rapid drawdown conditions. In *First Italian Workshop on Landslides*, pages 11–27, 2009.

Ansorena Ruiz, R. Conceptual design of the valmeer's pump storage station of the delta21 plan. 2020.

Arya, L., Paris, M., and Jack, F. A physicoempirical model to predict the soil moisture characteristic from particle-size distribution and bulk density data. *Soil Science Society of America Journal*, 45(6):1023–1030, 1981.

Askarinejad, A. *Failure mechanisms in unsaturated silty sand slopes triggered by rainfall*, volume 248. vdf Hochschulverlag AG, 2015.

Assouline, S., Tessier, D., and Bruand, A. A conceptual model of the soil water retention curve. *Water Resources Research*, 34(2):223–231, 1998.

Bezuijen, A. and Den Adel, H. Dike failure due to surface erosion ng and 1 g tests. In *Proc. 6th Int. Conf. on Physical Modelling in Geotechnics*, 2006.

Bishop, A. W. The principle of effective stress. *Teknisk ukeblad*, 39:859–863, 1959.

Booster, L., Loman, G., Dykstra, C., and Van der Meer, J. Maasvlakte 2: Geotechnische beoordeling van aanleggebied. *Projectorganisatie Uitbreiding Maasvlakte (PUMA)*, 2008.

Brandl, H. and Szabo, M. Hydraulic failure of flood protection dykes. In *Proceedings of the 18th international conference on soil mechanics and geotechnical engineering, Paris*, 2013.

Brinkgreve, R., Kappert, M., and Bonnier, P. Hysteretic damping in a small-strain stiffness model. *Proc. of Num. Mod. in Geomech., NUMOG X, Rhodes*, pages 737–742, 2007.

Burdine, N. et al. Relative permeability calculations from pore size distribution data. *Journal of Petroleum Technology*, 5(03):71–78, 1953.

Burland, J. On the compressibility and shear strength of natural clays. *Géotechnique*, 40(3):329–378, 1990.

Carrier III, W. D. Goodbye, hazen; hello, kozeny-carman. *Journal of geotechnical and geoenvironmental engineering*, 129(11):1054–1056, 2003.

Carsel, R. F. and Parrish, R. S. Developing joint probability distributions of soil water retention characteristics. *Water resources research*, 24(5):755–769, 1988.

Chavez Abril, M. A. Numerical simulations of static liquefaction in submerged slopes. 2017.

CROW. Handboek zandboek. *CROW, Ede, the Netherlands*, 2004.

CROW. Standaard raw bepalingen 2020. 2020.

Dijkstra, J., Broere, W., Bezuijen, A., and Van Tol, A. 44 density changes near an advancing displacement pile in sand. 2008.

Dos Santos, J. and Gomes Correia, A. Reference threshold strain of soil. its application to obtain an unique strain-dependent shear modulus curve for soil. In *International Conference on soil mechanics and geotechnical engineering*, pages 267–270, 2001.

Duncan, J. M., Wright, S. G., and Wong, K. S. Slope stability during rapid drawdown. In *Proceedings of the H. Bolton seed memorial symposium*, volume 2, pages 253–272, 1990.

Fattah, M. Y., Omran, H. A., and Hassan, M. A. Behavior of an earth dam during rapid drawdown of water in reservoir–case study. *International Journal of Advanced Research (2015)*, 3(10):110–122, 2015.

Fredlund, D. G. and Xing, A. Equations for the soil-water characteristic curve. *Canadian geotechnical journal*, 31(4):521–532, 1994.

Galavi, V. Groundwater flow, fully coupled flow deformation and undrained analyses in plaxis 2d and 3d. *Plaxis Report*, 2010.

Gao, Y., Wang, Y.-H., and Su, J. C. Experimental characterization of the influence of fines on the stiffness of sand with inherent fabric anisotropy. *Soils and Foundations*, 55(5):1148–1157, 2015.

Gao, Y., Zhu, D., Zhang, F., Lei, G., and Qin, H. Stability analysis of three-dimensional slopes under water drawdown conditions. *Canadian Geotechnical Journal*, 51(11):1355–1364, 2014.

Geologische Dienst, N. Dinoloket, geraadpleegd in augustus 2020, 2020.

Ghayoomi, M., Suprunenko, G., and Mirshekari, M. Cyclic triaxial test to measure strain-dependent shear modulus of unsaturated sand. *International Journal of Geomechanics*, 17(9):04017043, 2017.

Hagos, D. A., Gebremedhin, A., and Zethraeus, B. Towards a flexible energy system–a case study for inland norway. *Applied energy*, 130:41–50, 2014.

Hardin, B. O. and Black, W. L. Sand stiffness under various triaxial stresses. *Journal of Soil Mechanics & Foundations Div*, 92(ASCE# 4712 Proceeding), 1966.

ITTC. Ittc–recommended procedures fresh water and seawater properties. IITC, 2011.

Jaky, J. The coefficient of earth pressure at rest. *J. of the Society of Hungarian Architects and Engineers*, pages 355–358, 1944.

Jommi, C. Remarks on the constitutive modelling of unsaturated soils. *Experimental evidence and theoretical approaches in unsaturated soils*, pages 139–153, 2000.

Khalili, N., Geiser, F., and Blight, G. Effective stress in unsaturated soils: Review with new evidence. *International journal of Geomechanics*, 4(2):115–126, 2004.

Kovács, G. *Seepage hydraulics*. Elsevier, 2011.

Kramer, S. Geotechnical earthquake engineering. Prentice Hall, 1996.

Krapfenbauer, C. Experimental investigation of static liquefaction in submarine slopes. *MSc Thesis, TU Delft*, 2016.

Lane, P. and Griffiths, D. Assessment of stability of slopes under drawdown conditions. *Journal of geotechnical and geoenvironmental engineering*, 126(5):443–450, 2000.

Lavooij, H., Berle, L., Tonneijck, M., De Boer, H., and Vrijling, H. Delta21 deelrapport waterveiligheid. 2018.

Li, D., Yin, K., and Leo, C. Analysis of baishuihe landslide influenced by the effects of reservoir water and rainfall. *Environmental Earth Sciences*, 60(4):677–687, 2010.

Likos, W. J., Lu, N., and Godt, J. W. Hysteresis and uncertainty in soil water-retention curve parameters. *Journal of Geotechnical and Geoenvironmental Engineering*, 140(4):04013050, 2014.

Liu, Y. and Glass, G. Effects of mesh density on finite element analysis. Technical report, SAE Technical Paper, 2013.

Luckner, L., Van Genuchten, M. T., and Nielsen, D. A consistent set of parametric models for the two-phase flow of immiscible fluids in the subsurface. *Water Resources Research*, 25(10):2187–2193, 1989.

Maqsoud, A., Bussière, B., Aubertin, M., and Mbonimpa, M. Predicting hysteresis of the water retention curve from basic properties of granular soils. *Geotechnical and Geological Engineering*, 30(5):1147–1159, 2012.

Mayor, P. A. *Verhalten eines Flussdammes unter wiederholter Hochwasserbelastung*, volume 245. vdf Hochschulverlag AG, 2014.

Meehl, G. A., Zwiers, F., Evans, J., Knutson, T., Mearns, L., and Whetton, P. Trends in extreme weather and climate events: issues related to modeling extremes in projections of future climate change. *Bulletin of the American Meteorological Society*, 81(3):427–436, 2000.

Mualem, Y. Hydraulic conductivity of unsaturated soils: prediction and formulas. *Methods of Soil Analysis: Part 1 Physical and Mineralogical Methods*, 5:799–823, 1986.

Noborio, K. Measurement of soil water content and electrical conductivity by time domain reflectometry: a review. *Computers and electronics in agriculture*, 31(3):213–237, 2001.

Novák, v. and Hlaváčiková, H. Soil-water retention curve. In *Applied Soil Hydrology. Theory and Applications of Transport in Porous Media*, page vol 32, 2019.

Nuth, M. Constitutive modelling of unsaturated soils with hydro-geomechanical couplings. Technical report, EPFL, 2009.

Oosterbaan, R. and Nijland, N. 12 determining the saturated hydraulic conductivity. 1994.

Paasman, Y. Design for the in- and outlet structure of the energy storage lake within the delta21 plan. 2020.

Paprotny, D., Sebastian, A., Morales-Nápoles, O., and Jonkman, S. N. Trends in flood losses in europe over the past 150 years. *Nature communications*, 9(1):1985, 2018.

Paton, J. and Semple, N. Investigation of the stability of an earth dam subjected to rapid drawdown including details of pore pressure recorded during a controlled drawdown test. *Pore pressure and suction in soils*, pages 85–90, 1961.

Peñuela, W. F. M. *River dyke failure modeling under transient water conditions*, volume 247. vdf Hochschulverlag AG, 2015.

Peters, A. and Durner, W. A simple model for describing hydraulic conductivity in unsaturated porous media accounting for film and capillary flow. *Water Resources Research*, 44(11), 2008.

Philip, J. Unitary approach to capillary condensation and adsorption. *The Journal of Chemical Physics*, 66 (11):5069–5075, 1977.

Plaxis. Plaxis materials models connect edition v20. 2019.

Prof. Pieter Vermeer, D. R. B. Plaxis bullitin nr13. *Plaxis Users Association (NL)*, 20, 2003.

R, B. personal consult. 2020.

Richards, L. A. Capillary conduction of liquids through porous mediums. *Physics*, 1(5):318–333, 1931.

Schanz, T. and Vermeer, P. On the stiffness of sands. In *Pre-failure deformation behaviour of geomaterials*, pages 383–387. Thomas Telford Publishing, 1998.

Schmertmann, J. An updated correlation between relative density dr and fugro-type electric cone bearing, qc. *Contract Report DACW*, pages 39–76, 1976.

Schmertmann, J. H. Guidelines for cone penetration test: performance and design. Technical report, United States. Federal Highway Administration, 1978.

Schofield, A. N. Cambridge geotechnical centrifuge operations. *Geotechnique*, 30(3):227–268, 1980.

Skempton, A. The pore-pressure coefficients a and b. *Geotechnique*, 4(4):143–147, 1954.

Souliyavong, T., Gallage, C., Egodawatta, P., and Maher, B. Factors affecting the stability analysis of earth dam slopes subjected to reservoir drawdown. In *Proceedings of the Second International Conference on Geotechnique, Construction Materials and Environment*, pages 507–512. The GEOMATE International Society, 2012.

Stokoe, K., Darendeli, M., Andrus, R., and Brown, L. Dynamic soil properties: laboratory, field and correlation studies. *Proc. 2nd Int. Conf. on Earthquake geotech. Eng.*, 3:811–845, 1999.

TAW. Technical report on water retaining structures. Technical report, Technische Adviescommissie voor Waterkeringen, (in Dutch), 2001.

Taylor, R. Centrifuges in modelling: principles and scale effects. In *Geotechnical centrifuge technology*, pages 19–33. CRC Press, 2018.

Terzaghi, K. v. The shearing resistance of saturated soils and the angle between the planes of shear. In *First international conference on soil Mechanics, 1936*, volume 1, pages 54–59, 1936.

Terzaghi, K. Theoretical soil mechanics. johnwiley & sons. *New York*, pages 11–15, 1943.

TNO Geologische Dienst, N. Dinoloket, 2018.

Van Genuchten, M. T. A closed-form equation for predicting the hydraulic conductivity of unsaturated soils 1. *Soil science society of America journal*, 44(5):892–898, 1980.

Van Genuchten, M. T., Leij, F., Yates, S., et al. The retc code for quantifying the hydraulic functions of unsaturated soils. 1991.

Vanden Berge, D. *Rapid drawdown analysis using the finite element method*. PhD thesis, Virginia Tech, 2014.

Vandenberge, D. R. Total stress rapid drawdown analysis of the pilarcitos dam failure using the finite element method. *Frontiers of Structural and Civil Engineering*, 8(2):115–123, 2014.

Vermeer, P. A. and De Borst, R. Non-associated plasticity for soils, concrete and rock. *HERON, 29 (3), 1984*.

Verruijt, A. *Soil mechanics*. Delft University of Technology The Netherlands, 2012.

Vessies, W. Relative density differences of a sand fill. 2012.

Viratjandr, C. and Michalowski, R. L. Limit analysis of submerged slopes subjected to water drawdown. *Canadian Geotechnical Journal*, 43(8):802–814, 2006a.

Viratjandr, C. and Michalowski, R. L. Limit analysis of submerged slopes subjected to water drawdown. *Canadian Geotechnical Journal*, 43(8):802–814, 2006b.

Vrielink, L. Stability of dike slobes for a changing water table. 2020.

Wang, J.-J., Zhang, H.-P., Zhang, L., and Liang, Y. Experimental study on heterogeneous slope responses to drawdown. *Engineering geology*, 147:52–56, 2012.

White, D., Take, W., and Bolton, M. Soil deformation measurement using particle image velocimetry (piv) and photogrammetry. *Geotechnique*, 53(7):619–631, 2003.

Wichtmann, T. and Triantafyllidis, T. Effect of uniformity coefficient on g/g max and damping ratio of uniform to well-graded quartz sands. *Journal of geotechnical and geoenvironmental engineering*, 139(1):59–72, 2013.

Wichtmann, T., Hernández, M. N., and Triantafyllidis, T. On the influence of a non-cohesive fines content on small strain stiffness, modulus degradation and damping of quartz sand. *Soil Dynamics and Earthquake Engineering*, 69:103–114, 2015.

Windfinder. Getijden oostvoorne. `https://nl.windfinder.com/tide/oostvoorne`, 2020. Accessed: 2020-10-19.

Xu, R. and Fatahi, B. Three dimensional numerical analysis of seismic soil-structure interaction considering soil plasticity. In *INTERNATIONAL CONFERENCE ON EARTHQUAKE GEOTECHNICAL ENGINEERING*. The New Zealand Geotechnical Society (NZGS), 2015.

Yan, Z.-L., Wang, J.-J., and Chai, H.-J. Influence of water level fluctuation on phreatic line in silty soil model slope. *Engineering Geology*, 113(1-4):90–98, 2010.

Zhang, T., Yan, E., Cheng, J., and Zheng, Y. Mechanism of reservoir water in the deformation of hefeng landslide. *Journal of Earth Science*, 21(6):870–875, 2010.

A

PLAXIS2d coupled analysis

A.1. Groundwater flow in the coupled analysis

To find the groundwater flow for the saturated and non-saturated permeability a soil-water retention curve is used, relating the suction in the unsaturated zone to the volumetric water content.

To find the soil hydraulic parameters needed, the soil is placed in one of the twelve textural classes of the USDA soil textural triangle. The soil hydraulic parameters of this textural class are needed for equations A.2, A.1 and A.3, the parameters are taken from Carsel and Parrish (1988). The textural class is chosen based upon the particle fractions, which can set by default.

Van Genuchten (1980) is used in PLAXIS to describe the hydraulic behavior of unsaturated soils. It is taken because it is relatively accurate and a very common method in literature (Peters and Durner, 2008). The Van Genuchten function relates the saturation to the pressure head ψ:

$$S(\psi) = S_{res} + (S_{sat} - S_{res})[1 + (g_a \mid \psi \mid)^{g_n}]^{g_c} \tag{A.1}$$

Where $\psi = -\frac{p_w}{\gamma_w}$l

p_w = suction pore stress
γ_w = Unit weight of the pore fluid
S_{res} = Residual saturation
S_{sat} = Saturation level of the pores
g_a = Fitting parameter related to the air entry value of the soil
g_n = Fitting parameter which is a function of the rate of water extraction from the soil once the air entry value has been
h_z = fitting parameter with the following assumption to convert the Van Genuchten to a two-parameter equation $G_c = \frac{1}{}$

To describe the saturation from the minimum residual saturation the effective saturation is used. The effective saturation is used to estimate the weight of the soil as a ratio between the unsaturated and saturated weigth. Furthermore, it has influence on the unsaturated hydraulic conductivity and the suction pressure. It is defined as in the following formula (Plaxis, 2019).

$$S_{eff} = \frac{S - S_{res}}{S_{sat} - S_{res}} \tag{A.2}$$

The relative permeability according to Van Genuchten now reads as described in equation A.3. It is to be noted that this formula makes no difference in drying and wetting. This is incorrect as described as shown in the previous chapter in figure C.1.

$$k_{rel}(S) = max\left[(S_{eff})^{g_r}\left(1 - \left[1 - S_{eff}^{(\frac{g_n}{g_n-1})}\right]^{(\frac{g_n-1}{g_n})}\right)^2, 10^{-4}\right] \tag{A.3}$$

A.1.1. Bishop's effective stres

The effective saturation is used to calculate suction according to the Bishop's stress. The effective saturation is taken as the effective stress parameter (χ). The effective saturation is multiplied with the matric suction to prevent the suction to become unrealisticly large at low water content. At full saturation Bishop's stress is equal to Terzaghi's stress. (Galavi, 2010)

$$\sigma' = (\sigma - u_a) + S_{eff}(u_a - u_w) \tag{A.4}$$

A.2. factor of safety

To find the factor of safety, the phi/c reduction or strength reduction method is used. Hereby the parameters $tan(\psi)$ and cohesion (c) as well as the tensile strength are successively reduced until failure of the structure occurs. When the friction angle is equal to the dilatancy angle, these is lowered as well. The ratio available strength and strength at failure gives the safety factor at failure.

$$\sum Msf = \frac{tan\phi_{input}}{tan\phi_{reduced}} = \frac{C_{input}}{C_{reduced}} = \frac{s_{u,input}}{s_{u,reduced}} = \frac{Tensilestrength_{input}}{Tensilestrength_{reduced}} \tag{A.5}$$

Collapse is assumed when the applied load reduces in magnitude in X successive calculation steps and the current stiffness parameter (CSP) is less than 0.015. The CSP is defined as:

$$Stiffness = \int \frac{\Delta\epsilon * \Delta\sigma}{\Delta\epsilon\Delta^e\Delta\epsilon} \tag{A.6}$$

This measures the amount of plasticity occurring. The CSP parameter is used in the calculation for the global error. The global error is defined as:

$$Globalerror = \frac{|\,unbalanceforce\,|}{|\,currentlyactivatedload\,| + CSP * |\,previouslyactivatedload\,|} \tag{A.7}$$

Where the unbalance force the difference is between the external and internal reactions. The global error is fixed to 1%. The denominator becomes smaller close to failure due to reduced stiffness and less load added. Therefore the unbalance is lower close to failure(Personal communication, R. Brinkgreve. 2020).

B

Analytical estimation of infinite slope

B.0.1. Analytical calculation

To verify the numerical model it is compared with centrifuge tests and field tests. In this chapter the FoS will be compared with a analytical estimation from the book of Verruijt (2012). According to Verruijt (2012) the factor of safety of an infinite slope of sand is the same of a dry slope as of a slope under water. It reads:

$$F = \frac{strength}{load} = \frac{tan\phi}{tan\alpha} \tag{B.1}$$

where $\varphi$is the internal friction angle and $\alpha$is the slope angle. With φ=33 and α=18,4 (slope 1/3) this results in a FoS of 1,948.

Although an infinite dike is impossible to model in a finite element model, a dike with an height of 100m is made. This is with the coupled analysis with a Mohr Coulomb model. This dike has the same slope angle and made from sand with the same internal friction angle. It is placed fully under water. Without changing any of the boundary conditions this results in a FoS of 1,944. For a fully dry slope, so without considering suction, it is 1,924. The alikeness between the FoS of the numerical and analytical solution give an indication that the numerical model is fairly accurate in this situation. It is shown that it is worthwhile to further investigate the potential and correctness of the numerical model.

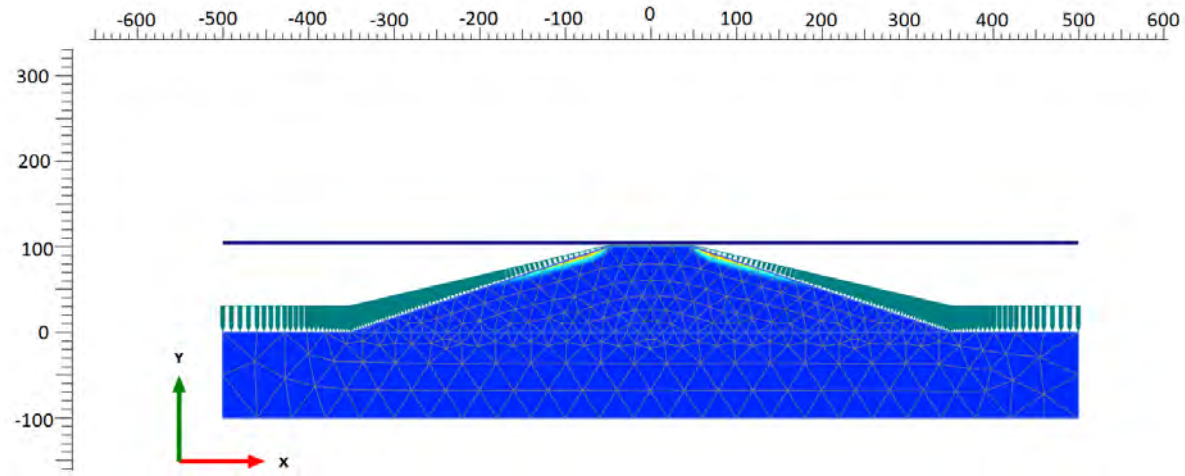

Figure B.1: deviatoric strain at failure for constant high water table

C

Scaling laws of a geotechnical centrifuge

This chapter explains the theoretical background on the scaling laws of the Geotechnical Centrifuge.

C.0.1. Scaling laws for infiltration and rapid draw down

According to Schofield (1980) seepage in the dike will occur N times faster due to an N times higher centrifugal acceleration. Because length of the model is N times shorter the seepage time will be faster with a factor of N^2 in macroscopic scale. When looking at grain scale, the grain size will be equal in the prototype and the model. Therefore the seepage length is the same as the prototype at microscopic scale and accordingly the seepage time in the model will be less with a factor N.

C.0.2. Scaling laws for the static liquefaction mechanism (microscopic)

The rapid draw down in the dike can cause static liquefaction as a failure mechanism. Hereby a loss of strength occurs of a loose contractive material under undrained conditions. (Olson et al., 2000; Chu et al., 2003; Casini et al.,2010a). The loss of strength is due to a reduction in effective stress and shear strength, after locally increased pore pressures. Therefore it is important to look at the grain scale and structure of the soil in the model. In this chapter the scaling laws on the grain scale for static liquefaction will be discussed, as described by Askarinejad (2015).

As can be seen in table C.1, the length on grain scale has a scaling factor of 1, because the assumption is made that the same grain size, void ratio and initial water content will be used in the model and the prototype. Although 'younger' reconstituted models normally have larger voids compared to the natural samples (Burland, 1990).

The time scale for gravitational falling T_impact[1] of a particle at grain scale would be:

$$T_{impact} = \sqrt{\frac{2L}{a}}, \quad \frac{L_m}{L_p} = 1, \quad \frac{a_m}{a_p} = N => \frac{T_{impact,m}}{T_{impact,p}} = \sqrt{\frac{1}{N}} \tag{C.1}$$

Where L is the falling height, a is the acceleration and subscripts p and m stand for prototype and model respectively. It is based upon the assumption of falling with zero initial velocity and at a constant acceleration.

Darcy's law can be used to calculate the velocity of dissipation of excess pore pressure. In figure C.1 the flow of a liquid from point A to B can be seen. This flow will be governed by the hydraulic gradient between these two points and the hydraulic conductivity of soil along the path. The total hydraulic head (H) at points A and B in the model and prototype can be calculated using the following equation.

$$H_{a,p} = \frac{h_p * \gamma_{f,p}}{\gamma_f} + \frac{W_p}{s.\gamma_f}, \quad H_{B,P} = 0, \quad H_{A,m} = \frac{h_m * \gamma_{f,m}}{\gamma_f} + \frac{W_m}{s.\gamma_f} = N * h_p + \frac{N * W_p}{S * \gamma_f} = N * H_{A,P} \quad H_{b,m} = 0 \tag{C.2}$$

Where, H is the total hydraulic head where the elevation head between point a and b is neglected, W is the weight of the falling particle, h is the height of the saturated pore, γ_f is the unit weight of a reference pore

fluid at $1g^2$, and S is the cross sectional area of the pore.

The hydraulic conductivity and the distance between points A and B are similar in the model and the prototype, accordingly the seepage and the pore pressure dissipation time will be N times faster in the model compared to the prototype:

$$v_{A-B} = k\frac{\Delta H_{AB}}{D_{AB}} => V_{A-B,m} = k\frac{N.\Delta H_{AB,p}}{D_{AB}} = N.V_{A-B,p} => \frac{T_{dissipation,m}}{T_{dissipation,p}} = \frac{1}{N} \tag{C.3}$$

It is concluded that under Ng acceleration, the impact time of a particle is reduced by a factor of $\sqrt{1/N}$, while the localised dissipation of the excess pore fluid pressure will N times faster than the prototype. This means that the increased acceleration provides a condition in which the excess pore pressure dissipates $\sqrt{1/N}$ faster than the collapse of the soil structure. Therefore, to reduce the dissipation time in the model a fluid $\sqrt{1/N}$ times more viscous than water can be considered.

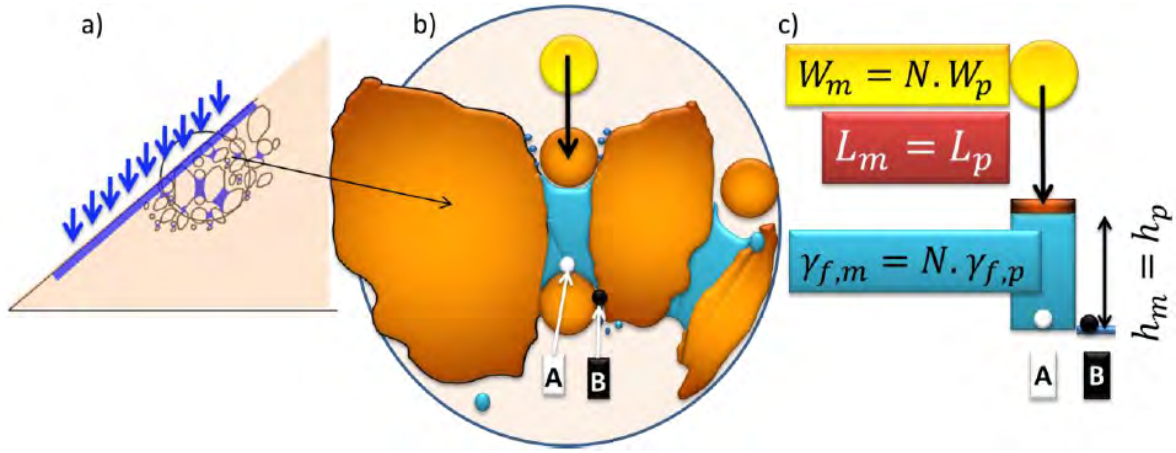

Figure C.1: a) Schematic of the slope b) microstructure of the soil pores showing one particle impacting another one vertically c) conceptual model under Ng acceleration (Askarinejad, 2015).

Table C.1: scaling laws of the geotechnical centrifuge

Term [Dimension]	Prototype	Model
Length (macroscopic) [L]	1	1/N
Length (grain scale) [L]	1	1
Seepage velocity (macroscopic and grain scale) [L/T]	1	N
Seepage time /(macroscopic) [T]	1	$1/N^2$
Seepage time /(grain scale) [T]	1	$1/N^2$
Time	1	$1/N^2$
Hydraulic gradient (macroscopic) [L/L]	1	N
Density	1	1

D

soil characteristics

D.0.1. soil parameters of gravel toe of Deltares centrifuge test

Geotechnical properties Baskarp sand		
Saturated weight [kN/m^3]	γ_{sat}	19,5
Unsaturated weight [kN/m^3]	γ_{unsat}	17,0
Initial void ratio [-]	$e_{initial}$	0,4
Young's modulus[kN/m^2]	E	223.300
Cohesion [kN/m^2]	c'	0
Internal friction angle [°]	φ	40
Dilatancy angle [°]	ψ	15
Poisson's ratio [-]	ν'_{ur}	0,4
Soil fragment [%]	<2 µm	10
Soil fragment [%]	2 µm - 50 µm	13
Soil fragment [%]	>50 µm	77
Permeability [m/day]	$K_x = K_y$	250

Table D.1: Soil parameters gravel used in toe of numerical model in Deltares remake

E

Ground investigation

At the locations shown in Figures E.11, E.12 and E.13, the CPT results until -35m NAP found in Dinoloket are presented in this section TNO Geologische Dienst (2018).

Figure E.1: CPT S36H00032-01

Figure E.2: CPT S36H00033-00

Figure E.3: CPT S36H00035-01

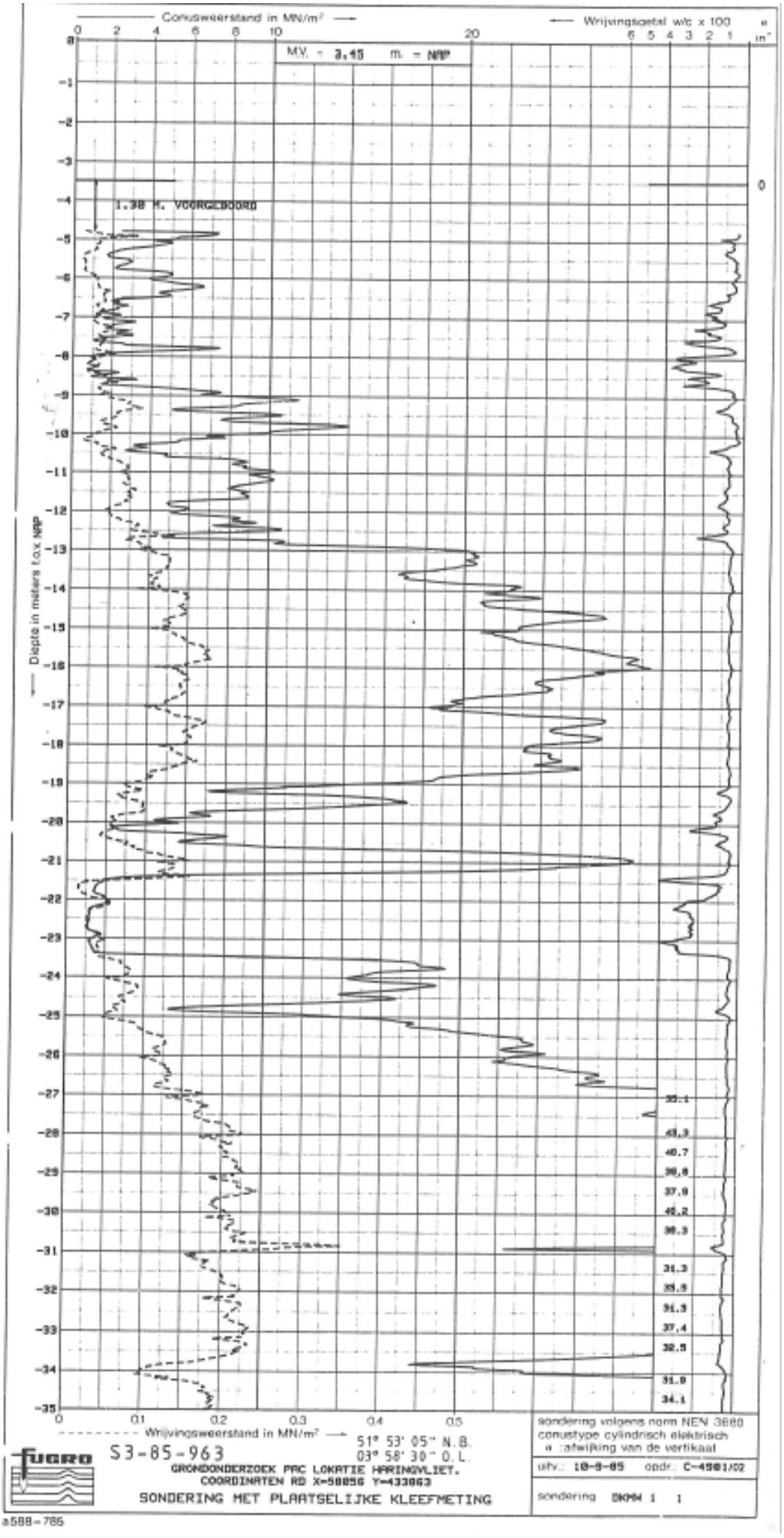

Figure E.4: CPT result from S36H00035-01

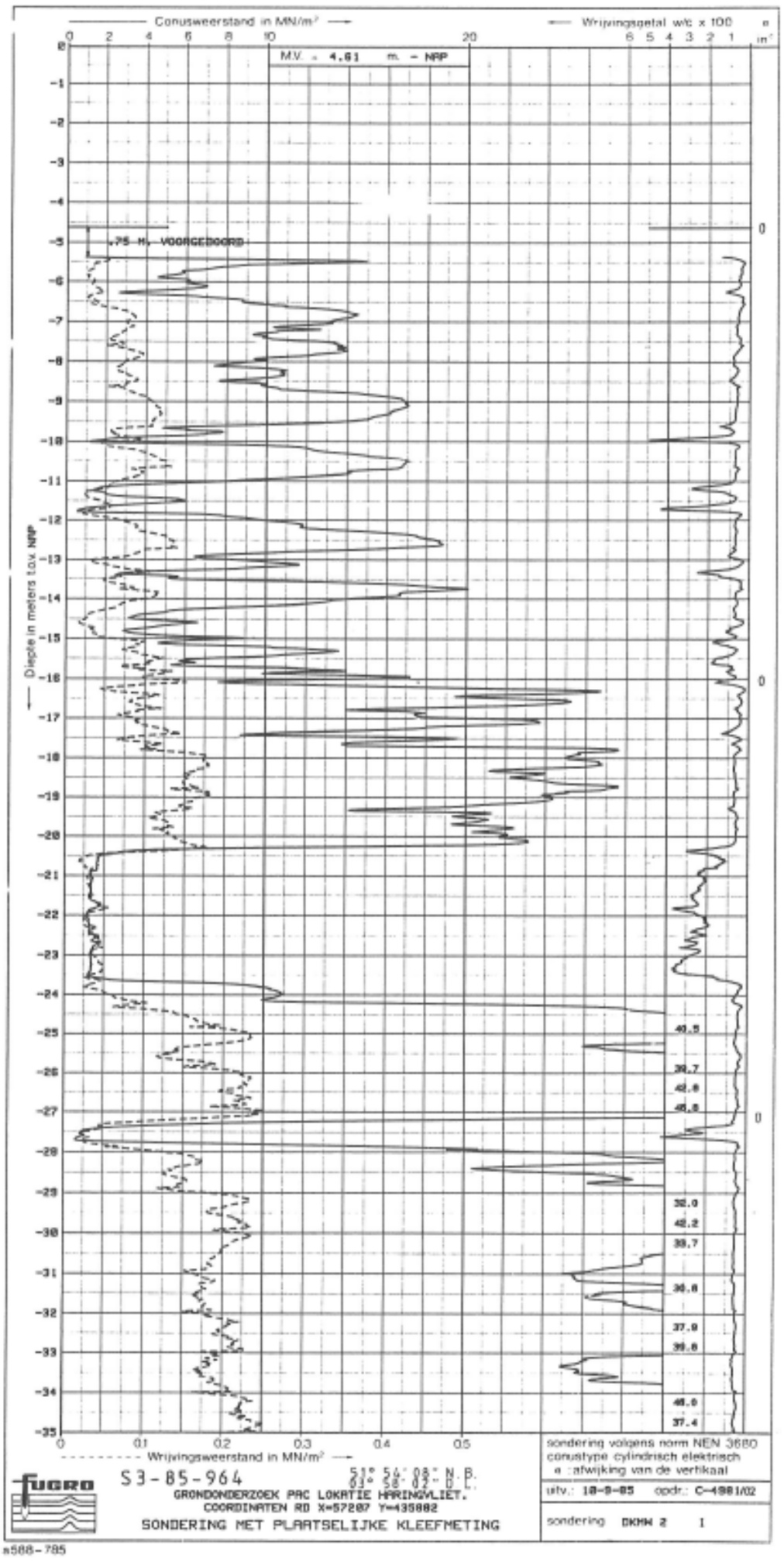

Figure E.5: CPT result from S36H00033-00

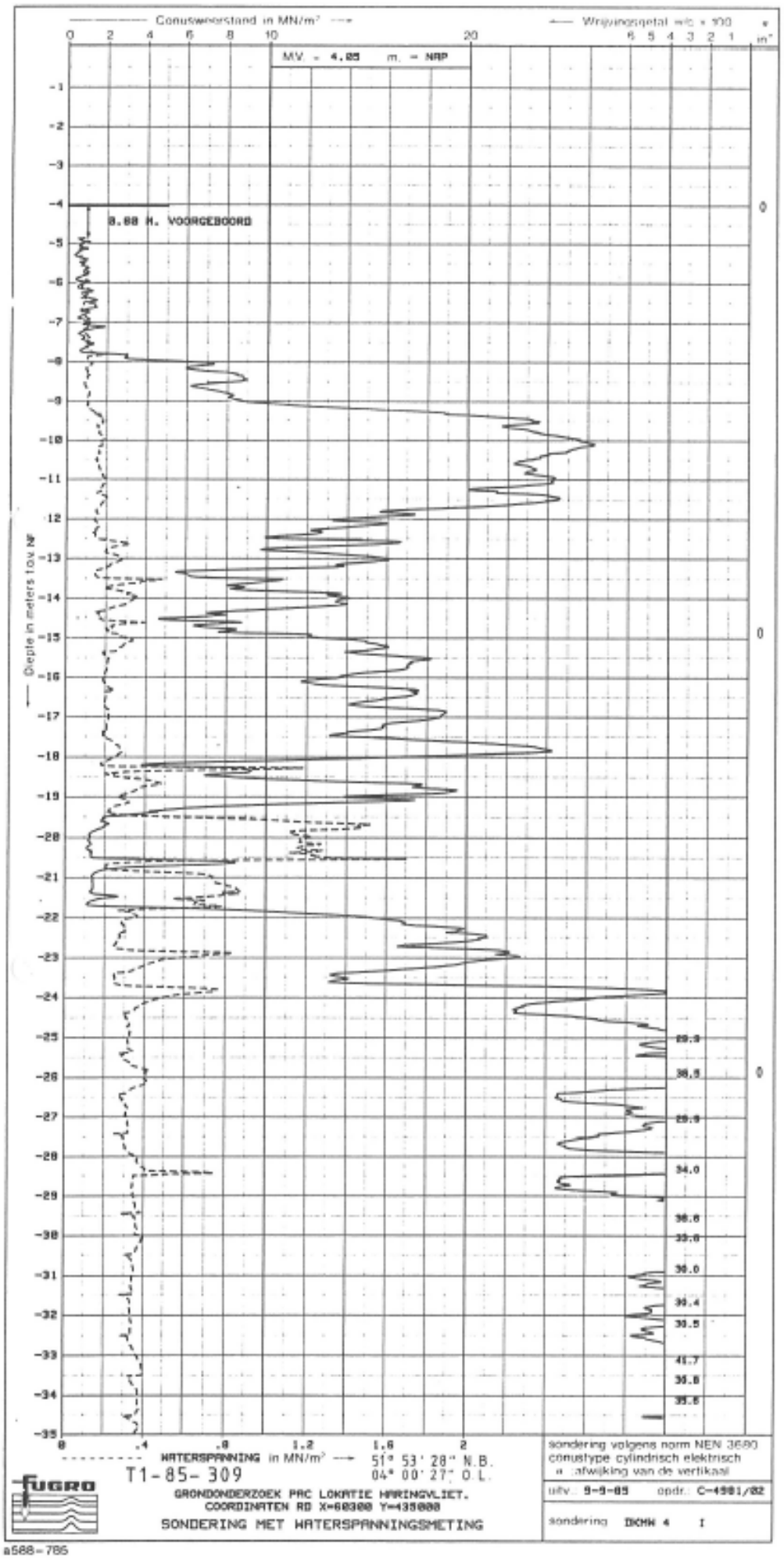

Figure E.6: CPT result from S36H00035-01

F

Soil Parameters

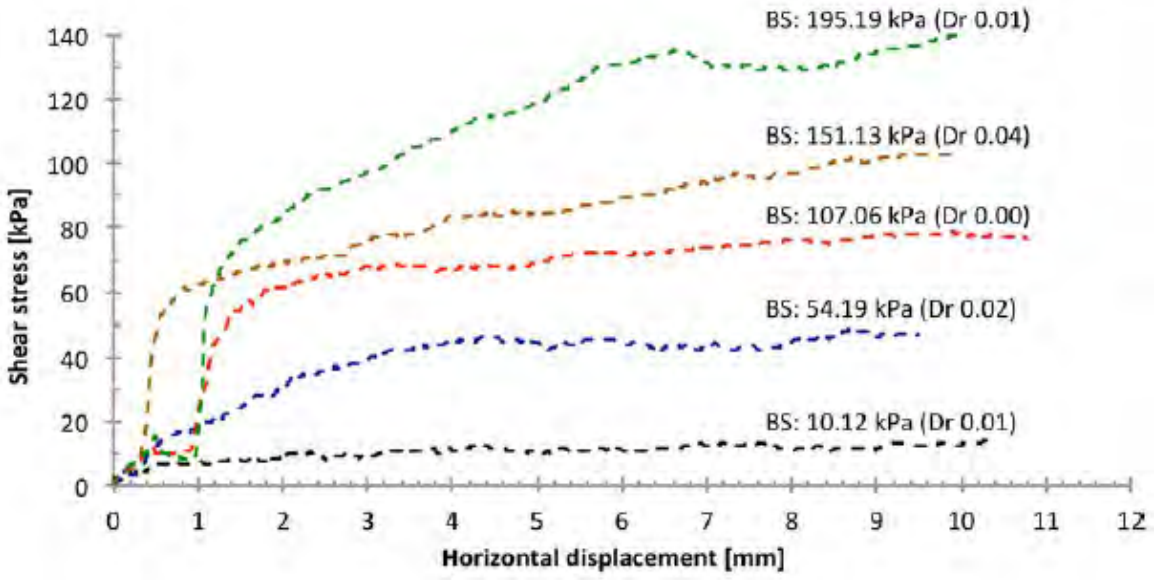

Figure F.1: Direct shear test results with loose samples of Geba sand from Krapfenbauer (2016)

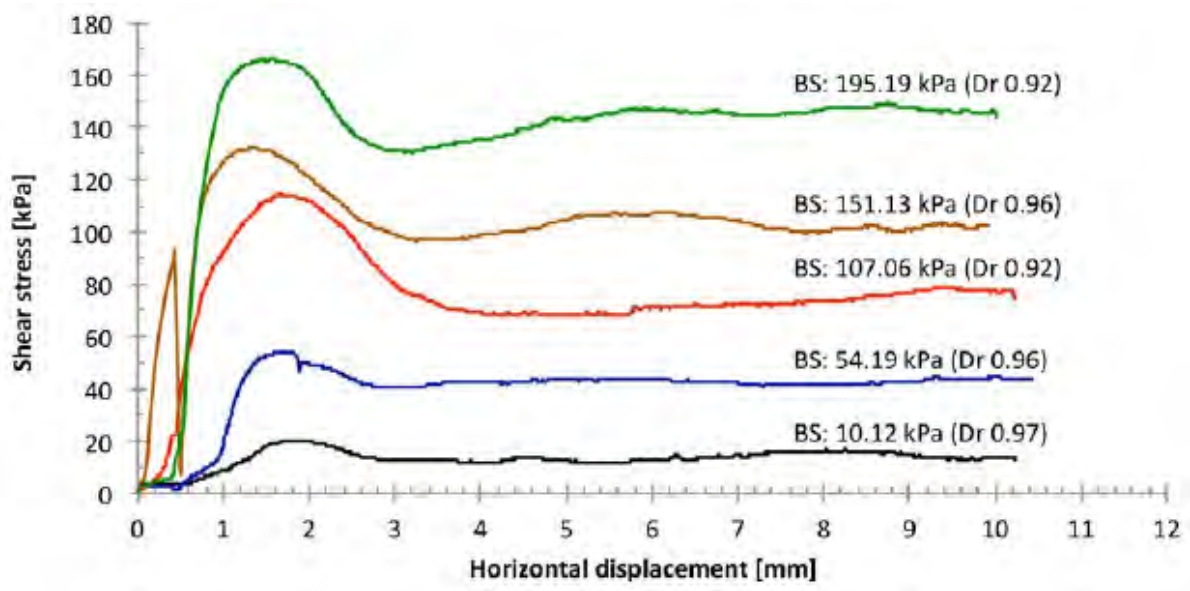

Figure F.2: Direct shear test results with dense samples of Geba sand from Krapfenbauer (2016)

G

photo's for PIV analysis

This chapter shows the first 41 pictures taken after drawdown of the rapid drawdown centrifuge test described in section 5.6. The pictures are taken every 0.2 seconds. Afterwards several pictures are presented on which the deformation is shown with help of PIV analysis.

G.0.1. pictures taken during drawdown

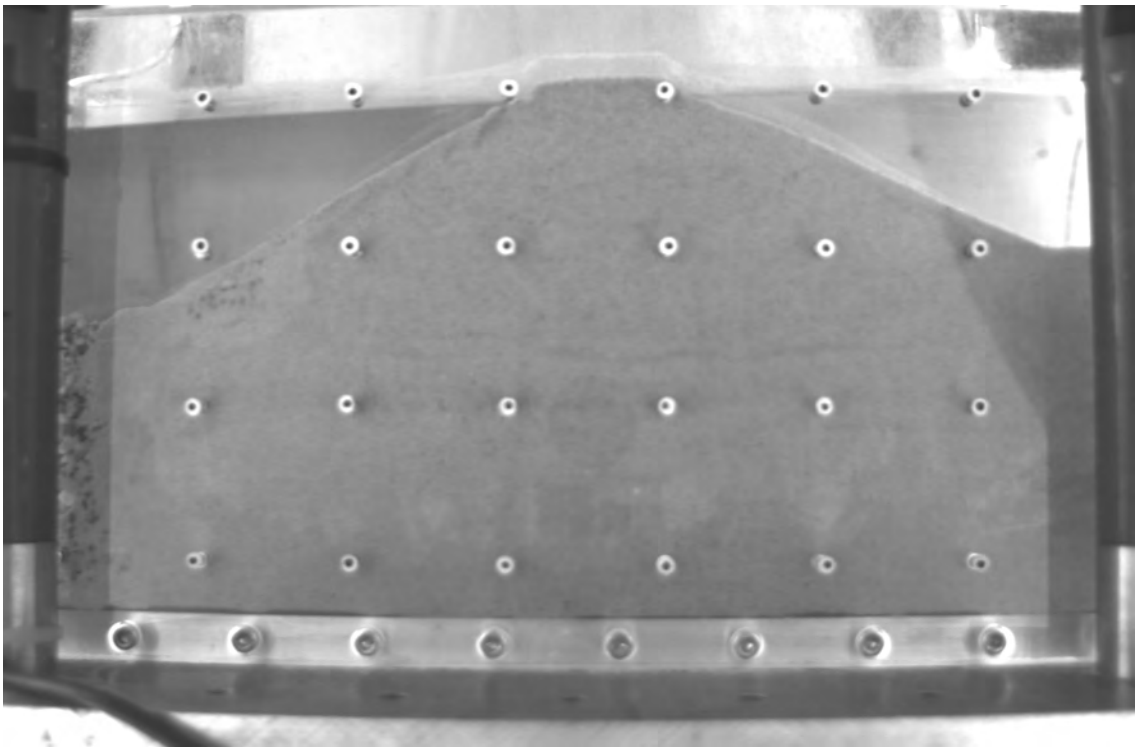

Figure G.1: Photo taken 0 seconds after start of rapid drawdown

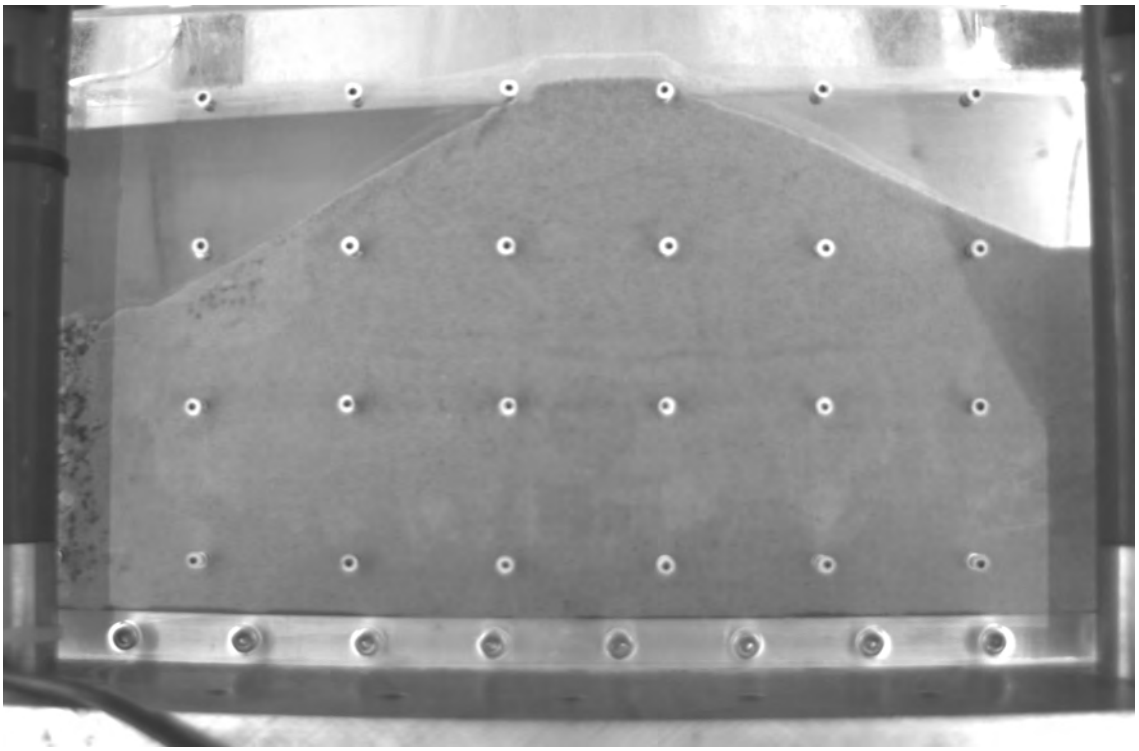

Figure G.2: Photo taken 0.2 seconds after start of rapid drawdown

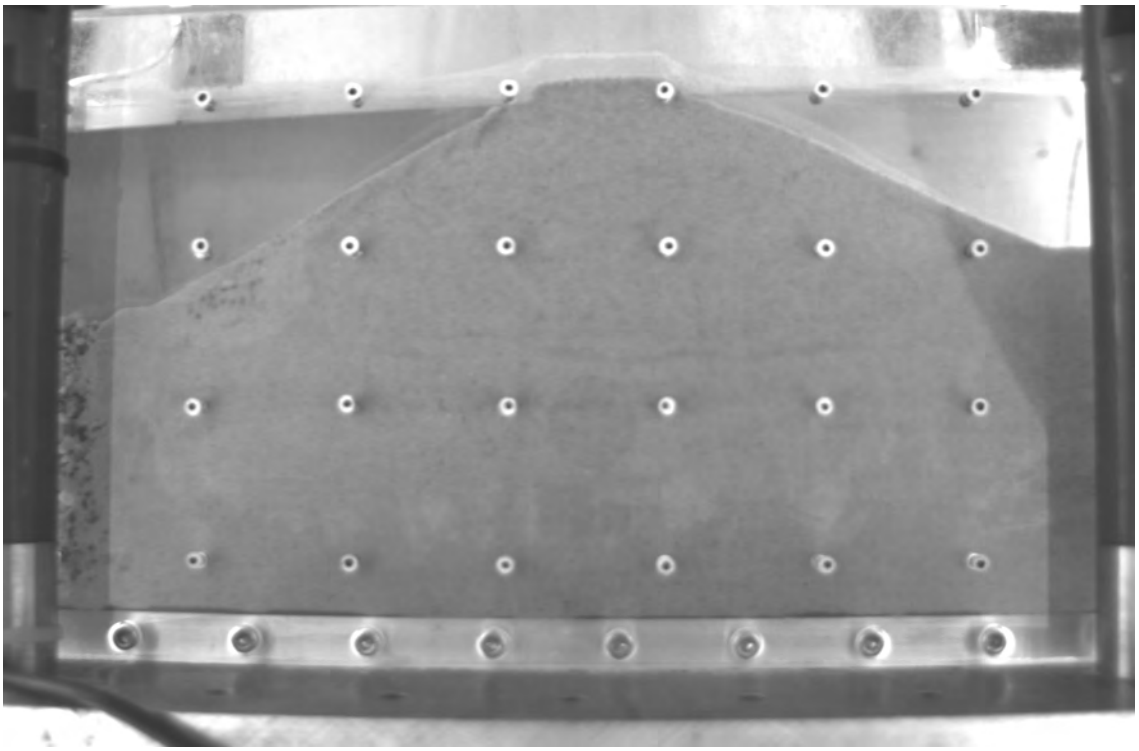

Figure G.3: Photo taken 0.4 seconds after start of rapid drawdown

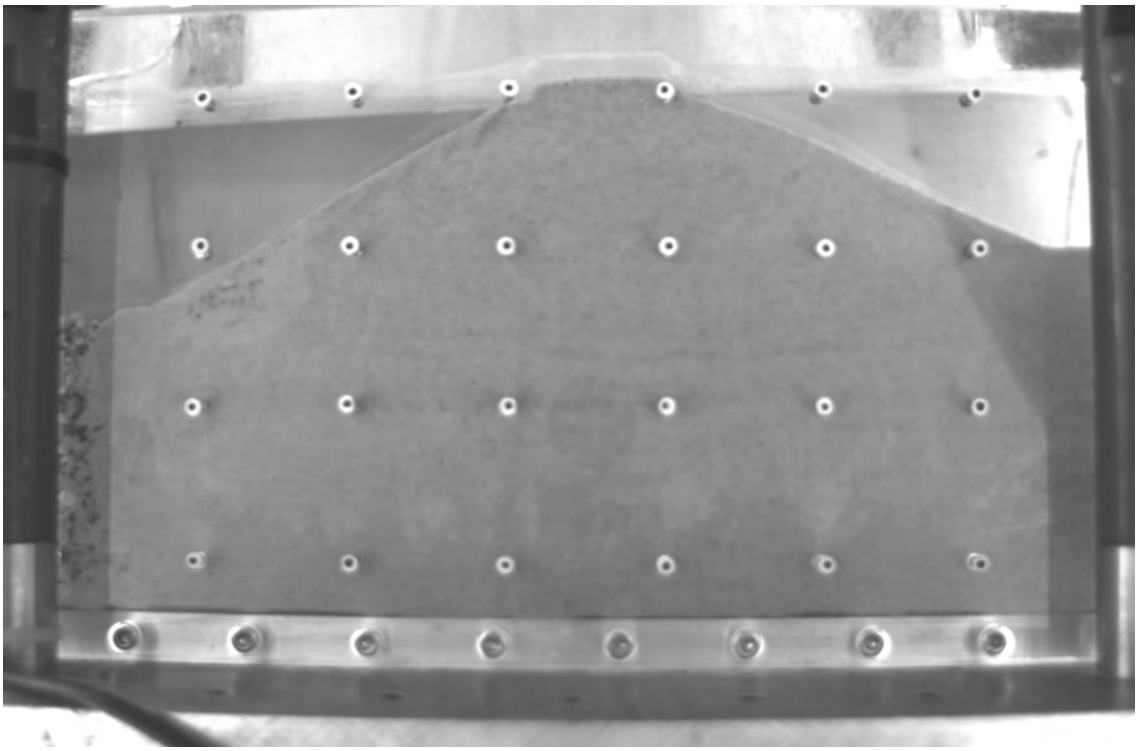

Figure G.4: Photo taken 0.6 seconds after start of rapid drawdown

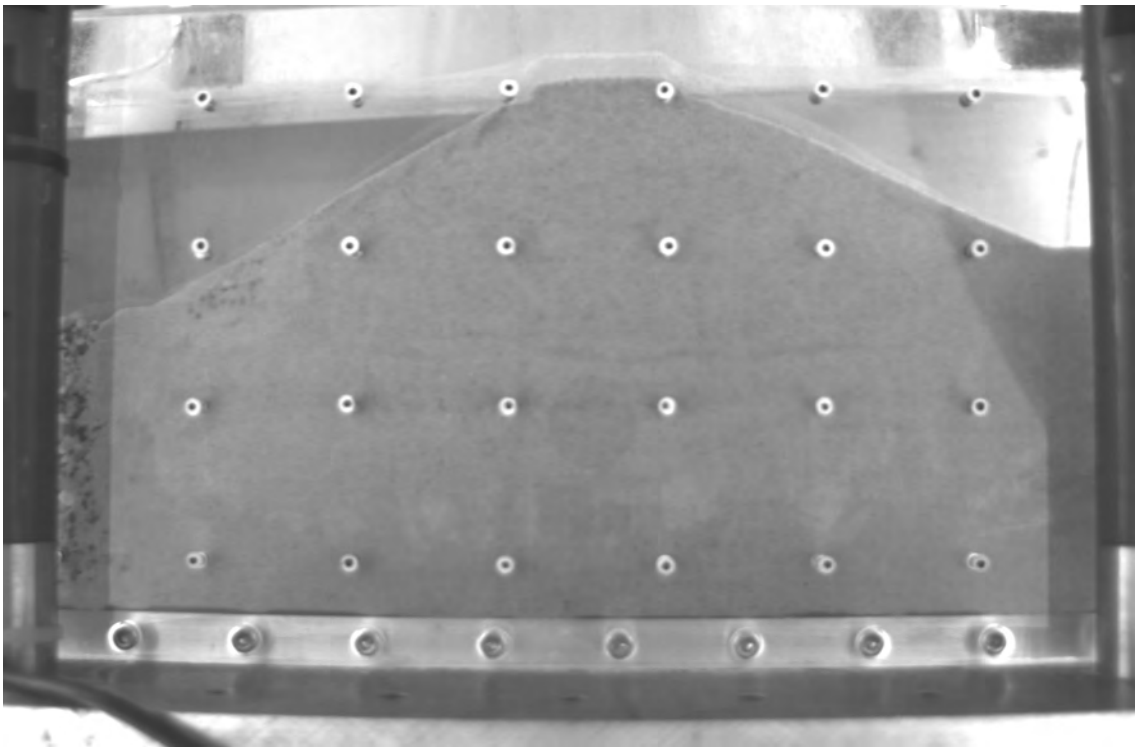

Figure G.5: Photo taken 0.8 seconds after start of rapid drawdown

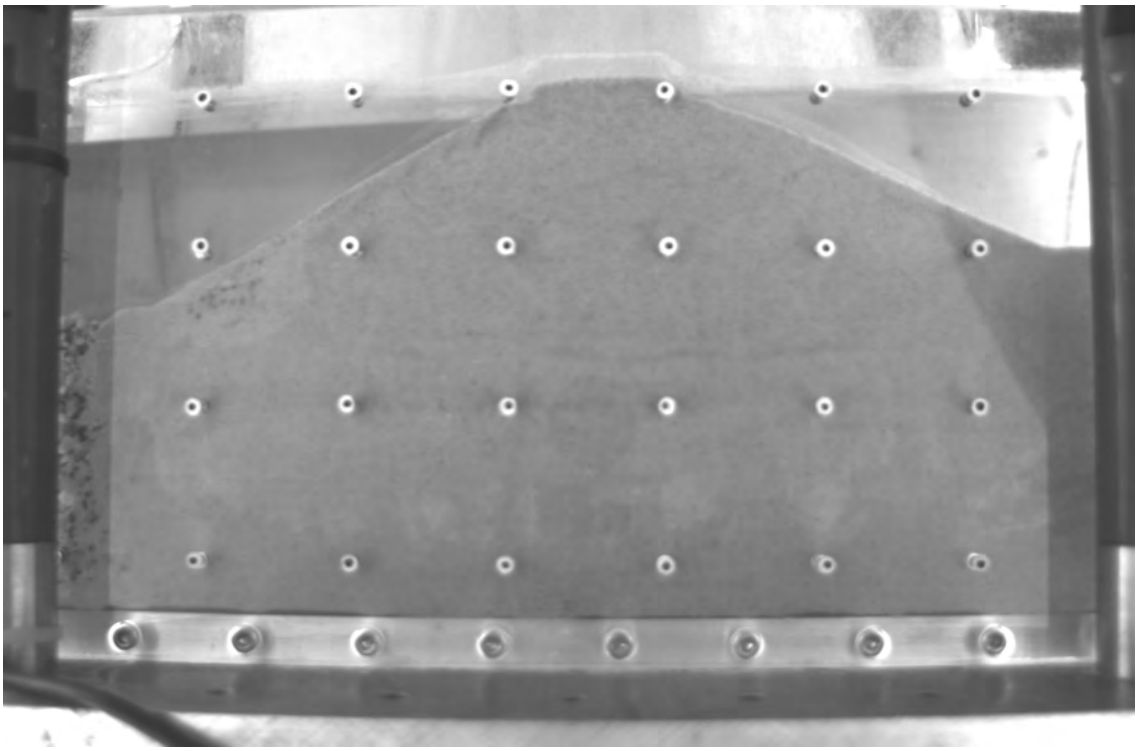

Figure G.6: Photo taken 1.0 seconds after start of rapid drawdown

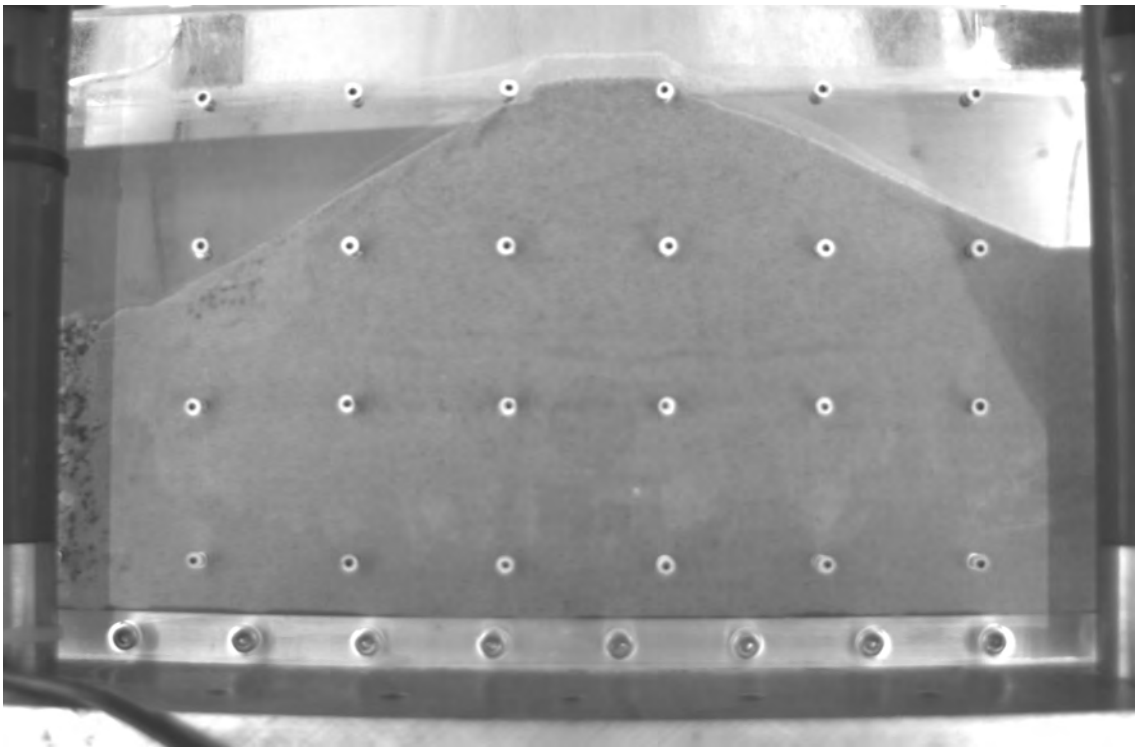

Figure G.7: Photo taken 1.2 seconds after start of rapid drawdown

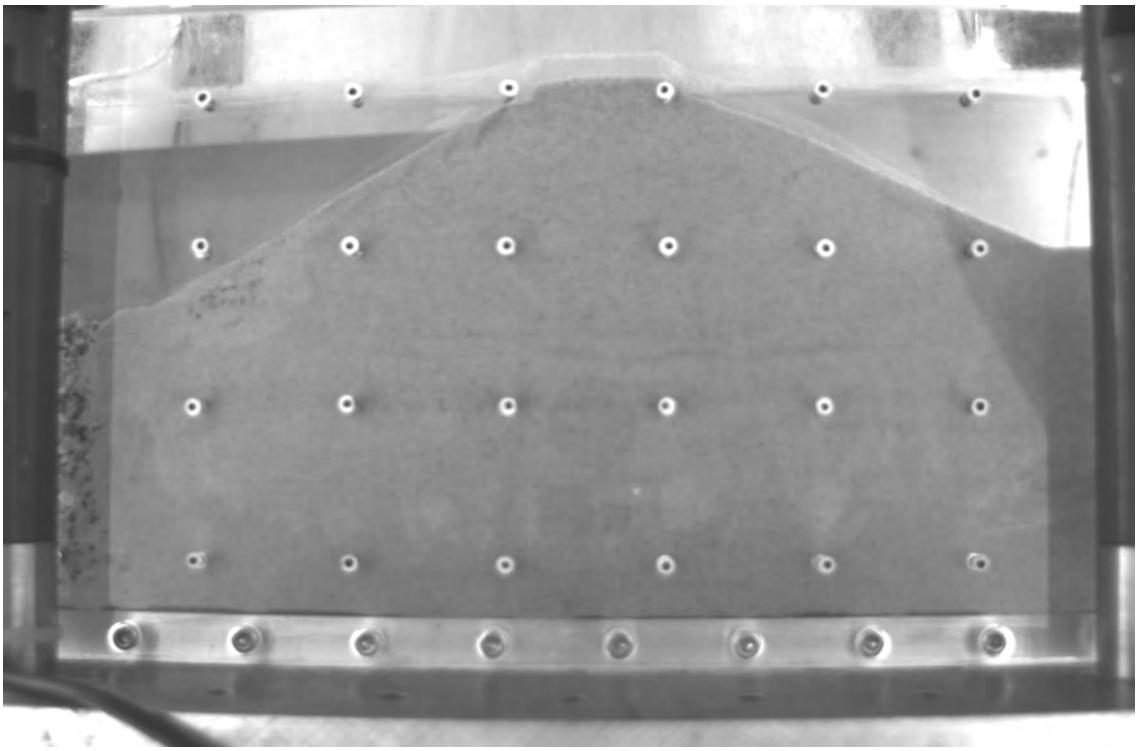

Figure G.8: Photo taken 1.4 seconds after start of rapid drawdown

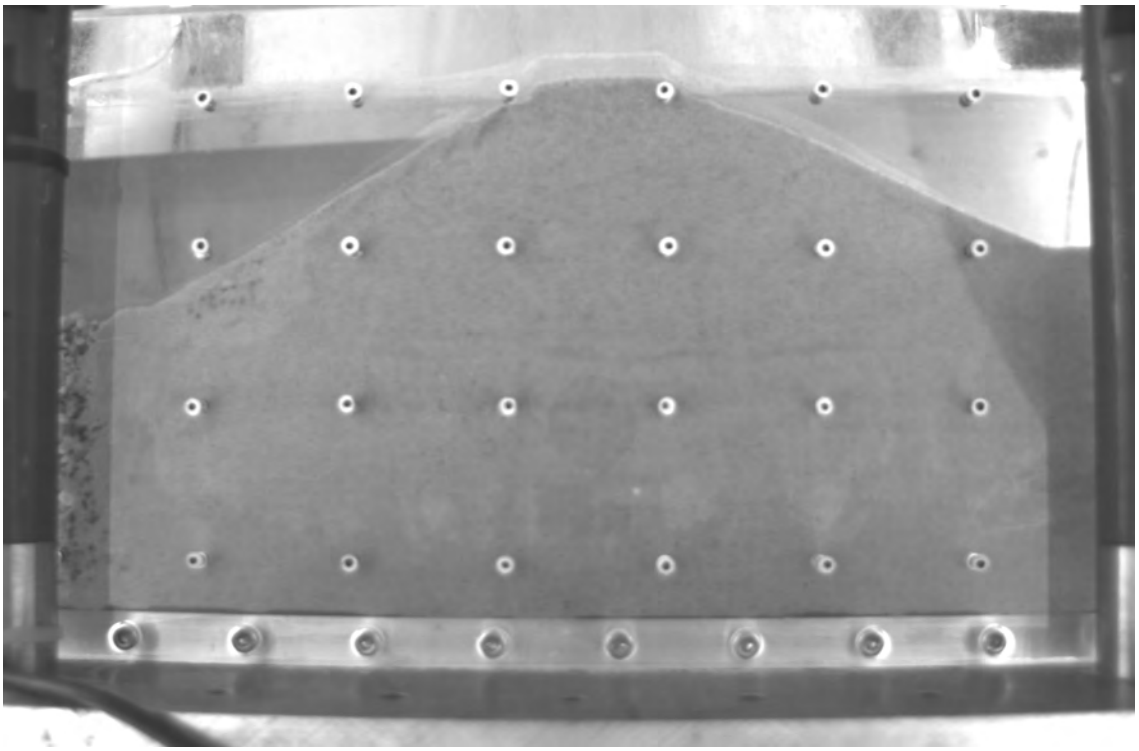

Figure G.9: Photo taken 1.6 seconds after start of rapid drawdown

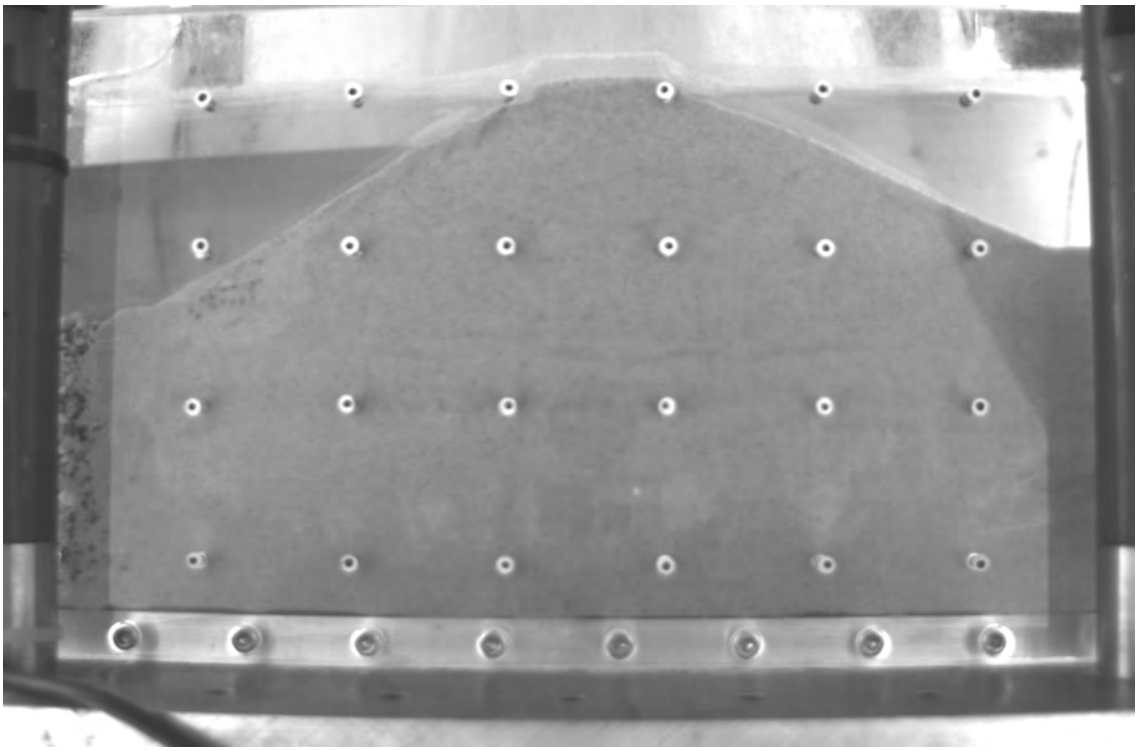

Figure G.10: Photo taken 1.8 seconds after start of rapid drawdown

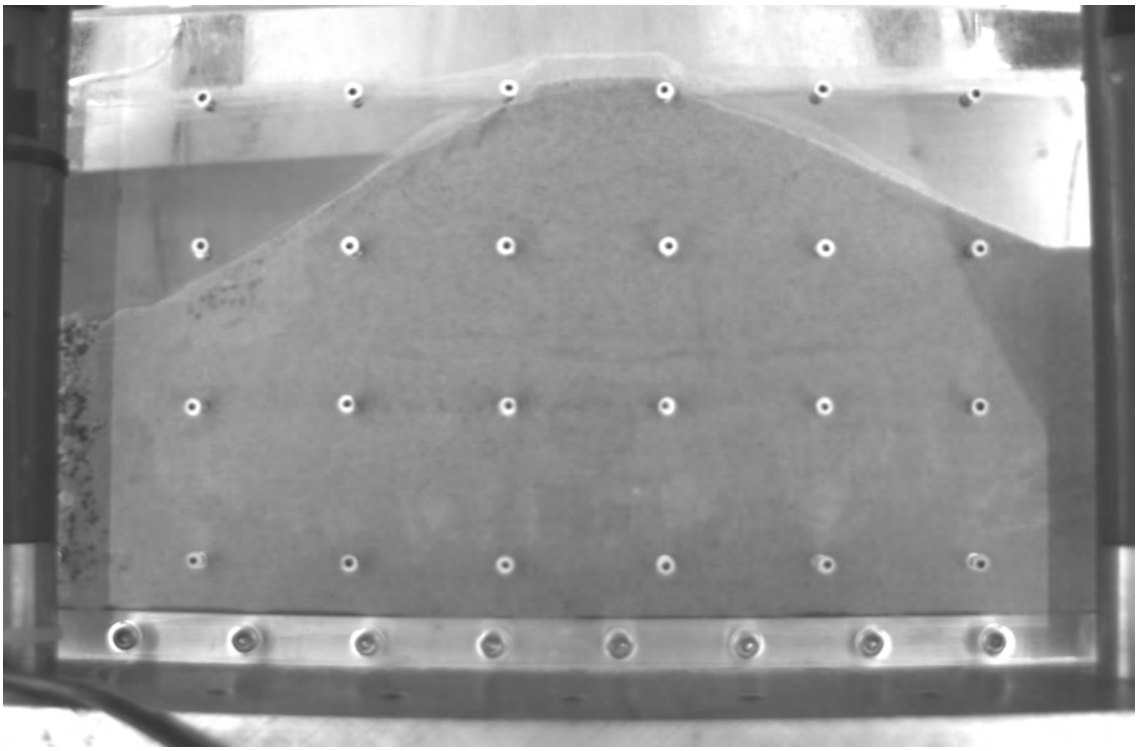

Figure G.11: Photo taken 2.0 seconds after start of rapid drawdown

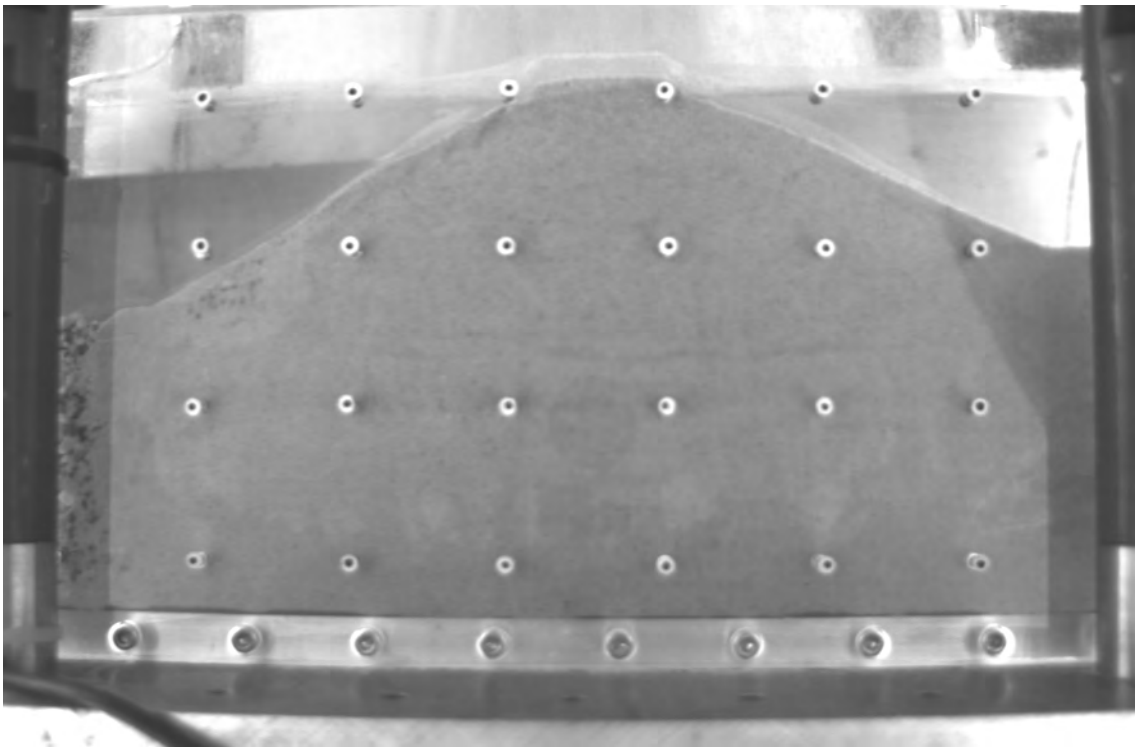

Figure G.12: Photo taken 2.2 seconds after start of rapid drawdown

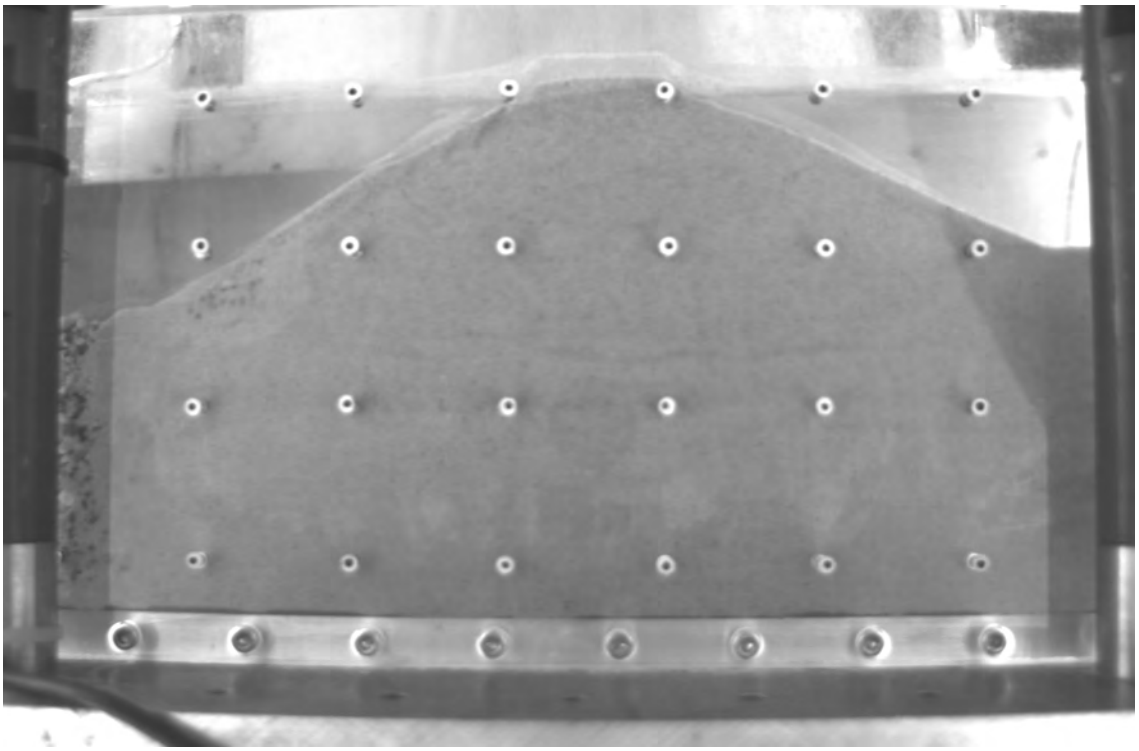

Figure G.13: Photo taken 2.4 seconds after start of rapid drawdown

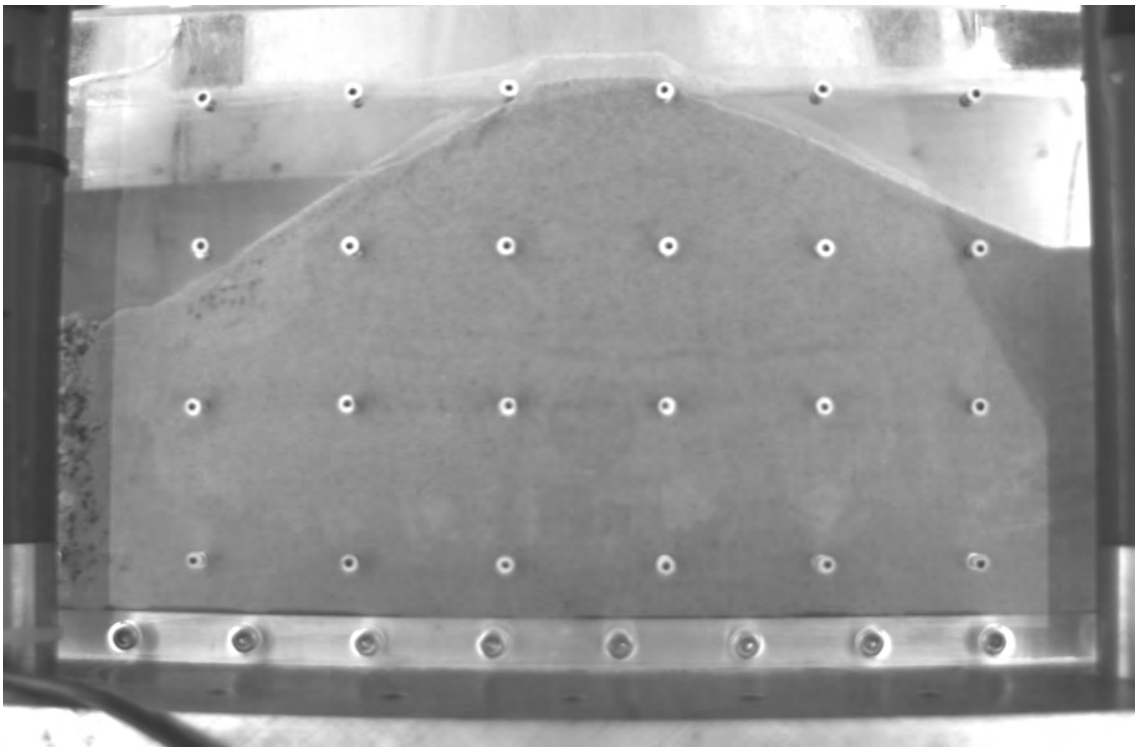

Figure G.14: Photo taken 2.6 seconds after start of rapid drawdown

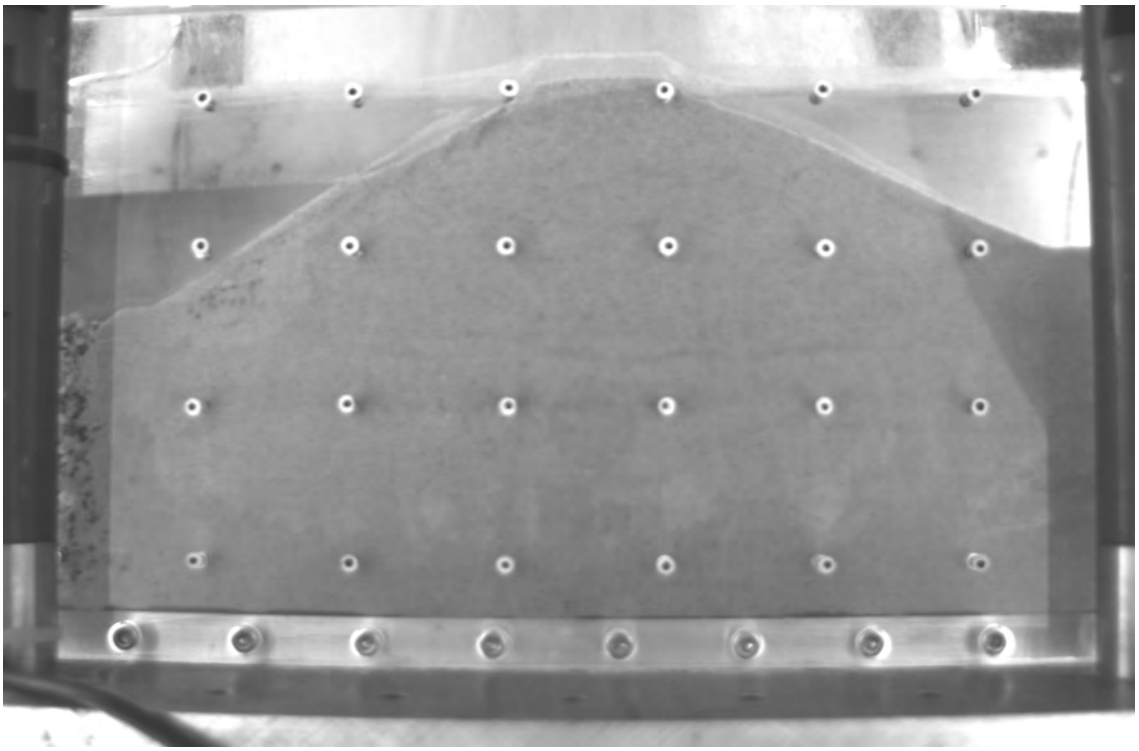

Figure G.15: Photo taken 2.8 seconds after start of rapid drawdown

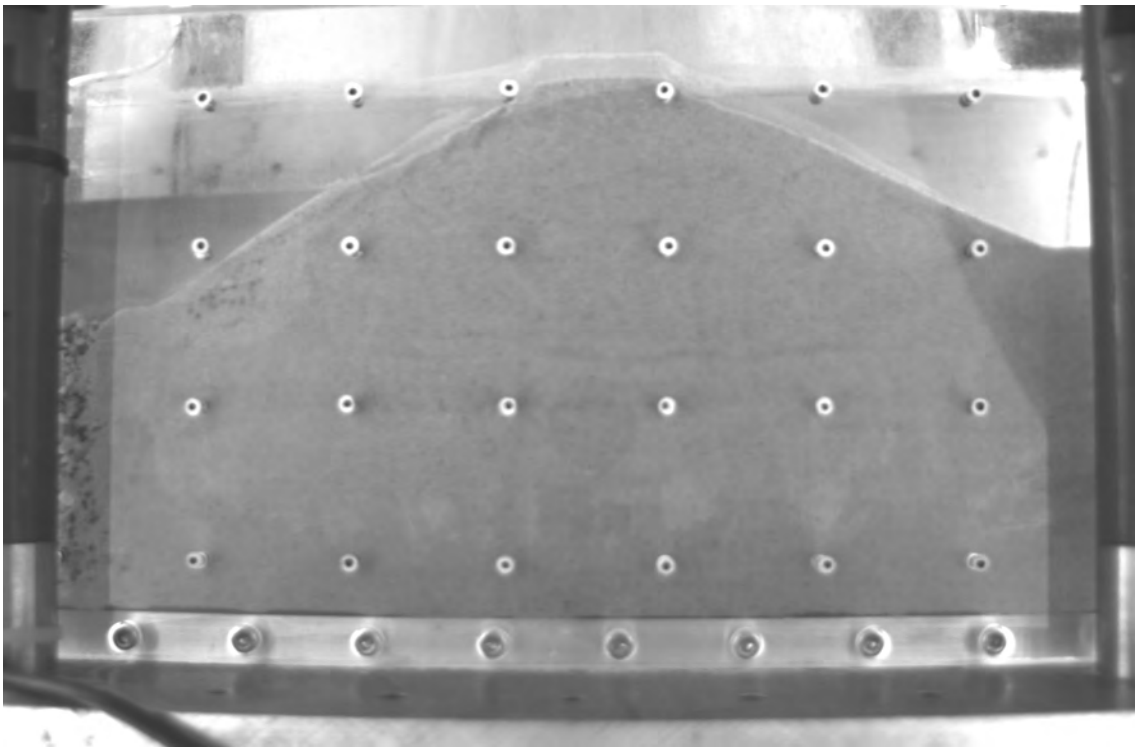

Figure G.16: Photo taken 3.0 seconds after start of rapid drawdown

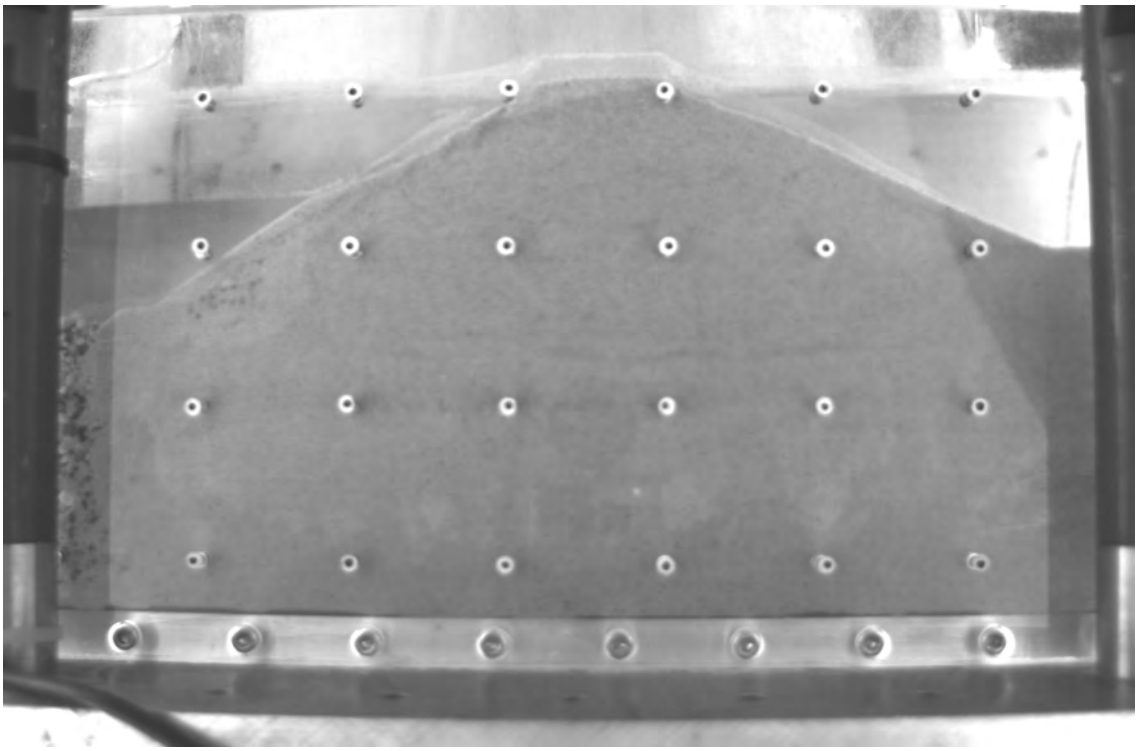

Figure G.17: Photo taken 3.2 seconds after start of rapid drawdown

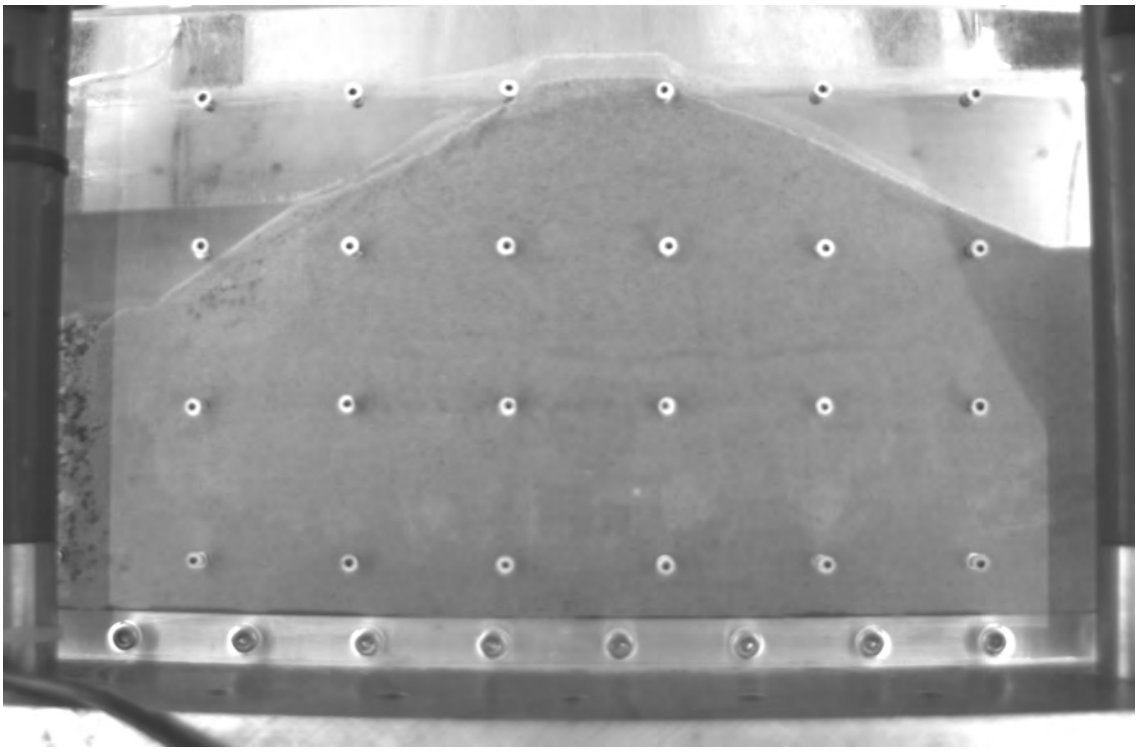

Figure G.18: Photo taken 3.4 seconds after start of rapid drawdown

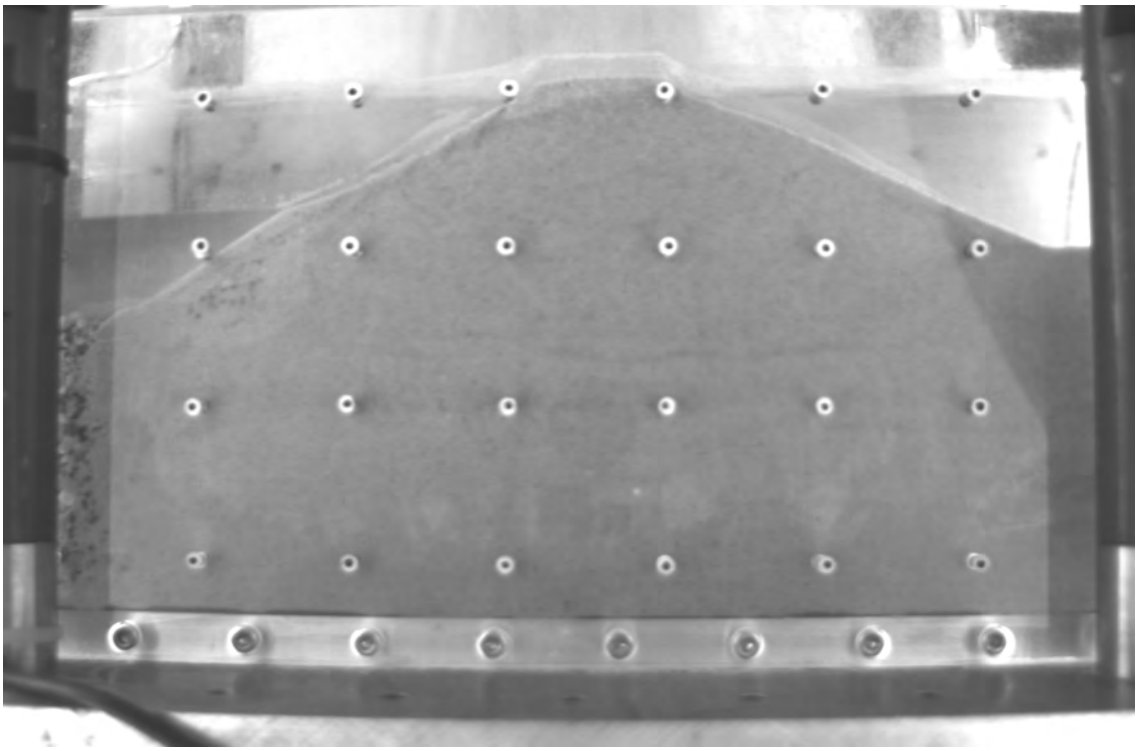

Figure G.19: Photo taken 3.6 seconds after start of rapid drawdown

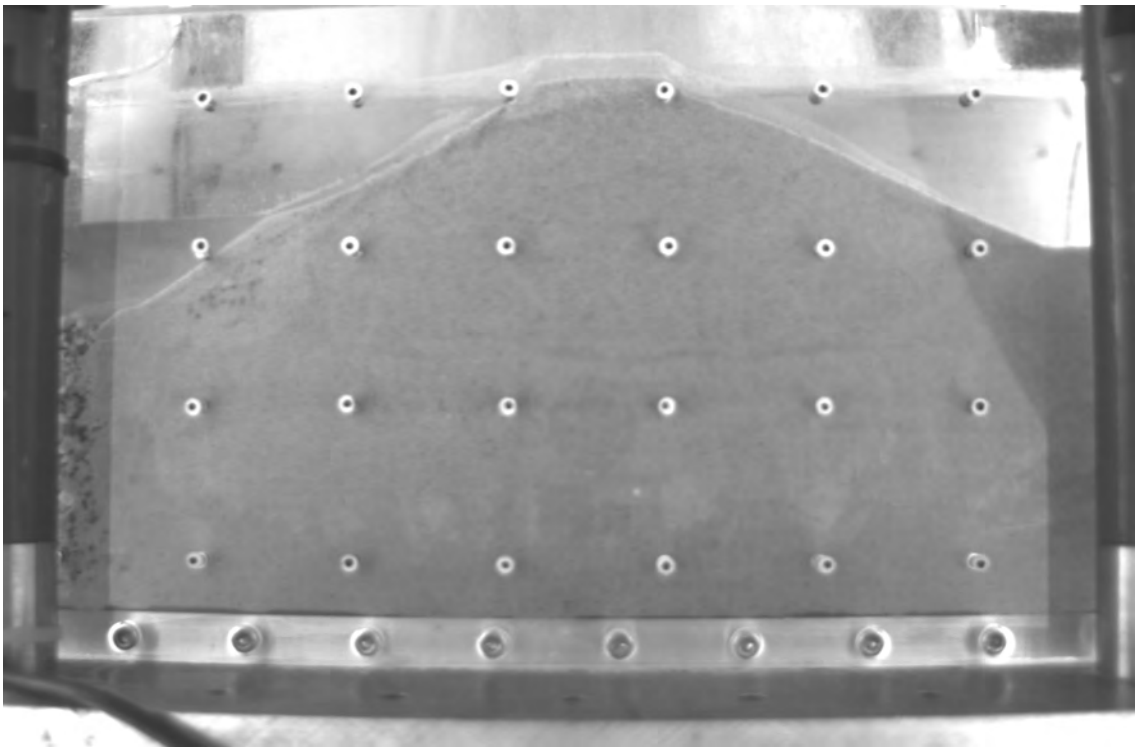

Figure G.20: Photo taken 3.8 seconds after start of rapid drawdown

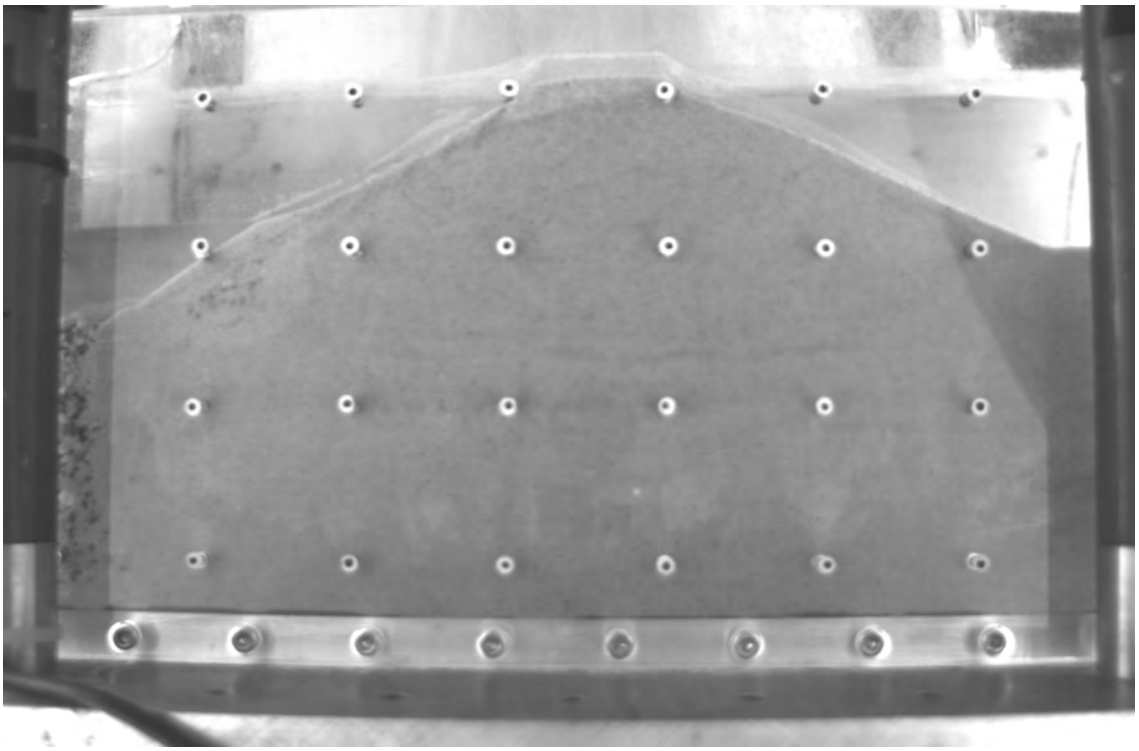

Figure G.21: Photo taken 4.0 seconds after start of rapid drawdown

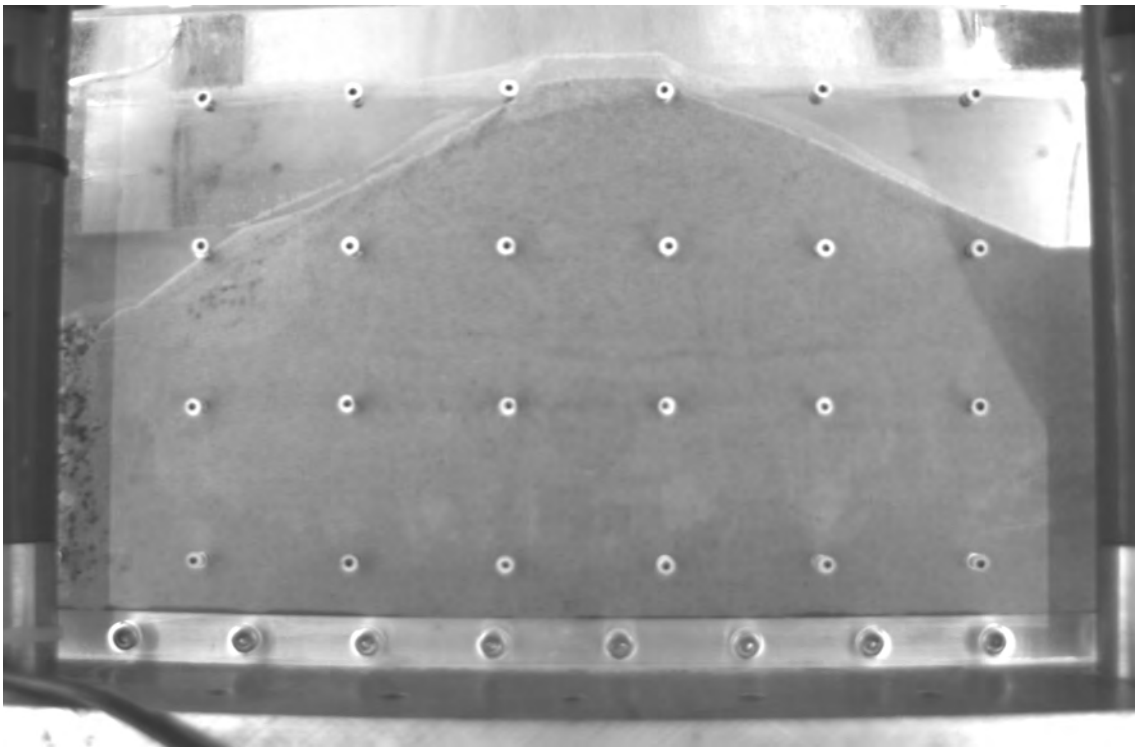

Figure G.22: Photo taken 4.2 seconds after start of rapid drawdown

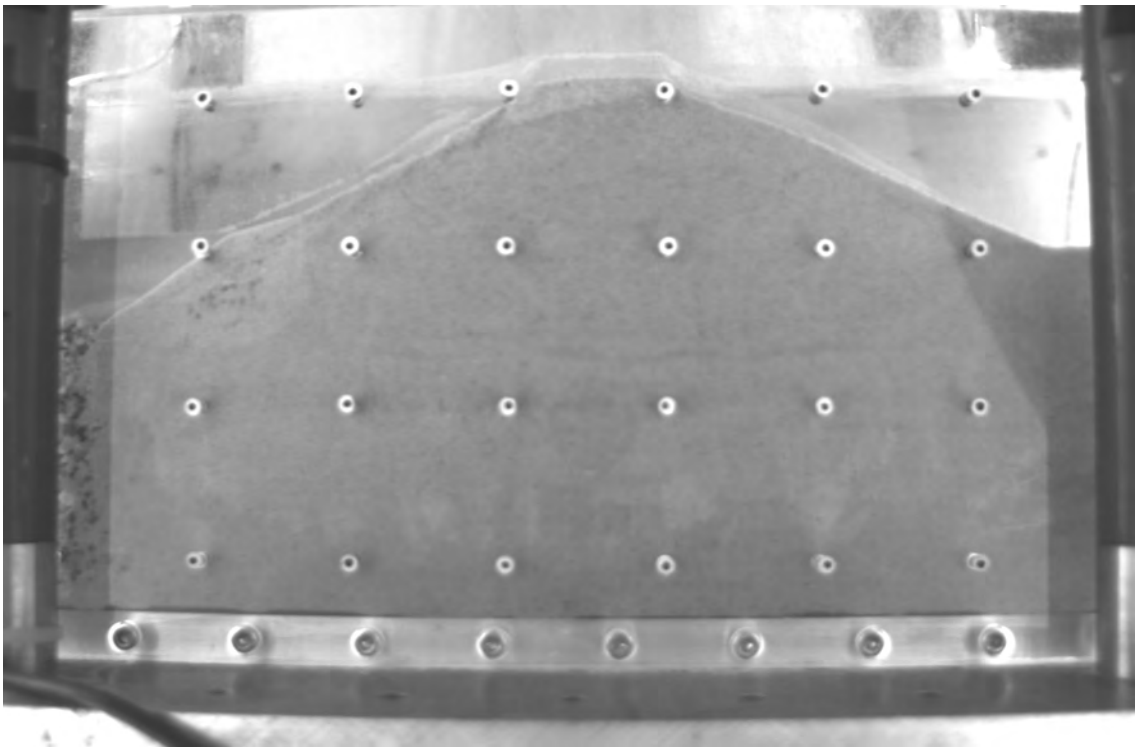

Figure G.23: Photo taken 4.4 seconds after start of rapid drawdown

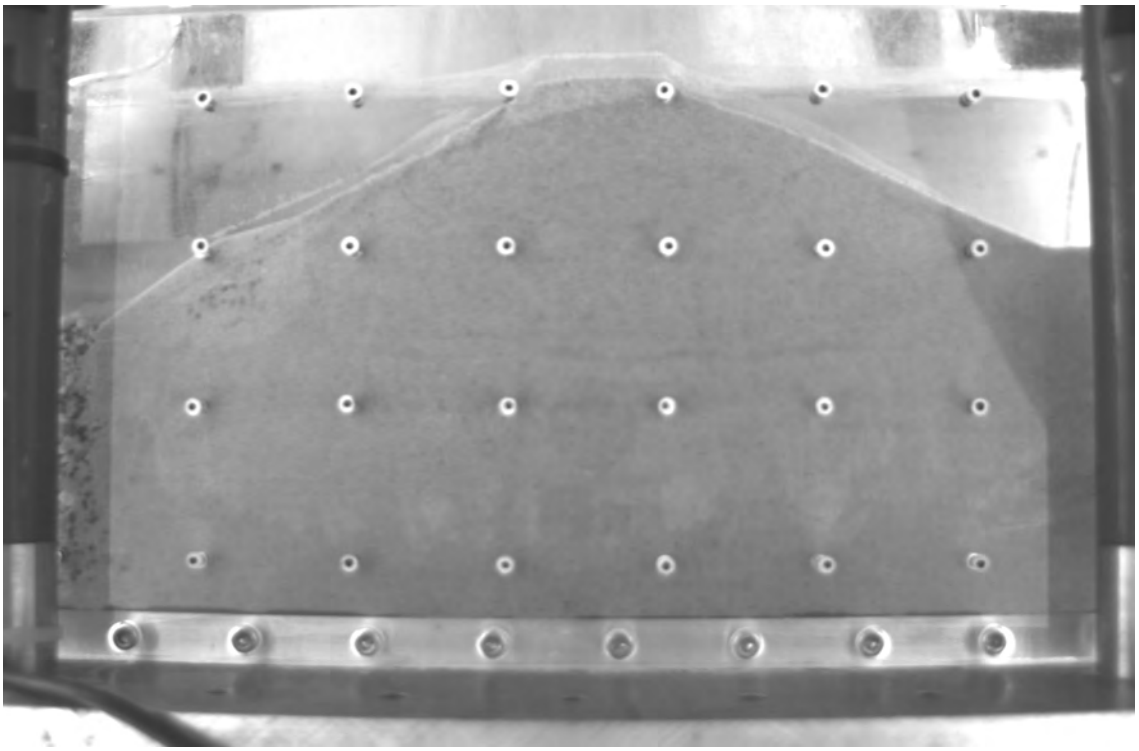

Figure G.24: Photo taken 4.6 seconds after start of rapid drawdown

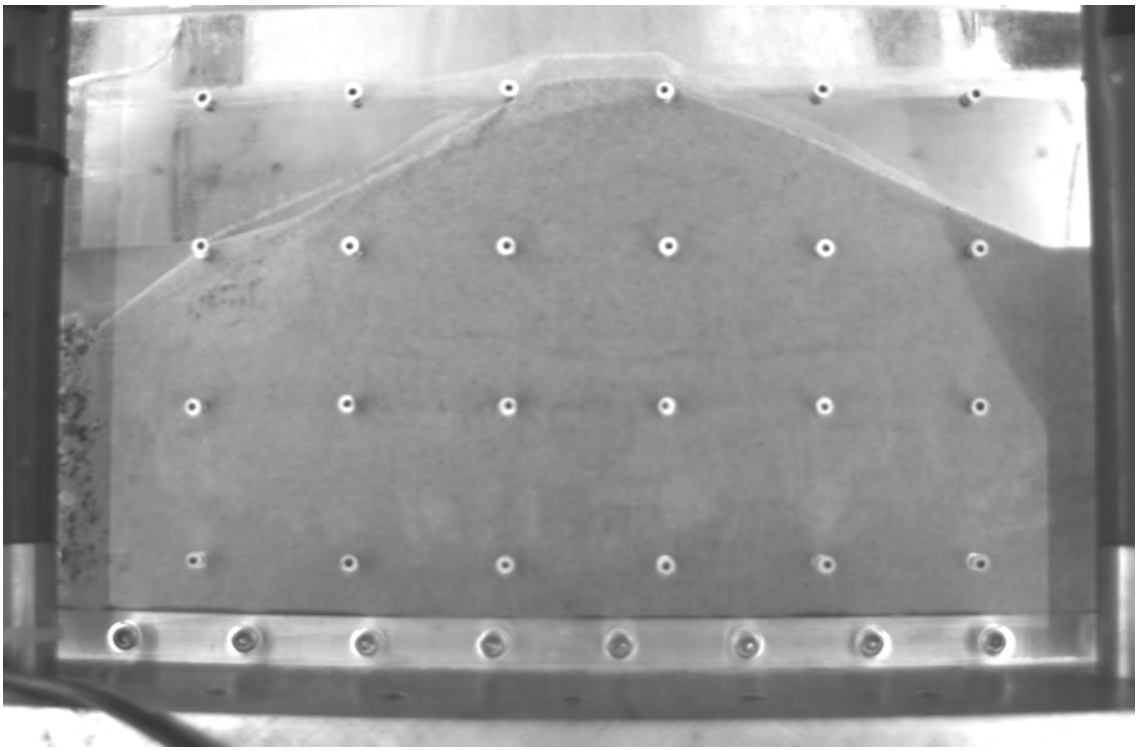

Figure G.25: Photo taken 4.8 seconds after start of rapid drawdown

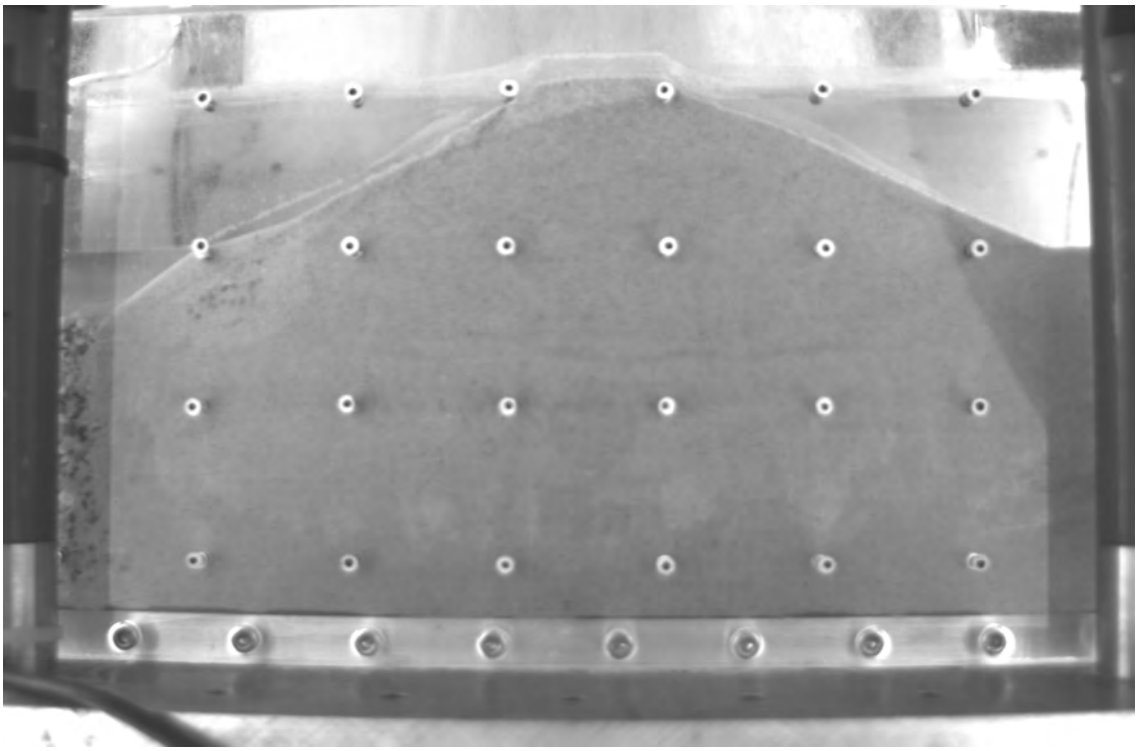

Figure G.26: Photo taken 5.0 seconds after start of rapid drawdown

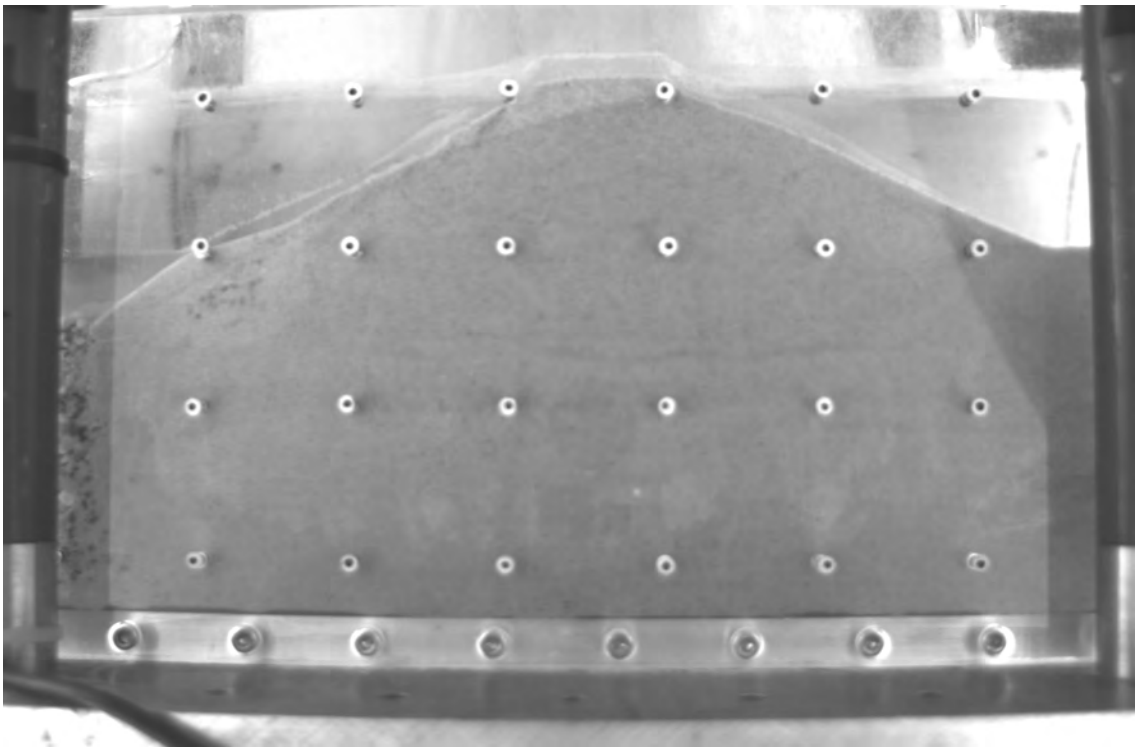

Figure G.27: Photo taken 5.2 seconds after start of rapid drawdown

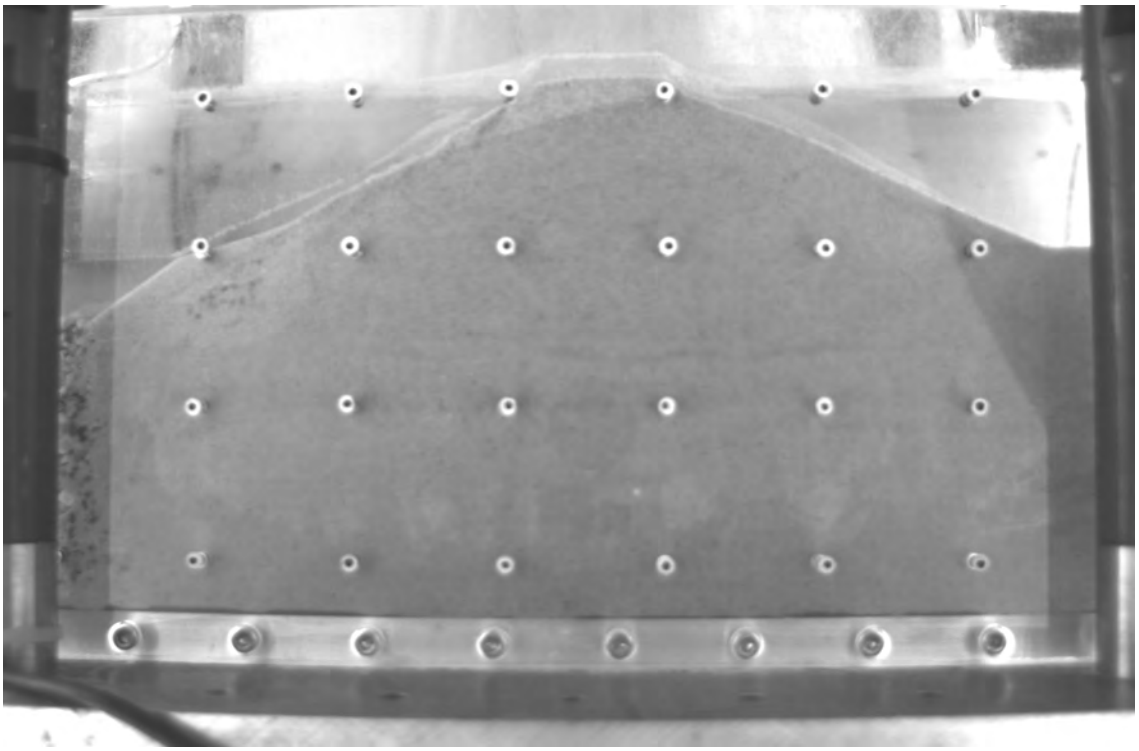

Figure G.28: Photo taken 5.4 seconds after start of rapid drawdown

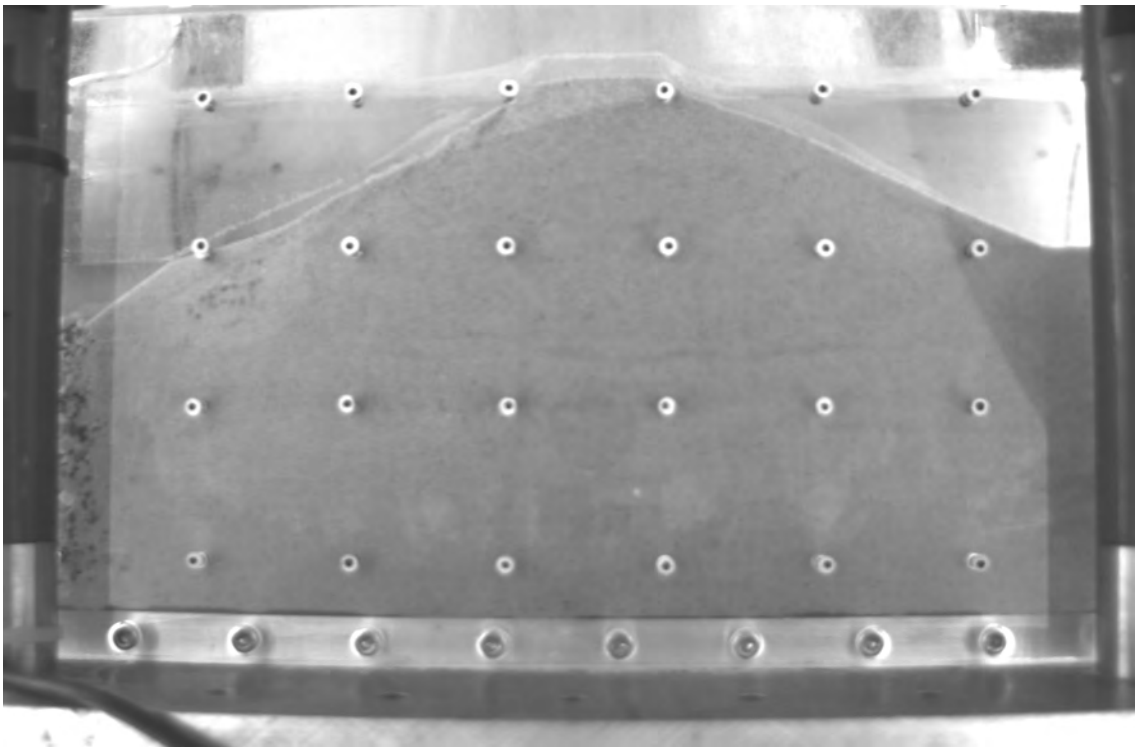

Figure G.29: Photo taken 5.6 seconds after start of rapid drawdown

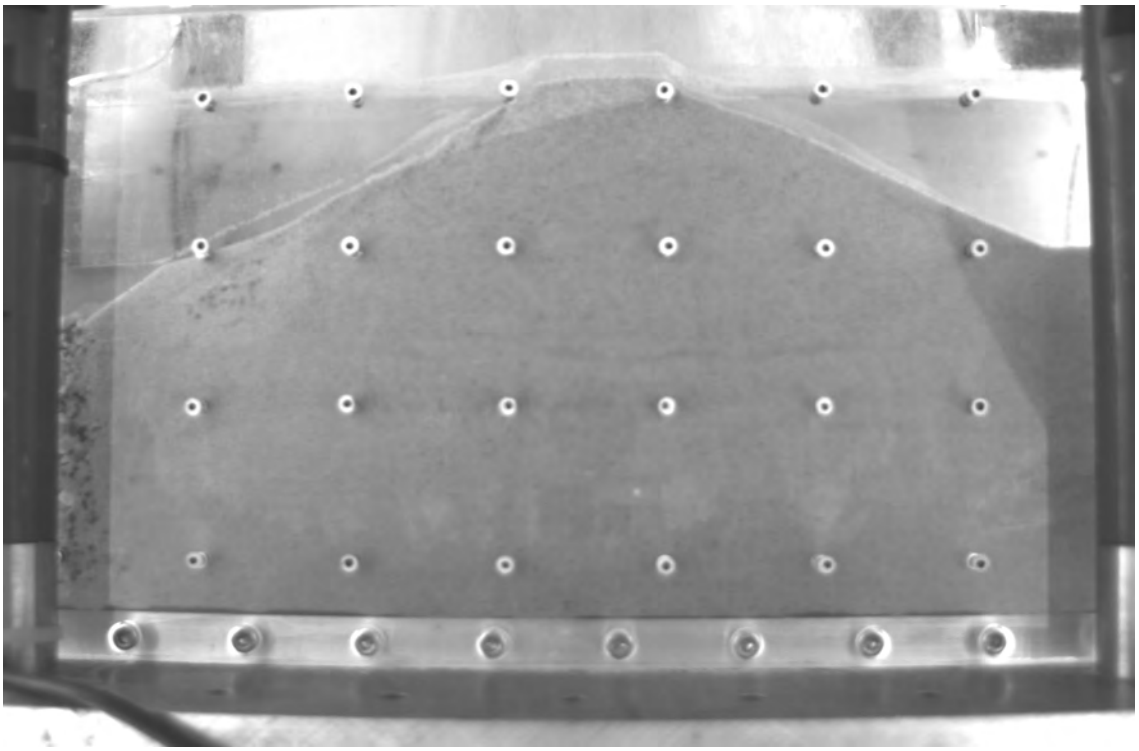

Figure G.30: Photo taken 5.8 seconds after start of rapid drawdown

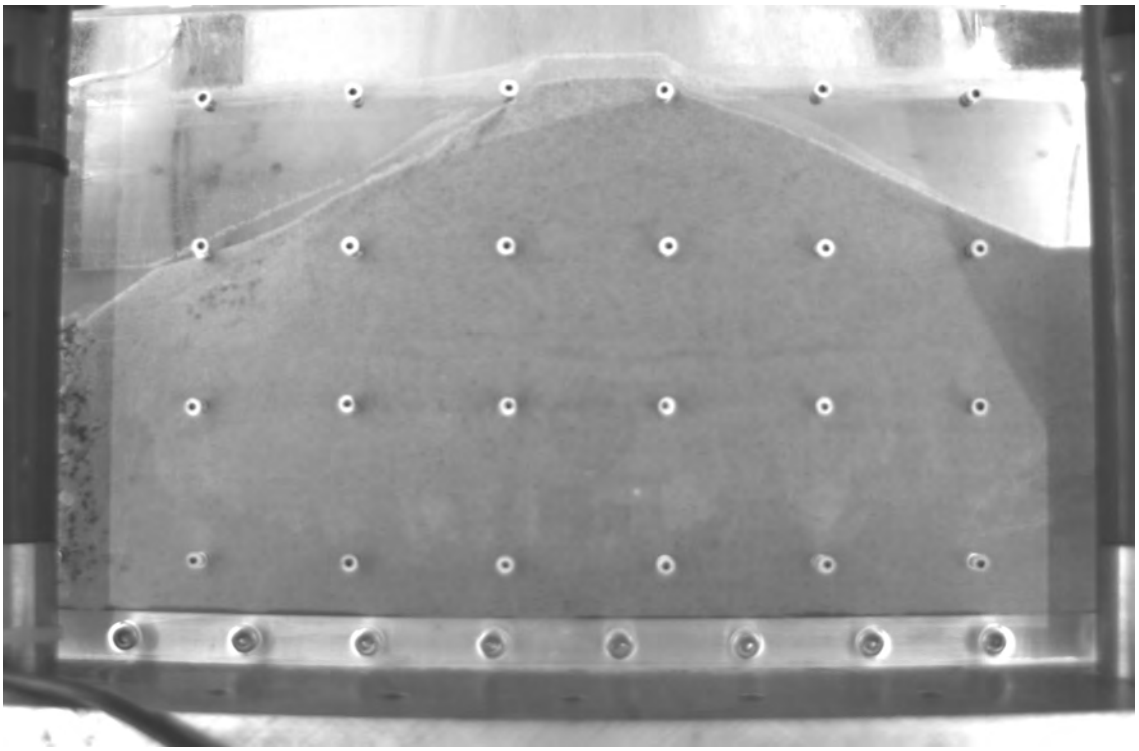

Figure G.31: Photo taken 6.0 seconds after start of rapid drawdown

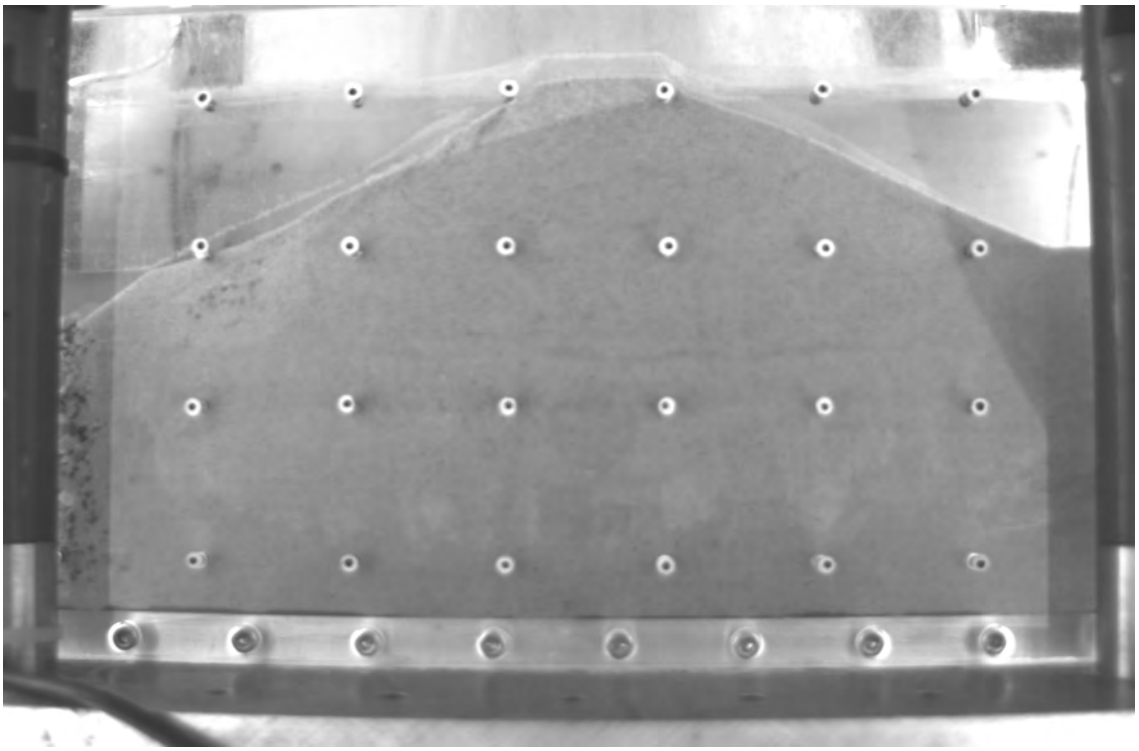

Figure G.32: Photo taken 6.2 seconds after start of rapid drawdown

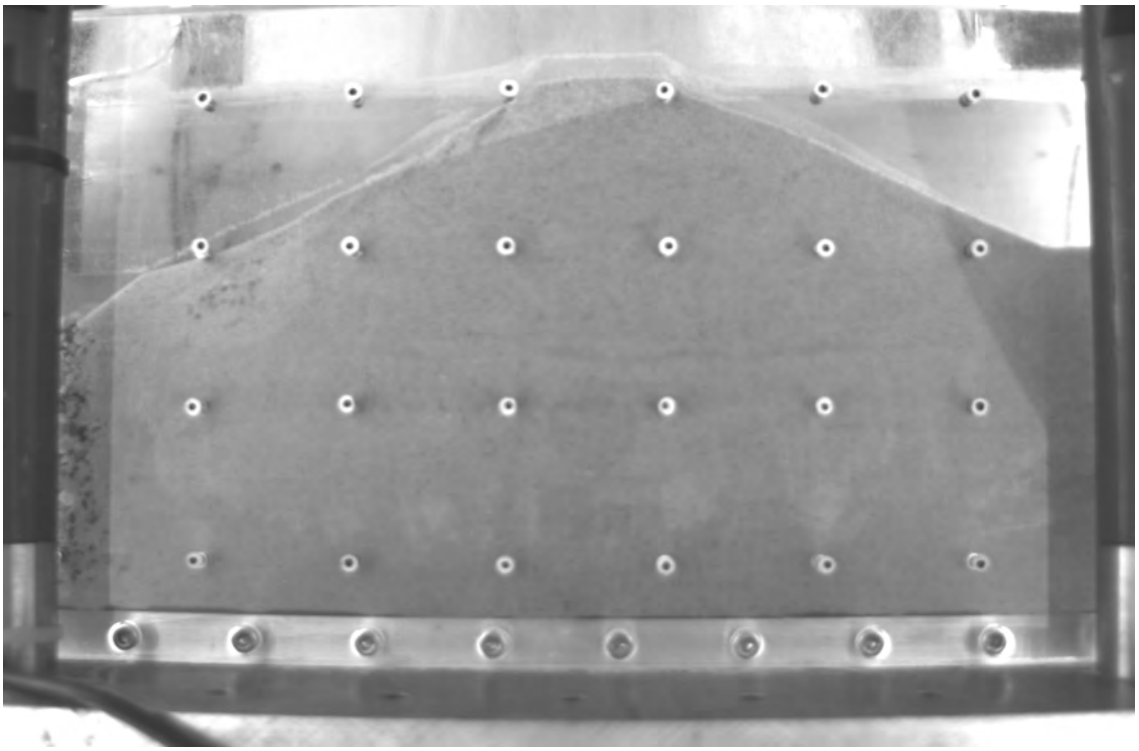

Figure G.33: Photo taken 6.4 seconds after start of rapid drawdown

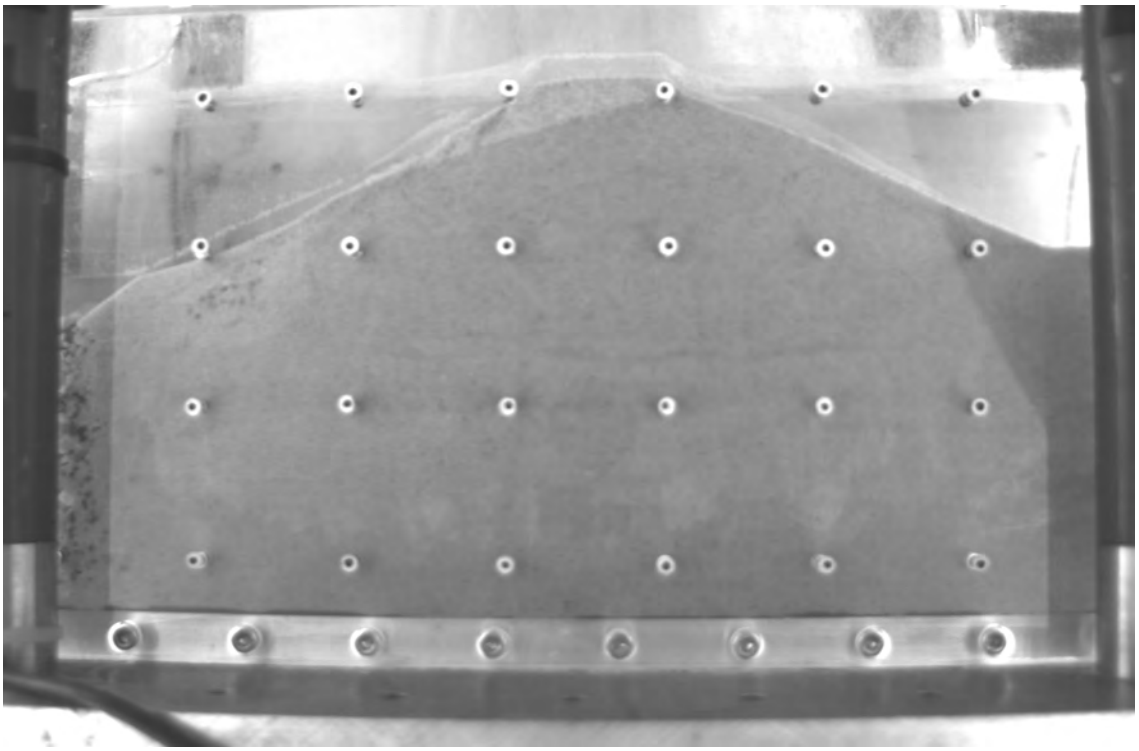

Figure G.34: Photo taken 6.6 seconds after start of rapid drawdown

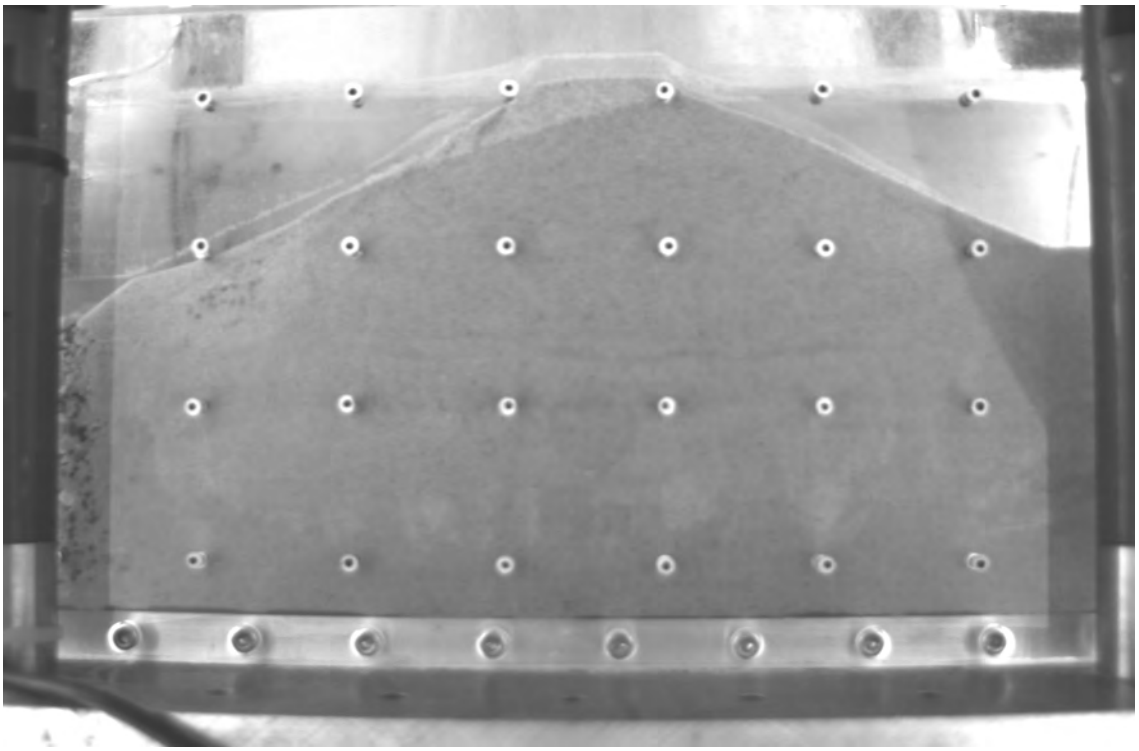

Figure G.35: Photo taken 6.8 seconds after start of rapid drawdown

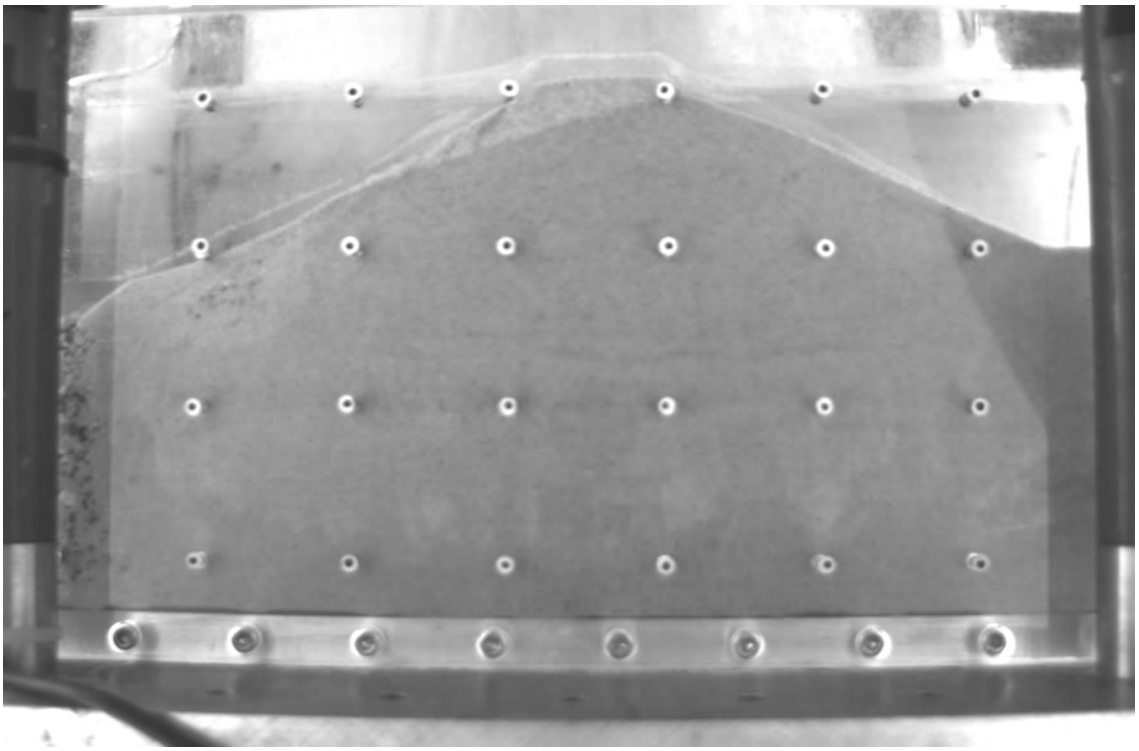

Figure G.36: Photo taken 7.0 seconds after start of rapid drawdown

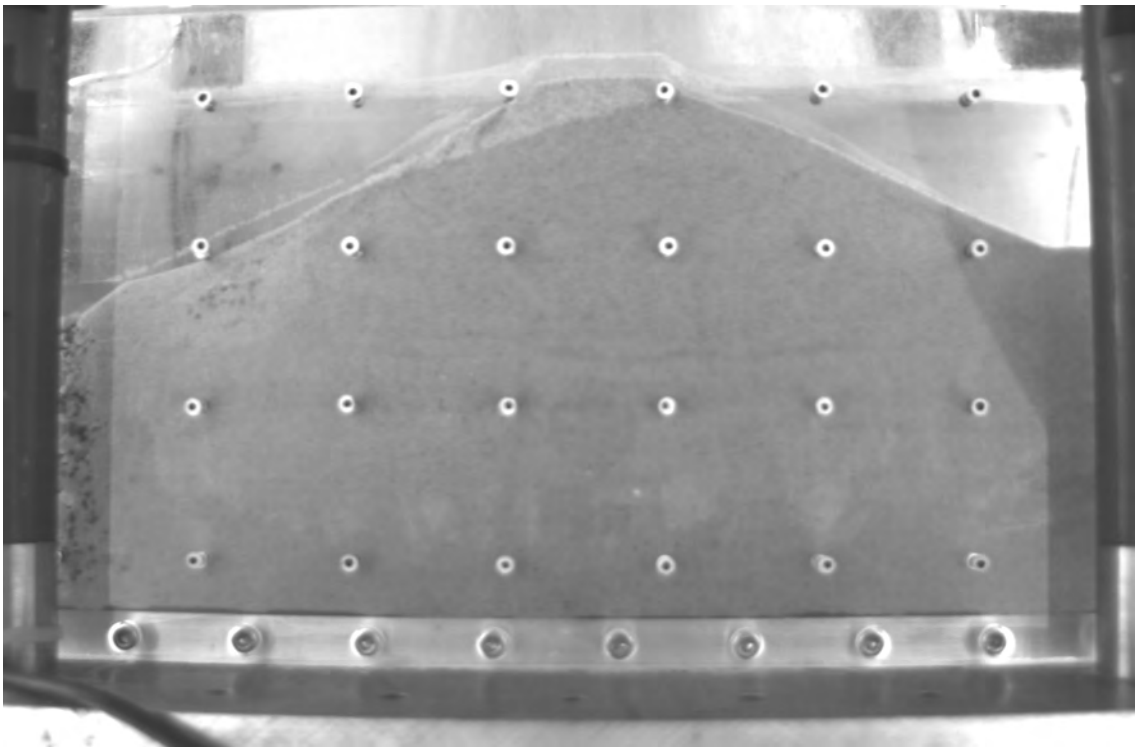

Figure G.37: Photo taken 7.2 seconds after start of rapid drawdown

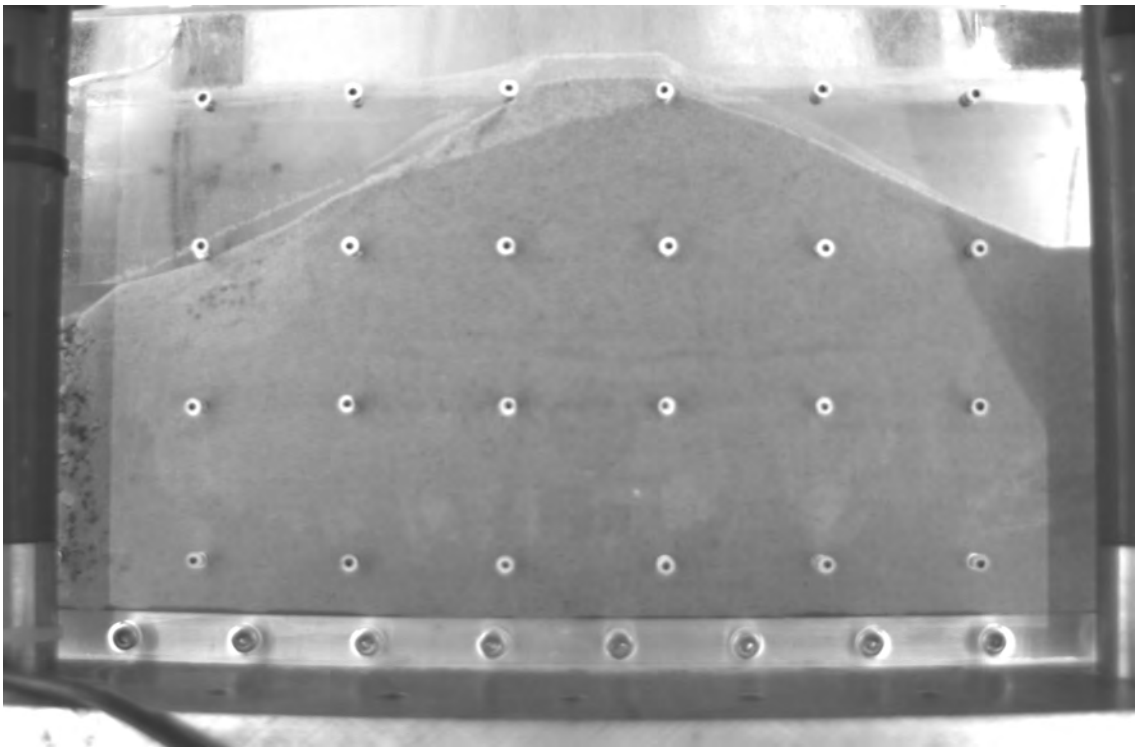

Figure G.38: Photo taken 7.4 seconds after start of rapid drawdown

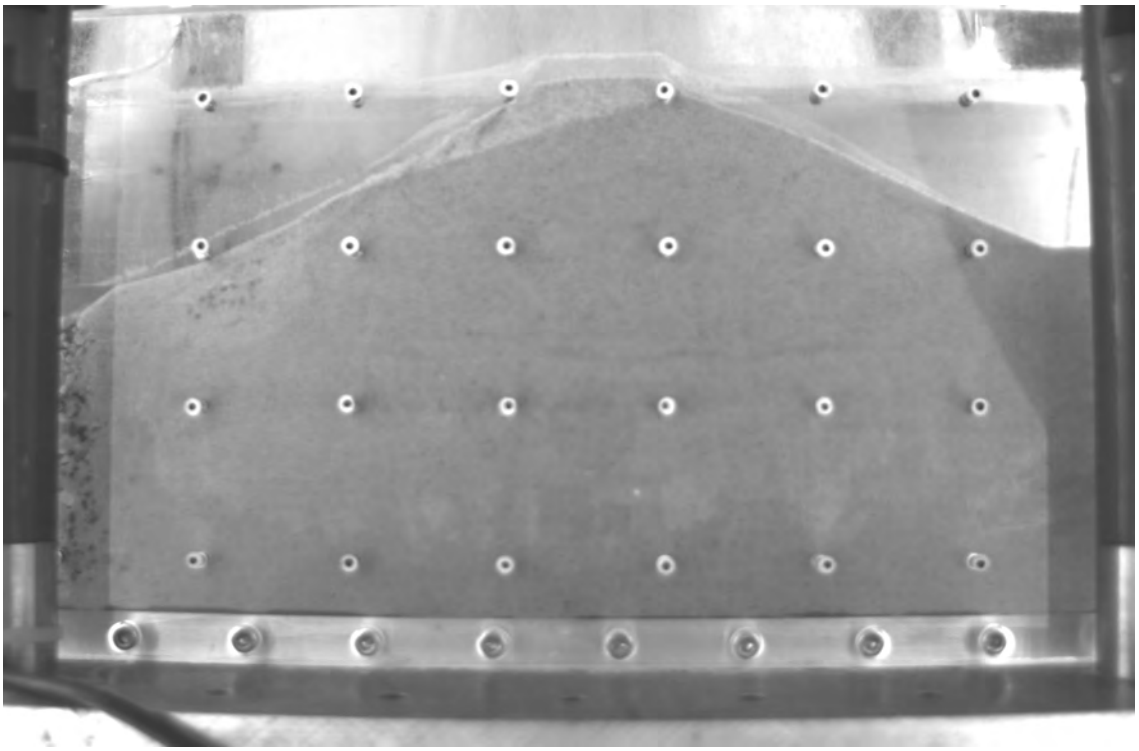

Figure G.39: Photo taken 7.6 seconds after start of rapid drawdown

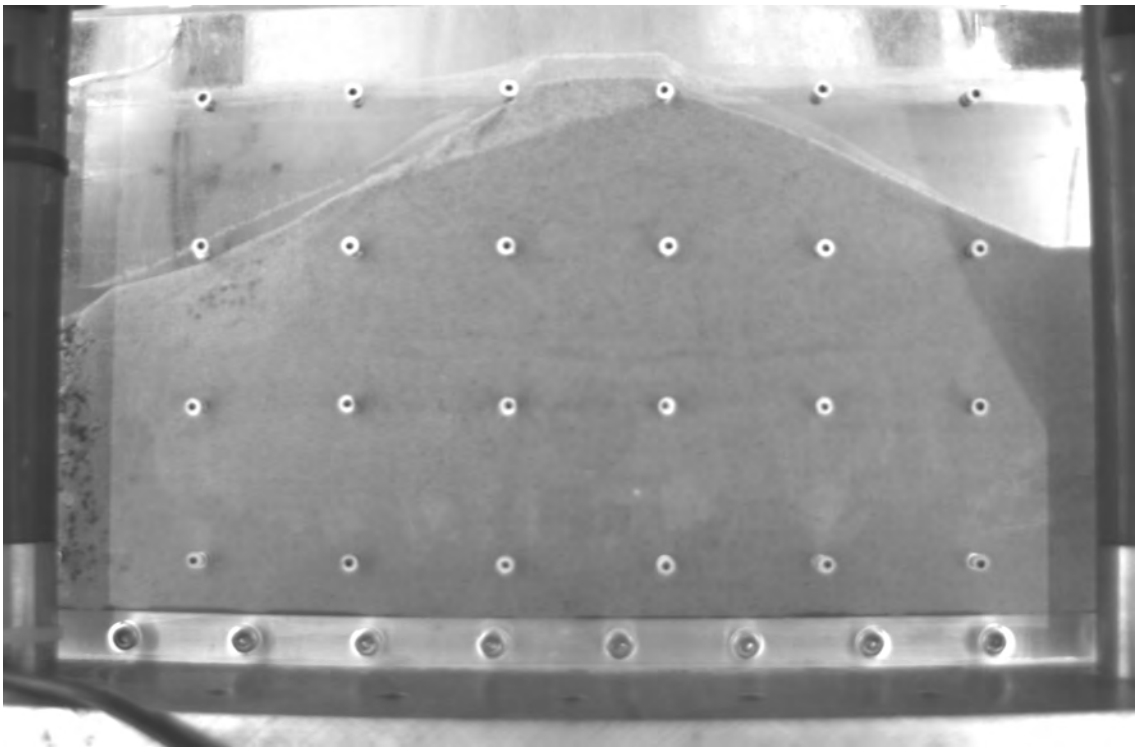

Figure G.40: Photo taken 7.8 seconds after start of rapid drawdown

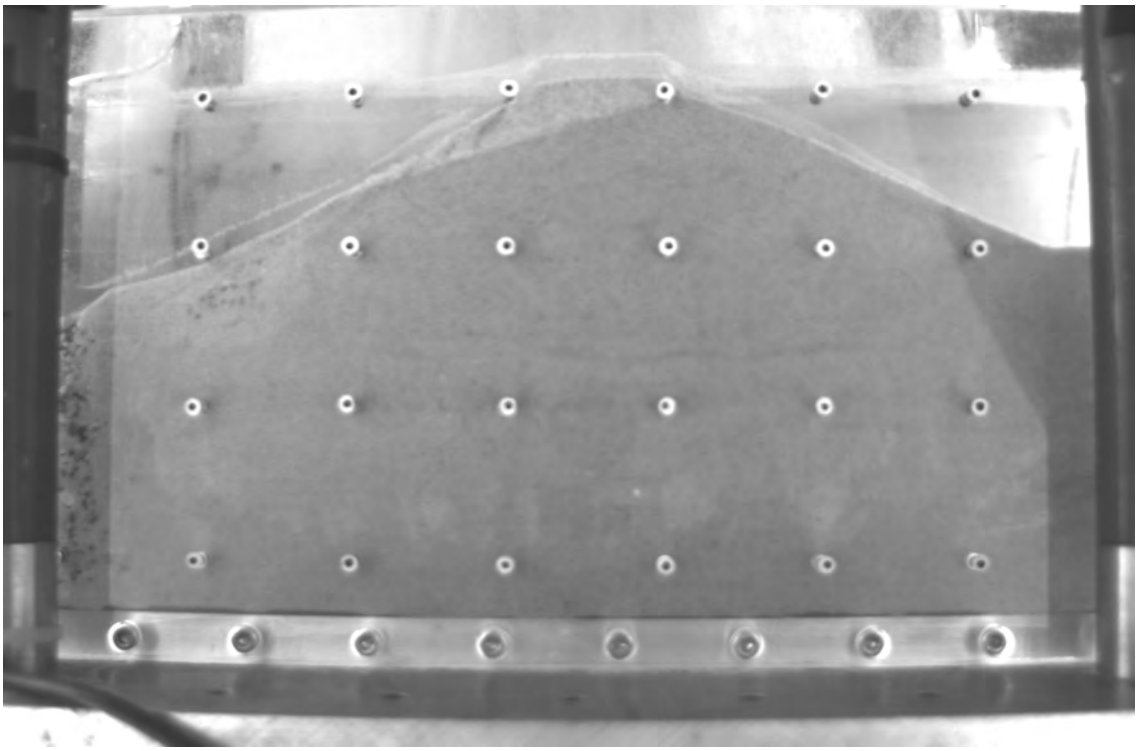

Figure G.41: Photo taken 8.0 seconds after start of rapid drawdown

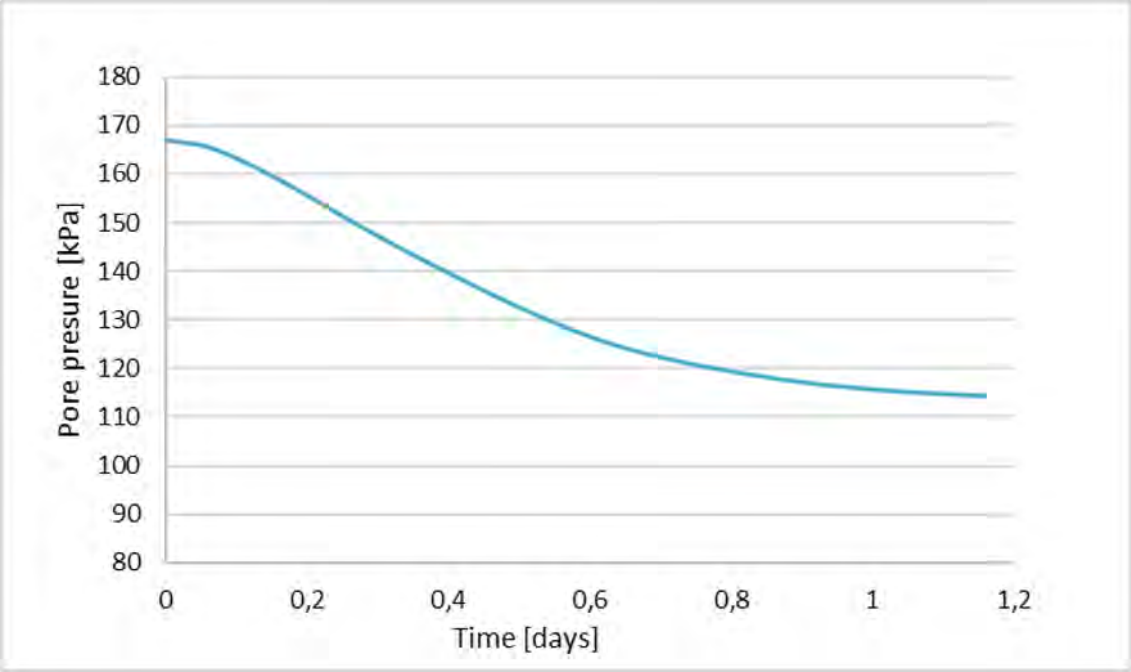

Figure G.42: water level used as input for PLAXIS model

H

Numerical model Delta21 dike

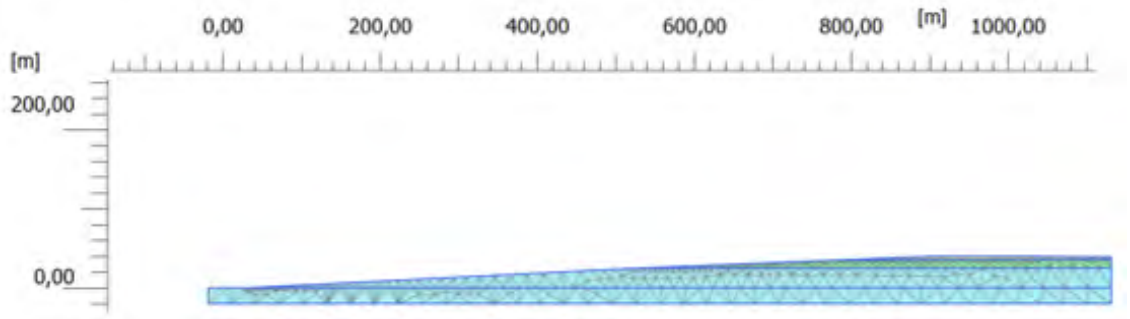

Figure H.1: Mesh of the numerical model for the Delta21 dike